

8605524

Schaffer, James Peter

**DECONVOLUTED DOPPLER BROADENED POSITRON ANNIHILATION
SPECTROSCOPY: CHARACTERIZATION OF DEFECTS IN ALUMINUM**

Duke University

Ph.D. 1985

**University
Microfilms
International** 300 N. Zeeb Road, Ann Arbor, MI 48106

Copyright 1985

by

Schaffer, James Peter

All Rights Reserved

BEST AVAILABLE COPY

THIS PAGE BLANK (USPTO)

This is an authorized facsimile, made from the microfilm master copy of the original dissertation or master thesis published by UMI.

The bibliographic information for this thesis is contained in UMI's Dissertation Abstracts database, the only central source for accessing almost every doctoral dissertation accepted in North America since 1861.

UMI[®] Dissertation
Services

From: ProQuest
COMPANY

300 North Zeeb Road
P.O. Box 1346
Ann Arbor, Michigan 48106-1346 USA

800.521.0600 734.761.4700
web www.il.proquest.com

Printed in 2005 by digital xerographic process
on acid-free paper

THIS PAGE BLANK (USPTO)

**DECONVOLUTED DOPPLER BROADENED POSITRON ANNIHILATION
SPECTROSCOPY: CHARACTERIZATION OF
DEFECTS IN ALUMINUM**

Figure 14.	A Comparison of the Peak Region of the Raw Data and the Deconvoluted Data for a Quenched Aluminum Sample.	70
Figure 15.	A Plot of the Error Parameter vs. Quench Temperature.	72
Figure 16.	A Plot of R_1 Values for the Raw Data vs. Quench Temperature.	80
Figure 17.	A Plot of R_1 Values as Calculated from Average Lineshape Parameter Values for the Raw Data vs. Quench Temperature.	82
Figure 18.	A Plot of R_1 Values for the Deconvoluted Data, Using All Retained Coefficients, vs. Quench Temperature.	83
Figure 19.	A Comparison of the Raw Data for an Aluminum Sample Quenched from 600°C and the Same Sample after a High Temperature Anneal.	84
Figure 20.	A Comparison of the Tail Region of the Raw Data for an Aluminum Sample Quenched from 600°C and the Same Sample after a High Temperature Anneal.	85
Figure 21.	A Comparison of the Deconvoluted Data for an Aluminum Sample Quenched from 600°C and the Same Sample After a High Temperature Anneal.	87
Figure 22.	A Comparison of the Tail Region of the Deconvoluted Data for an Aluminum Sample Quenched From 600°C and the Same Sample After a High Temperature Anneal.	88
Figure 23.	A Comparison of the Tail Region of the Same Samples as in Figure 22, but this time Both Data Sets were Deconvoluted Using the Same Number of Coefficients.	92
Figure 24.	A Plot of R_1 Values for the Deconvoluted Data Using a Constant Number of Reconstruction Coefficients.	93

LIST OF FIGURES

	Page
Figure 1. A Schematic Diagram Showing the Effects of the Electron-Positron Pair Momentum on the Energy and Direction of the Two Resulting Annihilation γ -Rays in the Laboratory Reference Frame.	9
Figure 2. A Typical Instrument Resolution Function for the Doppler PAS System Used in this Work.	21
Figure 3. A Schematic Diagram of the Quenching Apparatus.	27
Figure 4. A Schematic Diagram Showing the Relationship Between $r(x)$, $f(x)$, and $h(x)$.	30
Figure 5. A Plot Comparing the Power Spectrum of the Annihilation Energy Distribution Before and After Deconvolution.	46
Figure 6. A Semi-Log Plot of the Number of Reconstruction Coefficients Retained by the FFT/PS Algorithm as a Function of the Number of Counts in the Peak.	47
Figure 7. A Comparison of the Raw Data and the Deconvoluted Data for an Irradiated Sapphire Sample.	49
Figure 8. A Comparison of the Raw Data, $h(x)$, with the Function Obtained by the Convolution of $f(x)$ with $r(x)$.	50
Figure 9. A Comparison of the Resolution Function Before Deconvolution, After Deconvolution Using 70 Coefficients, and After Deconvolution Using 243 Coefficients.	54
Figure 10. A Plot of the Deconvoluted Lineshape Parameter $x(1)$ as a Function of Quench Temperature.	58
Figure 11. A Plot of the Raw Data Lineshape Parameter $x(1)$ as a Function of Quench Temperature.	62
Figure 12. A Comparison of the Shape of Resolution Functions Collected at Different Times During a Series of Experiments.	64
Figure 13. A Graphical Interpretation of the Sensitivity and Error Lineshape Parameters.	67

F. A LISTING OF THE FORTRAN FFT/PS DECONVOLUTION PROGRAM	117
G. RELATIONSHIP BETWEEN C_v AND C_d	141
H. THE UTILITY OF "R" PARAMETER ANALYSIS	143
REFERENCES	145

TABLE OF CONTENTS

ABSTRACT	(iii)
ACKNOWLEDGEMENTS	(iv)
LIST OF FIGURES	(vii)
CHAPTERS	
I. INTRODUCTION	2
II. EXPERIMENTAL PROCEDURES	17
The Doppler PAS System, 17	
Specimen Preparation, 23	
III. DECONVOLUTION OF DOPPLER PAS MEASUREMENTS	28
The Mathematics of Deconvolution, 29	
Previous Deconvolution Techniques, 33	
The FFT/Power Spectrum Deconvolution Method, 39	
Test of the Method, 44	
IV. RESULTS AND DISCUSSION	52
The Utility of the FFT/PS Deconvolution Algorithm, 52	
The Separation of Multiple Defect Types, 74	
V. CONCLUSIONS AND FUTURE WORK	96
APPENDICES	
A. POSITRON THERMALIZATION TIMES	104
B. THE EQUIVALENCE OF DOPPLER AND ANGULAR CORRELATION MEASUREMENTS	107
C. CHEMICAL ANALYSIS OF THE ALUMINUM	111
D. THE UTILITY OF FOURIER ANALYSIS IN DECONVOLUTION	112
E. THE MATHEMATICAL DIFFICULTIES ASSOCIATED WITH THE INCORRECTLY POSED INTEGRAL EQUATION	114

ABSTRACT

Positron Annihilation Spectroscopy (PAS) has become a useful tool for the nondestructive investigation of the defect structure of materials. Of the existing PAS measurement techniques Doppler broadening appears to offer several practical advantages. These advantages include low radioactive source strength requirements, comparatively short experimental times, and minimal geometrical restrictions. Unfortunately, the technique suffers from some inherent disadvantages. These include comparatively poor instrumental energy resolution and a limited ability to distinguish between multiple defect types.

In an attempt to overcome the difficulties associated with the use of Doppler broadened PAS the Fast Fourier Transform/Power Spectrum (FFT/PS) deconvolution algorithm has been developed in this work. This algorithm is computationally efficient, noniterative, and requires minimal a priori information. The utility of the FFT/PS deconvolution algorithm is demonstrated for high purity aluminum samples containing known concentrations of vacancies or prismatic dislocation loops. It is shown that the FFT/PS procedure is capable of automatically correcting for accidental and/or intentional changes in the instrument resolution function. In addition, based on the limited data analyzed in this work, it appears that both the sensitivity and the accuracy of the energy distribution lineshape parameters are improved by deconvolution. Finally, it is demonstrated that if the filtering error introduced by the FFT/PS procedure is controlled, then it is possible to distinguish between samples containing predominately vacancy type defects and those with prismatic dislocation loops as the dominant defect type.

DECONVOLUTED DOPPLER BROADENED POSITRON ANNIHILATION

SPECTROSCOPY: CHARACTERIZATION OF

DEFECTS IN ALUMINUM

by

James Peter Schaffer

Department of Mechanical Engineering and
Materials Science

Duke University

Date:

June 21, 1985

Approved:

Phillip L. Jones
Phillip L. Jones, Supervisor

Marion L. Shepard

E. J. Haughey

George W. Reasall

Howard B. Clark

Dissertation submitted in partial fulfillment of
the requirements for the degree of Doctor of
Philosophy in the Department of Mechanical
Engineering and Materials Science
in the Graduate School of
Duke University

1985

Copyright by
James Peter Schaffer
1985

CHAPTER I

INTRODUCTION

Over 50 years ago, Dirac postulated the existence of an atomic particle with a mass equal to that of an electron, but which is positively charged. In 1932 these positively charged electrons, referred to as positrons, were first observed by C. D. Anderson as a by-product of cosmic ray showers. Since that time positron research has been pursued in such varied disciplines as high energy nuclear physics, astrophysics, and materials science. It is within the broad context of materials science, and more specifically in the area of non-destructive testing (NDT) of aluminum, that the interaction of positrons with matter will be examined in this work. Before going on to describe the use of positrons as an NDT tool in the investigation of the defect structure of metals, a brief review of positron physics will be presented. A comprehensive treatment of this subject has been written by West (1974).

As postulated by Dirac in 1935, positrons and electrons are complementary states of matter such that when the two particles encounter one another they will annihilate each other. Their kinetic and rest mass energies will be dissipated as the energy of one, two, or three gamma rays in such a way as to conserve momentum. It can be shown that the ratio of the two-photon to three-photon annihilation event is 372:1 (Stevens 1980), while the ratio of the two-photon to one-photon events is $\sim 2.6 \times 10^6:1$, (West 1974). With these ratios as justification the remainder of this work will consider only the annihilation event yielding two photons. If both the electron and positron were at rest, a

positrons in vacancy type lattice defects. This effect was first observed by MacKenzie et al. and Dekhtyar et al. in 1964. Schultz et al. (1981) describe the changes in the annihilation characteristics due to the localization of a positron in a monovacancy type defect as follows: 1) Because the localized positron has a smaller overlap of its wave function with that of the high energy core electrons than it does when diffusing through the nearly perfect lattice, the annihilation rate with high energy core electrons decreases. 2) The density of conduction electrons in the vacancy is also decreased resulting in a decreased annihilation rate with conduction electrons. However, the percentage reduction is less than in the case of core electrons so that the net result is an increase in the fraction of annihilation events involving low energy conduction electrons, thus resulting in a decrease in the width of the Doppler broadened annihilation radiation distribution. 3) The potential for electrons in the vacancy is higher than normal resulting in the conduction electrons traveling more slowly. This in turn also decreases the observed Doppler broadening. 4) A second order effect is that the overlap of the positron wave function with weakly bound outer-core electrons is reduced less than is the overlap with inner-core electrons. This too leads to less broadening of the observed 511 KeV line. 5) The uncertainty principle requires that localization of the positron be accompanied by an increased spread in its momentum distribution (and a corresponding decrease in its de Broglie wavelength). As a result, the contribution of the positron to the center-of-mass velocity increases corresponding to a broadening of the annihilation energy spectrum (Schultz et al. 1981). The first four effects lead to a narrowing of the annihilation energy spectrum while the fifth effect tends to broaden the spectrum. The combination of these effects results in more sharply peaked (narrower) Doppler spectra for metals containing defects which are capable of trapping positrons (Siegel 1980).

As discussed by Siegel (1980) it is important to note that the positron is not equally sensitive to all lattice defects. It is sensitive to defect regions which can be characterized as having a lower-than-average electron density, for example, vacancies, small vacancy clusters, voids, and dislocation lines or jogs. On the other hand, positrons are relatively insensitive to defect regions with a higher-than-average electron density such as interstitials. Indeed this defect specificity is one of the advantages PAS measurements offer as compared with other NDT techniques such as residual electron resistivity (Siegel 1980).

In addition, positrons are capable of probing the entire depth of the valence band (MacKenzie et al. 1964) which is in contrast with techniques such as electrical and thermal conductivity, thermoelectric power, Hall coefficient, magnetic susceptibility, and Knight shift, all of which yield information restricted to the electrons near the Fermi surface.

PAS measurements are an attractive NDT tool since the positron causes negligible perturbation of the electronic structure as it passes through a crystal (Johnson et al. 1978) and the positron-electron interaction does not appreciably alter the momentum distribution of the electrons (Szotek and Chmielewski 1981). A further advantage of the technique is that it yields information regarding both the electron momentum distribution as well as the electron density within the sample (Siegel 1980).

The three most common PAS techniques are lifetime measurements, angular correlation, and Doppler broadening. The effective electron density in the region from which the positron annihilates can most easily be determined using lifetime measurement techniques. These measurements usually use ^{22}Na as a source material since it simultaneously (< 10 psec) emits a γ -ray along with the positron. This 1.28 MeV γ -ray acts to start the timing apparatus

which is stopped by the arrival of the ~ 511 KeV γ -ray signifying the occurrence of the annihilation event. The positron lifetime depends on the concentration and distribution of the electrons in the region of the material through which the thermalized positron drifts before its annihilation. This "mean" lifetime will of course be affected by any process, such as the trapping of positrons at defects, which alters the local concentration of electrons seen by the positron (Coleman 1977). These mean lifetimes, which are on the order of hundreds of picoseconds, can be measured to an accuracy of a few picoseconds with modern equipment.

As mentioned previously, when the annihilation event does occur the electron-positron pair will usually have a small net momentum in the laboratory frame. This net momentum affects both the energy of the resulting γ -ray as well as its direction of emission as shown in Figure 1. The relationships between the momentum of the annihilating γ -ray, the measured Doppler shift in energy, and the measured angle $\delta\phi$ are described in Appendix B.

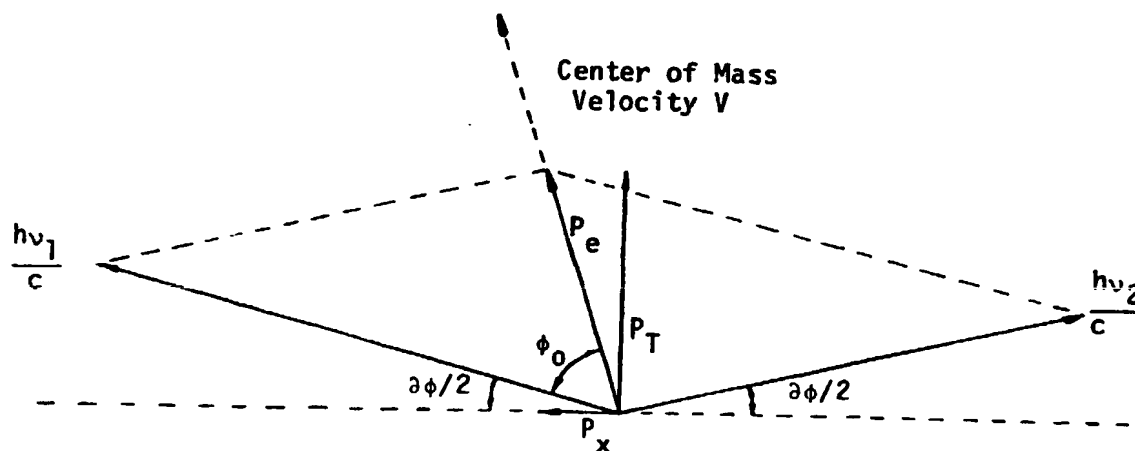


Figure 1. A Schematic Diagram Showing the Effects of the Electron-Positron Pair Momentum on the Energy and Direction of the Two Resulting Annihilation γ -Rays in the Laboratory Reference Frame.

Angular correlation measurements, which measure the deviation from colinearity of the two photons emitted from the annihilation process, were first reported by DeBenedetti and his coworkers in 1950. The so called long-slit geometry (DeBenedetti 1950) is commonly chosen since it provides both good angular resolution and adequate counting rates. However, other geometries can be employed for specific applications. The angular distribution of a sample is determined by measuring the coincidence counting rate as a function of angular deviation from colinearity. In well annealed metals this data generally takes the form of a central inverted parabola with Gaussian wings. The instrument resolution is good, typically ~ 0.5 mrad, but the counting rate is comparatively slow and the required source strengths are relatively high.

Alternatively, Doppler broadening measurements could be used to determine the net momentum distribution of the annihilating electron-positron pairs by measuring the energies of the resulting γ -rays. The center of mass momentum of the annihilating pair along the line of emission of the γ -ray gives rise to Doppler shifts of the γ -ray energies. The distribution of these momentum components then results in a Doppler broadening to give the 511 KeV line a width of approximately $511 (V_F/2c)$ KeV where $V_F (\sim 10^8 \text{ cm/s})$ is the Fermi velocity of the conduction electrons and c is the speed of light (Hughes 1982). Details of the experimental procedure for collecting Doppler-broadened spectra are given in Chapter II.

Although lifetime measurements, angular correlation, and Doppler-broadening measurements are by far the most common PAS techniques there are two others which should be mentioned. One of the drawbacks of using conventional sources such as ^{22}Na or ^{68}Ge is that only certain depths of the material under investigation are sampled extensively by these positrons. Hughes et al. (1982) give the equation:

$$\delta E = \pm \frac{1}{2} M_0 C^2 (\delta \theta) = \pm 255.5 (\delta \theta) \text{ eV} \quad (1.2)$$

where δE is the Doppler Energy Resolution in eV
and $\delta \theta$ is the Angular Correlation Resolution in mrad.

The best Doppler systems have a resolution of about 1.2 KeV which corresponds to an angular correlation resolution of 5 mrad. Typical angular correlation systems have a resolution approximately an order of magnitude better than this. For Doppler broadening techniques to effectively compete with angular correlation techniques in high precision applications it is necessary to improve the effective resolution of Doppler PAS. Schultz et al. (1981) point out that theoretically a 10-fold increase in effective resolving power of Doppler measurements can be achieved by deconvolution.

Deconvolution is the mathematical technique used to separate the instrumental broadening effects from the true Doppler broadened positron annihilation γ -ray spectrum. Instrumental broadening is a complicated problem caused by many different factors. For example, physical properties of the detector crystal such as frontal dead layers, geometry of the active region, and regions of poor charge collection, can all lead to line broadening. The primary contribution to instrumental broadening in a solid state semiconductor detector is due to statistical fluctuations in the division of absorbed energy between ionization and heating of the crystal lattice, i.e. the Fanno effect, (McNelles and Campbell 1975).

The shape of the instrument resolution function, as well as the magnitude of the line broadening, is most often determined from the 514 KeV γ -ray emitted from the isotope ^{85}Sr . The difficulty lies in the fact that the Doppler-broadening of the 511 KeV γ -ray line in the absence of defects in a metallic crystal is of the same order (\sim KeV) as the detector resolution, and

changes induced by defects are significantly smaller. Fortunately, the defect induced changes in the deconvoluted γ -ray energy distribution are much more dramatic than in the instrumentally smeared raw data (McNelles and Campbell 1975). In addition, removing instrumental effects offers another advantage. Such a procedure allows direct comparison of experimental results obtained in different laboratories. If results are reported without deconvolution they must be nondimensionalized in some way or else the instrument resolution function must also be reported. In either case the interpretation of results is complicated in the absence of a deconvolution procedure.

In light of the above discussion it was decided that the results presented in this work would be for deconvoluted Doppler spectra. Unfortunately, the mathematics involved are somewhat complicated. Because of this, most of the existing deconvolution schemes are iterative in nature and hence computationally inefficient. One of the major goals of this work was to develop a deconvolution scheme for Doppler broadened positron annihilation measurements which is model independent, does not require iteration, and which yields reproducible results.

In addition to the need for deconvolution, DBPAS also currently suffers from an inability to distinguish various defect types. For example, vacancies and dislocations tend to alter the annihilation lineshape in qualitatively the same manner. That is, in both cases the spectrum becomes more narrow as the defect concentration increases. Most of the lineshape parameters currently used to characterize Doppler broadened spectra are unable to distinguish the effects of different defect types because they describe only gross changes in lineshape. For example, MacKenzie's S-parameter, which is the most commonly used lineshape parameter, essentially measures the width of the distribution (MacKenzie et al. 1970). Hence, for any given spectrum such

an analysis yields a single value. This is useful if there is only one degree of freedom in the series of experiments. If two variables are allowed to change, however, it is impossible to separate their effects. Clearly, additional parameters are required. The other parameters selected must be uncorrelated with the S-parameter. That is, if the second parameter chosen is a function of the first parameter only, then no new information is gained. Campbell (1977) and Schultz et al. (1981) have discussed the use of other possible parameters to describe lineshapes. Although these parameters may be more sensitive to variations in specific defect concentrations they are correlated with S, and therefore of little help in differentiating defect types.

In light of the above discussion it can be seen that it would be desirable to find a family of lineshape parameters which is capable of distinguishing various types of metallurgical defects. For example, one of the groups of parameters to be examined in this work is the central moments of the γ -ray energy distribution. It is well known that the values of these moments give information regarding the shape of the distribution. In fact, it can be shown that if all of the moments are known one can construct the distribution. The even moments give information about the width of the distribution while the odd moments vanish for symmetrical distributions such as the ones to be examined in this work (the symmetry question is addressed in Chapter III). The second central moment is called the variance and its square root is the familiar standard deviation. The fourth central moment is called the Kurtosis or flatness. The advantage of moment analysis is that the information obtained is not redundant. For example, it is very possible to have two distributions with equal standard deviations (second moments) and yet widely different fourth moments. Such a family of lineshape parameters suggests the

possibility of separating the effects of multiple metallurgical defect types using DBPAS.

The above brief review of positron annihilation spectroscopy as an NDT tool for the study of metallurgical defects indicates that the technique with the greatest potential for practical use outside the laboratory is Doppler-broadening. This technique offers the advantages of low source strength requirements, the ability to use ^{68}Ge as a source material in order to reduce surface effects, and few geometrical experimental constraints. Doppler broadening currently suffers from relatively poor energy resolution and an inability to distinguish different metallurgical defect types. Based on these observations, the purpose of this work is twofold: 1) to develop an efficient, model independent, noniterative deconvolution method, and 2) to develop a family of lineshape parameters capable of distinguishing various defect types.

CHAPTER II

EXPERIMENTAL PROCEDURES

This chapter is divided into two sections. The first section describes the Doppler broadened PAS instrumentation and the methodology employed to collect Doppler spectra. The second section outlines the thermomechanical treatments used to create the desired defect concentrations in the metallic samples which were studied in this work.

The Doppler PAS System

The heart of the Doppler broadened PAS instrumentation system is the single crystal high purity Germanium (HPGe) detector. This detector is mounted at the end of a cold finger in a cryostat and, to reduce thermal noise, is operated at liquid nitrogen temperatures. The cylindrical detector crystal used in this work is 46.7 mm in diameter and 46.2 mm in length. When the annihilation γ -rays impinge upon the crystal their energy is absorbed by two mechanisms. The first is the creation of electron-hole pairs within the crystal. These electron-hole pairs are subsequently swept apart by the applied detector bias (4000 V) and flow through an external circuit creating a current pulse whose integral with respect to time has an amplitude proportional to the incident γ -ray energy. The second absorption mechanism is heating of the crystal. The ratio of these two absorption mechanisms is known as

the Fanno factor and the statistical fluctuations in the division of absorbed energy between ionization and heating is the primary contribution to instrumental line broadening in solid state semiconductor detectors. For further details of the absorption process see Moore (1983).

The resulting current pulse from the detector is rather weak and unsuitable for cable transmission. Because of this a preamplifier (Ortec Model 120-5) is mounted directly adjacent to the detector output. The detector and preamp are D.C. coupled, as is the entire system, and powered from the same A.C. source to prevent ground loops. The preamp is a charge sensitive device capable of accepting signals corresponding to the γ -ray energy range of 0-10 MeV. Its output is a voltage pulse with an amplitude proportional to the integrated charge supplied by the detector and hence proportional to the incident γ -ray energy. The magnitude of the voltage pulse amplitude is related to the incident γ -ray energy by the approximate conversion factor of 280 mV per MeV. Therefore for a typical 511 KeV γ -ray the output of the preamp would be approximately 143 mV. In addition to converting the detector charge pulse to a voltage pulse with an intensity suitable for cable transmission the preamp also shapes the resulting voltage pulse so that it is acceptable to the linear amplifier.

The linear amplifier used in this work is an Ortec Model 571. It accepts the shaped pulses from the preamp and amplifies them to suitable voltages for transmission to the multichannel analyzer. The output pulses are active filter shaped (skewed Gaussian approximations) and have amplitudes in the 0-10 V range. Unipolar outputs are used to optimize the signal-to-noise ratio (resolution). Since the main amplifier is operated within its linear range the amplitude of the output voltage pulse is proportional to the incident γ -ray energy as measured by the HPGe detector.

The output from the linear amplifier is routed to an Ortec Model 408A biased amplifier. This device accepts the output pulses from the main amplifier and allows one to selectively view any region of the initial 0-10 MeV energy range. In this work the biased amplifier was used to select the energy window of 483 to 548 KeV. The output pulses from the biased amplifier serve as the input to the analog-to-digital (ADC) converter located within the Norland IT-5300 multi-channel analyzer (MCA). In this device the amplitude of the voltage pulse is converted to a digital representation of the energy of the detected γ -ray and subsequently dynamically displayed on the MCA's CRT in the form of a histogram of energy versus count intensity. The MCA can be programmed to accept input signals until a predetermined number of counts in the peak channel is reached. At this time the experiment is terminated and a complete Doppler broadened spectrum is displayed on the CRT. The energy distribution is then ready for transmission to the computer for subsequent data manipulation.

The two most important parameters which characterize the quality of a Doppler PAS system are the width, in units of energy, of the instrument resolution function and the energy resolution, in units of eV per channel, of the MCA. The width of the instrument resolution function (IRF) is, in essence, a measure of the quality of the detector crystal, although it is also affected by the associated amplification electronics as well as the ADC. The IRF is most often determined by examining the response of the system to the monoenergetic ($E = 514$ KeV) photons emitted from the isotope ^{85}Sr . If the instrumentation was perfect the energy distribution, as recorded by the MCA, would consist of a single bar in the histogram in the channel corresponding to 514 KeV. However, in any real instrumentation this line will be broadened for reasons previously discussed. The amount of instrumental broadening is most often re-

ported in terms of the energy width of the ^{85}Sr line as measured across the two channels which contain half the number of counts in the peak channel. This energy measure is commonly named the full width half maximum (FWHM). Figure 2 shows typical IRF for the Doppler PAS system used in this work. As can be seen in this figure the FWHM of the IRF is about 1.28 KeV.

The second parameter which describes the quality of the Doppler PAS instrumentation is the energy resolution of the MCA which is determined by the following procedure. First, a Doppler broadened spectrum is collected and the channel corresponding to its centroid is determined. The centroid channel is assigned the energy value 511 KeV. Next, an energy spectrum is obtained for the isotope ^{85}Sr . The channel corresponding to the centroid of this distribution is calculated and assigned the energy value 514 KeV. The MCA energy resolution is then easily calculated by dividing the energy difference (3 KeV) by the number of channels between the centroids. In this work the 511 KeV channel was number 439 while channel number 486 corresponded to 514 KeV. Hence, the MCA energy resolution is $3000 \text{ eV}/(486 - 439)$ or $\sim 64 \text{ eV per channel}$. Clearly this value can be adjusted using the biased amplifier. The reason for selecting the 64 eV/channel is to obtain the best possible resolution while maintaining the ability to display the entire region of interest (483 to 548 KeV) on the 1024 channel MCA. The reasons for requiring the above energy window will be discussed in Chapter III.

While the MCA energy resolution is a parameter which, to a certain extent, can be varied, the IRF is essentially predetermined by the instrumentation. The one factor contributing to the width of the IRF which can be controlled is the data acquisition, or count rate. It is well known that increasing the count rate decreases the instrument resolution. Therefore, one must select a count rate which results in an acceptable line broadening while

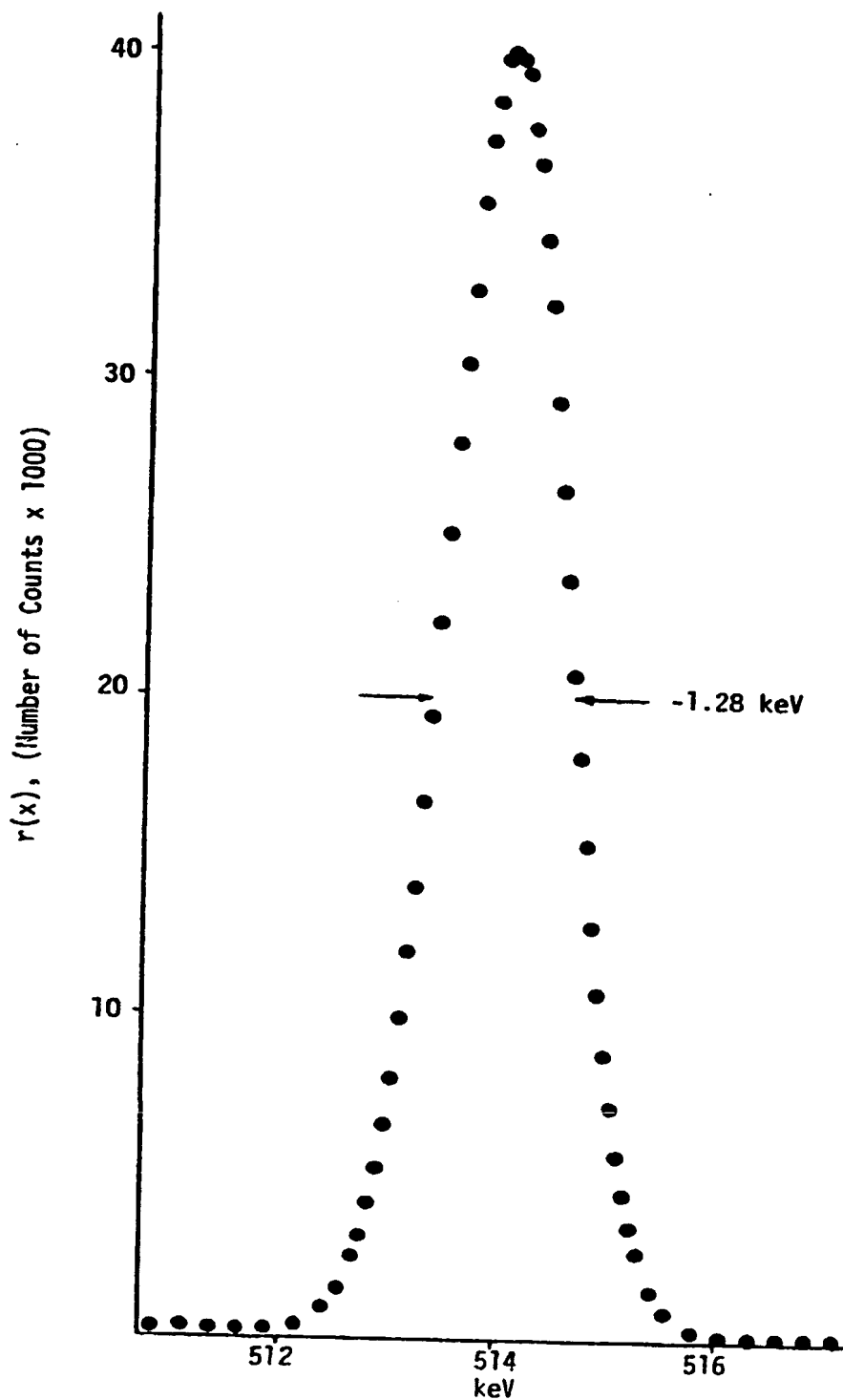


Figure 2. A Typical Instrument Resolution Function for the Doppler Pas System used in this Work. Note that the Full Width Half Maximum is about 1.28 keV.

keeping the time required to collect a spectrum reasonably short. Moore (1983) demonstrated that with the Doppler instrumentation used in this work very reproducible results can be obtained with count rates of ≤ 2 kHz. The count rate is easily adjusted by changing the sample to detector distance. All of the results reported in this work were obtained using count rates of ≤ 2 kHz with an associated experiment time of ~ 30 minutes resulting in a peak height of 40K counts and $\sim 3 \times 10^6$ total integrated counts.

The positron source isotope in all experiments was ^{68}Ge which was chosen to avoid surface effects. The mean depth of penetration in aluminum for such positrons is ~ 0.50 mm. The activity of the source was initially 50 μC . The half-life of ^{68}Ge is ~ 275 days and hence the activity of the source did not change significantly for any single set of experiments since a typical set of measurements requires less than a week to accumulate. It should be pointed out that the activity of the source does not measurably affect the observed annihilation spectra, provided the count rate remains constant.

Although the count rate can be easily adjusted by changing the source to sample distance such a change introduces an additional error source. This error source is related to the source/sample geometry. It has been demonstrated that the observed spectra may depend on the angle with which the gamma rays impinge upon the detector crystal (Smedskjaer 1983). It has also been shown that in high precision experiments among samples of the same material, one should use samples of nearly identical thickness to reduce the error associated with small angle scattering (Smedskjaer 1983).

The ^{68}Ge source was deposited on a thin (~ 0.05 mm) nickel foil for handling convenience. This results in what is known as a source contribution to the annihilation lineshape. That is, in each experiment some of the positrons will annihilate in the nickel foil and the γ -rays produced by these

events will contribute to the overall annihilation spectrum. However, the ratio of source annihilation events to sample annihilation events is small ($< 1\%$), and the source contribution is neglected in the remainder of this work.

In all measurements the source and sample were arranged in what is commonly called the sandwich configuration. In this configuration the positron source is placed between two identically treated metallic samples. The samples are thick enough, typically a few millimeters, to guarantee that virtually all of the positrons annihilate within the material being examined.

Specimen Preparation

The material examined in this work is high purity, large grain size aluminum purchased from the Materials Research Corporation. The aluminum was zone refined to a nominal purity of 99.9995% before being vacuum melted and cold fabricated to size. The chemical analysis, in PPM of metallic interstitials, is listed in Appendix C. The aluminum was supplied as a 13 mm diameter rod from which ~ 1.5 mm thick disks were machined. Each of these disks had an ~ 1.5 mm hole drilled through it near its edge. The purpose of this hole was to allow the disks to be suspended from a titanium wire while within the vertical tube furnace. After the disks were machined to size, they were given a full anneal heat treatment consisting of 2 hours at 400°C followed by furnace cooling overnight. The as annealed aluminum disks were the starting material for all subsequent thermal treatments.

The thermal treatments used in this work are very similar to those outlined by Cotterill et al. (1972). In this work the authors describe a two step time/temperature cycle which allows one to produce, in a controlled fashion, first samples with vacancies as the dominate defect type, and then,

samples with dislocation loops as the major defect type. The actual thermal treatment employed in this work is as follows:

- 1) Heat the samples to the desired quenching temperature and hold them at temperature for one hour to establish thermal equilibrium.
- 2) Quench the samples from the furnace into $\sim 293^{\circ}\text{K}$ water.
- 3) Dry the samples within 5 to 10 seconds.
- 4) Quench from $\sim 293^{\circ}\text{K}$ to a liquid nitrogen bath at 77°K . This procedure has been shown to produce primarily vacancies, the concentration of which is a direct function of the quenching temperature.
- 5) After DBPAS characterization, the aluminum disks are then annealed at 353°K for thirty minutes, which results in the production of prismatic dislocation loops by vacancy coalescence.
- 6) The samples are cooled to 77°K and the PAS measurements corresponding to the dislocation loops are made.
- 7) Finally the disks are annealed at 523°K for two hours to remove the dislocations and return the material to the annealed state.

Several of the steps in this procedure require further explanation. The quenching procedure is taken from Cotterill et al. (1972) and their results together with the following discussion forms the basis for the assumption used in this work that the PAS measurements made after step 4 are for a fairly uniform distribution of vacancies of concentration approximately equal to the equilibrium concentration at the quenching temperature.

Quenching experiments are usually performed on thin metallic foils so that the quench rate remains constant across the sample. However, as discussed previously, constraints imposed by the positron annihilation experiments put a lower limit on the sample thickness of ~ 1.5 mm. For a complete review of the complications which can evolve during quenching due to increased

sample thickness see, for example, Cotterill et al. (1965). The main problems to be addressed here are the formation of vacancy clusters and the loss of vacancies at the sample surfaces. The second problem was investigated in a paper by Wilkes and Harrison (1972) in which they observed the quenching of 3 mm thick disks of aluminum and reported a very low vacancy loss. Since the samples used in this work are only ~ 1.5 mm thick and since the quench procedure is similar to that employed by Wilkes and Harrison, it will be assumed that the vacancy loss during the quench can be ignored. As for the formation of vacancy clusters, the positron lifetime measurements of Cotterill et al. (1972) demonstrate that for this quenching procedure the probability of forming bivacancies, or larger clusters, is small.

It is very important to dry the samples thoroughly between the water quench and the liquid nitrogen quench. This is necessary to avoid the formation of a thin layer of ice on the specimen surface which would contribute an undesirable component to the measured PAS spectrum. As pointed out by Cotterill et al. (1972) the annealing of the vacancies during this short drying procedure may be neglected since the mean lifetime of vacancies (at room temperature) in a specimen quenched from 873°K is ~ 100 s and increases for lower quenching temperatures. It is, of course, desirable to keep the drying time as short as possible.

Step 5 of the procedure, the formation of prismatic dislocation loops from the collapse of disk shaped vacancy clusters during a low temperature anneal of aluminum, was reported by Hirsch et al. in 1958. Cotterill et al. (1972) demonstrate that the appropriate thermal treatment consisted of a 30 minute anneal at 353°K. The theoretical relationship between the vacancy concentration after the quench, C_v , and the concentration of dislocation cores, C_d (given as an atomic fraction), is presented in Appendix G.

The apparatus used to perform the thermal treatments is shown in Figure 3. A quartz tube passes through a vertical tube furnace and is attached to the room temperature water reservoir by a "quick disconnect" coupling. Just above the water level in the reservoir is the argon supply port. All thermal treatments were performed in an argon atmosphere to avoid oxidation. The other end of the tube is connected to a flow meter which is used to monitor the argon flow rate. The other side of the flow meter is vented to atmosphere. The temperature is measured by a chromel-alumel thermocouple positioned inside the tube furnace and adjacent to the aluminum disks. These disks are supported by a titanium wire, the other end of which is connected to an iron slug. The slug, and hence the specimens, are held in position in the furnace by a magnet located outside of the tube. The actual quench is performed simply by pulling the magnet away from the tube and allowing the entire specimen-wire-slug arrangement to fall by gravity into the quench bath. It is, of course, important for the system to be designed so that the specimens fall freely through the tube and quickly reach the quench bath. If the specimen-wire-slug arrangement does not fall freely the temperature of the samples when they enter the water will be significantly lower than the temperature measured by the thermocouple.

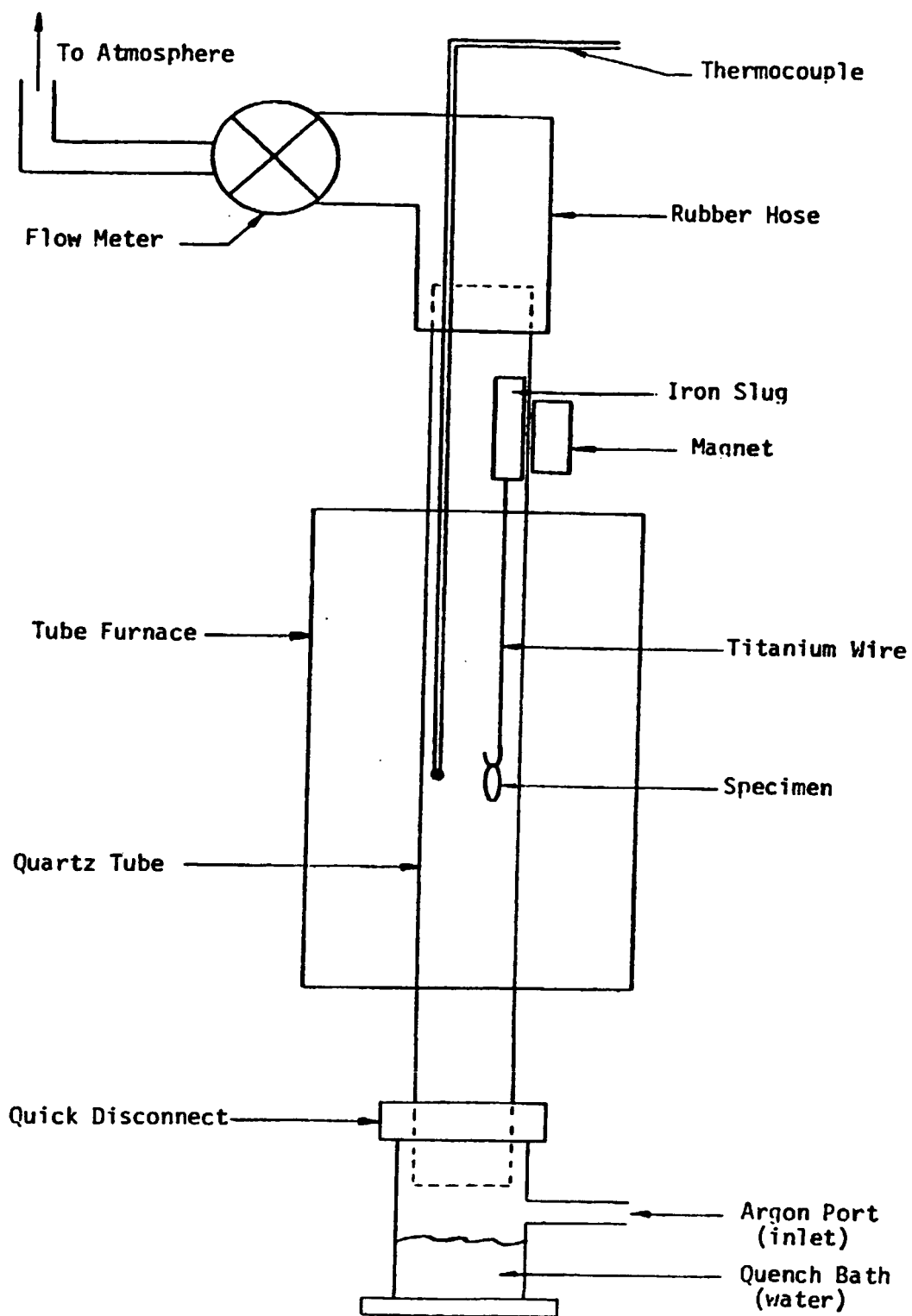


Figure 3. A Schematic Diagram of the Quenching Apparatus.

CHAPTER III

DECONVOLUTION OF DOPPLER PAS MEASUREMENTS

As discussed in the introduction, compared to angular correlation (AC) measurements, the major disadvantage of the Doppler PAS technique is its inherently poor energy resolution. In order for Doppler methods to be competitive with AC methods in high resolution applications the instrumental line broadening must be removed from the experimentally obtained Doppler spectra. Mathematically, the technique which accomplishes this separation is deconvolution. In this chapter the deconvolution of Doppler PAS measurements will be discussed.

The chapter is divided into four sections. In the first section the mathematics of deconvolution are presented. This section justifies the use of deconvolution techniques to separate instrumental effects from the desired true Doppler-broadened energy spectrum. In addition, the inherent advantages and mathematical difficulties associated with the use of Fourier analysis to solve the problem are addressed.

In the second section of this chapter the methods introduced by other investigators to solve the incorrectly posed deconvolution problem, along with their inherent advantages and disadvantages, are discussed. The third section presents the FFT/power spectrum deconvolution method (Schaffer et al. 1984); and describes its use in detail. In the final section of this chapter the FFT/power spectrum method is demonstrated using a neutron irradiated high purity single crystal sapphire sample.

The Mathematics of Deconvolution

The first objective of this section is to demonstrate the validity of using the convolution equation to describe the relationship between $h(x)$, the experimentally observed energy distribution, $f(x)$, the true Doppler broadened energy distribution, and $r(x)$, the instrument resolution function (IRF). In Figure 4(a) the instrument resolution function $r(x)$ is shown. Recall that this function represents the instrumental broadening of what should be a single energy line at the centroid of $r(x)$. The function $r(x)$ is assumed to be normalized to unit area. In order to understand the relationship between these three functions, $f(x)$ should be viewed as a histogram comprised of segments of width Δx . If it can be assumed that the instrumental response is linear (the detector and all associated electronics are operated within their linear range) then each segment of the $f(x)$ histogram will be broadened by the unit area IRF $r(x)$. Hence, the value of the observed function $h(x)$ at x' will have contributions from many of the $f(x)$ histogram segments in the neighborhood of x' . Figure 4(b) is a schematic representation of the contribution to $h(x')$ from the histogram section of $f(x)$ at a distance x_1 from the origin. This contribution $\Delta h_1(x')$ will be the product of the area $f(x_1)\Delta x$ and $r(x' - x_1)$, that is:

$$\Delta h_1(x') = f(x_1)r(x' - x_1)\Delta x \quad (3.1)$$

The total value of $h(x')$ will be the sum of the contributions from all possible histogram segments in $f(x)$. Thus,

$$h(x') = \sum_{i=-\infty}^{\infty} \Delta h_i(x') = \sum_{i=-\infty}^{\infty} f(x_i)r(x' - x_i)\Delta x \quad (3.2)$$

or as the width of the segments approaches zero the summation in Eq. 3.2 is replaced by an integral to yield,

$$h(x') = \int_{-\infty}^{\infty} f(x)r(x' - x)dx \quad (3.3)$$

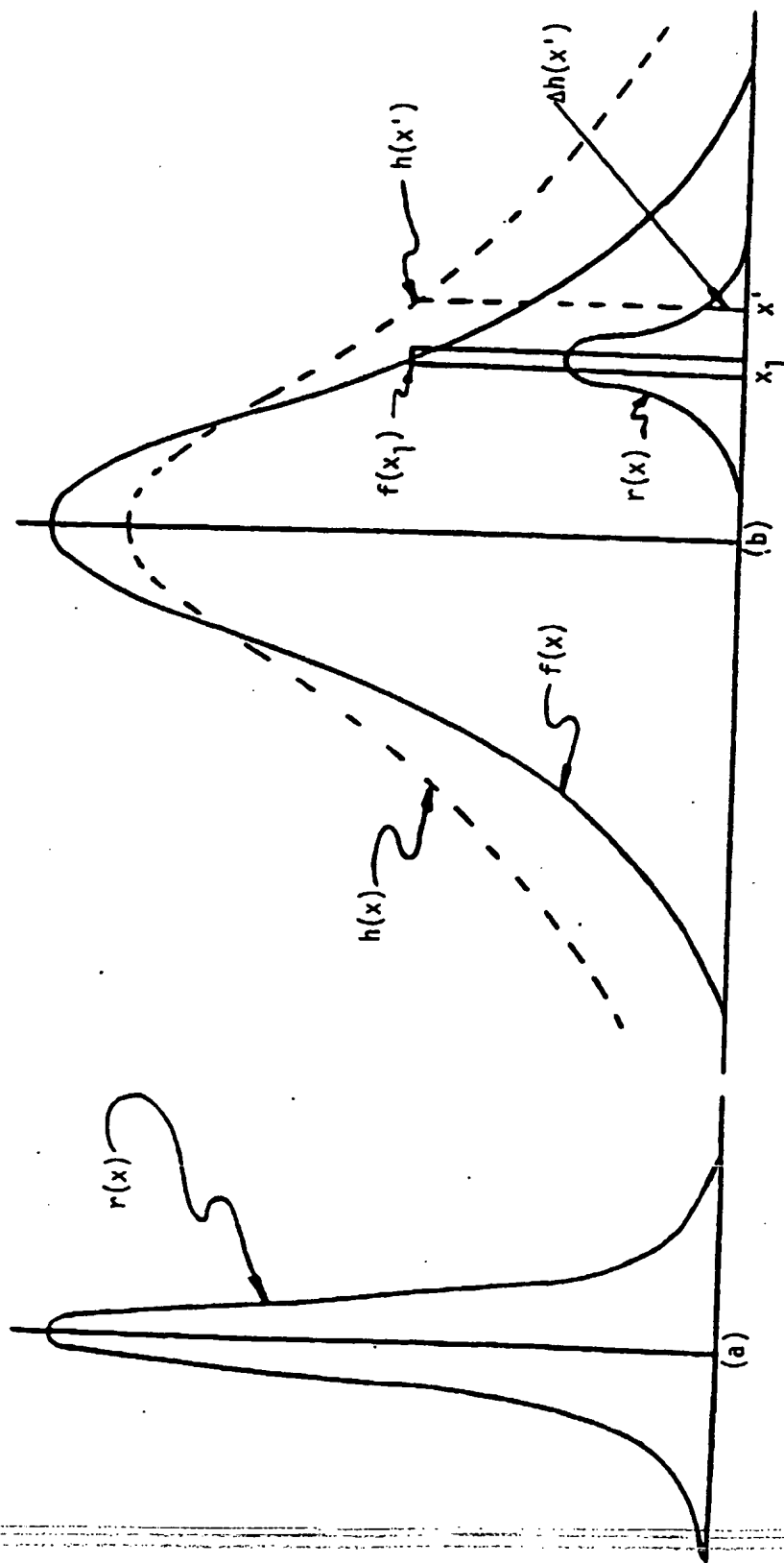


Figure 4. (a) The Instrument Resolution Function $r(x)$, (b) A Schematic Representation of the Contribution to $h(x')$ from the Histogram Section of $f(x)$ at a Distance x_1 from the Centroid.

Clearly the same procedure holds for any value of x in $h(x)$ and the final form of the relationship, with a change of variables, is:

$$h(x) = \int_{-\infty}^{\infty} f(y)r(x - y)dy \quad (3.4)$$

Eq. 3.4 is the convolution equation which serves as the starting point for the remainder of the mathematics used in this work.

The advantage of using Fourier analysis when dealing with convolution problems can be seen clearly when Eq. 3.4 is rewritten as:

$$H(w) = F(w) \cdot R(w) \quad (3.5)$$

where the functions in Eq. 3.5 are the Fourier transforms of the respective functions in Eq. 3.4 according to the general relationship:

$$G(w) = \frac{1}{\sqrt{2\pi}} \int_{-\infty}^{\infty} e^{-iwx} g(x) dx \quad (3.6)$$

Note that in Fourier space convolution is simply a complex multiplication. The equivalence of Eqs. 3.4 and 3.5 is demonstrated in Appendix D.

Rearranging Eq. 3.5 yields

$$F(w) = H(w)/R(w) \quad (3.7)$$

from which one can find $f(x)$ using the inverse Fourier transform

$$f(x) = \frac{1}{\sqrt{2\pi}} \int_{-\infty}^{\infty} e^{iwx} \frac{H(w)}{R(w)} dw \quad (3.8)$$

Eq. 3.8 is an expression for the true Doppler broadened energy spectrum in terms of the Fourier transforms of the experimentally observed function $h(x)$ and the instrument resolution function $r(x)$. However, the uniqueness of the solution given in Eq. 3.8 requires that $h(x)$ be known exactly. This condition is never satisfied in a real experiment and this fact significantly complicates the mathematics of the problem. The observed function $h^*(x)$ will be related to the "true" function $h(x)$, as defined in Eq. 3.4, for an unknown

function $f(x)$ by:

$$\max_{-\infty < y < +\infty} |h^*(x) - h(x)| < \epsilon \quad (3.9)$$

where ϵ is a measure of the noise associated with the stochastic nature of the experiment.

It can then be shown (see Appendix E) that there are two solutions $f_1(x)$ and $f_2(x) = f_1(x) + C \sin(2\pi nx/(b-a))$ with corresponding function h_1 and h_2 (as defined by Eq. 3.4) both of which satisfy the inequality (3.9). Hence, both f_1 and f_2 must be considered as solutions to Eq. 3.4 with a left hand side $h^*(x)$ taken from an experiment to within an error ϵ (Turchin et al. 1971). In fact, there is an infinite set of such solutions a subset of which contain indefinitely large rapidly oscillating components.

In order to understand the mathematical source of these difficulties Eq. 3.8 was investigated further. If in Eq. 3.8 $H(w)$ is replaced by $H^*(w)$

with

$$H^*(w) = \frac{1}{\sqrt{2\pi}} \int_{-\infty}^{\infty} e^{iwx} h^*(x) dx \quad (3.10)$$

and

$$h^*(x) = h(x) + \delta(x) \quad (3.11)$$

where δ is a stationary random process with zero mean, then it has been shown (Rautian 1958) that the dispersion of $f(x)$ is

$$D(f) = \langle f^2 \rangle - \langle f \rangle^2 = \frac{1}{\sqrt{2\pi}} \int_{-\infty}^{\infty} \frac{G(w)}{|R(w)|^2} dw \quad (3.12)$$

where $G(w)$ is the power spectrum of $\delta(x)$

and $|R(w)| \rightarrow 0$ for $|w| \rightarrow \infty$

Therefore the dispersion of the solution $f(x)$ can remain finite only if the power spectrum of the noise approaches zero rapidly as w approaches infinity. In practice this will not be the case since the noise will inevitably contain a "white noise" component such that $G(w)$ remains finite as $|w| \rightarrow \infty$ and the dis-

persion of the solution $f(x)$ therefore becomes infinite (Turchin et al. 1971).

Alternatively one can understand the source of the mathematical difficulties as follows. The observed function $h^*(x)$ contains high frequency noise components which are not physically realizable in the true function $h(x)$. In Eq. 3.8 these high frequency components are divided by small eigenvalues, $R(w)$, which results in large oscillations in the solution $f(x)$ (Turchin et al. 1971).

Recognizing these difficulties, previous investigators have proposed several deconvolution techniques which appear to successfully solve the problem. Since the accuracy of the deconvoluted spectrum can never really be determined, except in certain carefully constructed numerical experiments, the criticisms of a specific method tend to relate to the amount of computer time required, the complexity of the programming effort, the degree to which the analysis may be automated, or to the need for some a priori information concerning the function $f(x)$. As a preface to the introduction of the FFT/power spectrum deconvolution technique, the following section is a review of the prior techniques that have been developed to deconvolute Doppler PAS data.

Previous Deconvolution Techniques

One of the early Doppler PAS deconvolution schemes introduced by Hotz et al. (1968) is basically a matrix approach. The convolution in its discrete form is

$$h(x) = \sum_{y=-a}^a r(y - x)f(y)\Delta y \quad (3.13)$$

where Δy is the incremental width (resolution)

and the other functions have their usual meanings

This can be rewritten in matrix form as

$$b_i = A_{ji}c_j \quad (3.14)$$

where b is the discrete experimental vector (spectrum)

c is the unknown discrete vector before instrument broadening

and A is a rectangular matrix in which each row is the detector response function appropriate to the corresponding component of c .

In the method developed by Hotz et al. (1968) the matrix A is determined using ^{85}Sr and the vector b is the output of the Doppler system MCA for a given experiment. In this technique an initial estimate of the unknown vector c is made, say $c(1)$, and a corresponding vector $b(1)$ is calculated from Eq. 3.14. The quality of $c(1)$ is determined by finding χ^2 for the fit between b and $b(1)$ as defined by

$$\chi^2 = \sum_i (b_i(1) - b_i)^2 / b_i \quad (3.15)$$

Next $c(1)$ is modified in a manner described in the original work to create a second estimate, $c(2)$, of the desired function c . Then $b(2)$ is found from Eq. 3.14 and a new χ^2 value determined. The process is repeated until χ^2 is minimized. This process is extremely involved and inefficient. In addition the initial estimate $c(1)$ as well as the modification criteria used to generate subsequent $c(i)$ estimates can influence the final result.

In more recent years the matrix approach has been examined in greater detail (Aulick and Gallie 1981). Although this work is not related to Doppler PAS measurements, the mathematical problem is the same. It is demonstrated that 3.14 should be rewritten as:

$$\hat{b} = Ac \quad (3.16)$$

where $\hat{b} = b + \epsilon$

and ϵ is the measurement error

The least squares solution of Eq. 3.16 is then

$$A^t \hat{b} = c \quad (3.17)$$

where A^t is the pseudo-inverse (Penrose 1956) of A .

However, due to the fact that \hat{b} contains noise Eq. 3.16 is incorrectly posed and A will be ill-conditioned. Hence, the elements of A^t are large and the error in \hat{b} will be magnified, obscuring the true solution which is

$$c = A^t b \quad (3.18)$$

Aulick and Gallie (1981) point out that to avoid this problem one needs to calculate solutions to Eq. 3.16 in a way which will damp out the error in \hat{b} . One way of accomplishing this goal is to supply some additional a priori information about the shape of the desired vector c . The additional information recasts the problem as a constrained optimization problem. This technique is called regularization.

An example of the type of a priori information commonly supplied appears in the deconvolution technique used by Reddy and Carrigan (1970). In their approach the resolution function is assumed to be the sum of two Gaussians with the same centroid but differing in their amplitudes and widths. The shape of $f(x)$ (returning to the more common notation) is assumed to be a truncated parabola based on the free electron model (Reddy and Carrigan 1970).

Introducing these constraints on the shapes of $r(x)$ and $f(x)$ into the least square solution problem yields a physically plausible result. That is, the function $f(x)$ which is obtained by this method does not contain indefinitely large and rapidly oscillating components typical of the results obtained by evaluating Eq. 3.8 directly. The difficulties associated with this method are related to the validity of the a priori assumptions. For example, the resolution function $r(x)$ is constrained to be symmetric. In addition assuming the shape of the true Doppler energy distribution, $f(x)$, to be a simple truncated parabola is probably an oversimplification. Other investigators

(MacKenzie et al. 1976) suggest the modeling of $f(x)$ using the superposition of Gaussian and inverted parabolic functions as representing contributions from core and valence electrons respectively. While it is not the purpose of this work to discuss the validity of the various electron distribution models, the very fact that there exists more than one analytic prediction of the shape of $f(x)$ is strong reason to develop a deconvolution technique which places minimal constraints on the shape of $f(x)$.

One of the most widely used deconvolution techniques in Doppler PAS studies is an iteratively based method introduced by Jackman et al. (1974). In this method an initial estimate of the desired result $f(x)$, say $f_1(x)$, is selected. The estimate $f_1(x)$ is then convoluted with $r(x)$ to obtain $h_1(x)$, the first estimate of the experimentally obtained energy distribution $h(x)$. The function $h_1(x)$ is then compared point-by-point with $h(x)$ and if satisfactory agreement is obtained $f_1(x)$ is assumed to be a reasonable approximation to the true solution. If unsatisfactory agreement is obtained then $f_1(x)$ is modified to produce $f_2(x)$ and the process is repeated.

The initial estimate of $f(x)$, the modification procedure for obtaining $f_2(x)$ from $f_1(x)$, and the criteria for stopping the iteration procedure are all current topics of investigation in the literature. In the original method the experimentally obtained function $h(x)$ served as the initial estimate $f_1(x)$. The modification algorithm was

$$f_2(x_i) = f_1(x_i) \times \left(\frac{\sum_{j=i-2}^{i+2} h(x_j)}{\sum_{j=i-2}^{i+2} h_1(x_j)} \right) \quad (3.19)$$

Subsequent work demonstrated that the convergence rate of the iteration process could be improved if the summations in Eq. 3.19 were taken over nine channels instead of the original five and if the summation ratio was squared before multiplication by $f_1(x_j)$ (Dannefaer and Kerr 1975). The iteration pro-

cedure is stopped when the comparison of $h(x)$ and $h_N(x)$ yields a χ^2 value less than some predetermined minimum (Jackman et al. 1974) or when the sum of the squares of the deviations falls below some predetermined level (Dannefaer and Kerr 1975).

The main advantage of these iteratively based techniques is that a solution is obtained without any restriction on the shape of $f(x)$. While this is indeed an attractive feature of the method it also suffers from some inherent disadvantages. These disadvantages include the amount of computer time required, the possible dependence of the result on the initial estimate of $f(x)$, and the possibility of introducing large oscillations into the solution if the stopping criterion is selected with too small an error bound. This last difficulty is of course related to the mathematical nature of the incorrectly posed problem.

The iterative deconvolution technique essentially ignores the statistical nature of the problem. An alternate approach is to treat Eq. 3.4 as a problem of mathematical statistics and introduce a regularizer (a priori information) in the form of some probability distribution for $f(x)$ (Turchin et al. 1971). This is the method of statistical regularization which offers the advantage of error analysis. The result of this process is the most probable $f(x)$ for a given $h(x)$ measured with mean square errors $S(x)$ which are independent of x and normally distributed with zero mean (Goldanskii et al. 1978). The regularizer is a form of a priori information concerning the shape of $f(x)$ and hence somewhat restrictive. However, such an approach appears to yield reasonable results if a solution can be obtained using minimal a priori information concerning the smoothness of $f(x)$.

In 1981 the Fourier cut-integral method was introduced by Szotek and Chmielewski. In this technique Eq. 3.4 is rewritten as

$$f(x) = \frac{1}{2\pi} \int_{-\rho_0}^{\rho_0} e^{iwx} \frac{H(w)}{R(w)} dw \quad (3.20)$$

The difference in the equations is the introduction of finite limits of integration. If ρ_0 is then chosen small enough the solutions obtained are physically plausible. The mathematical explanation for this result is that the insertion of finite limits of integration forces the dispersion of $f(x)$ to remain finite. (Refer to Eq. 3.12 and the associated discussion). The problem associated with this method is that the optimum value of ρ_0 is not readily predictable. Approximations for $f(x)$ are obtained using different values for ρ_0 , and one must then select the "best" approximation to the true $f(x)$. This is typically done by convoluting the function with $r(x)$ and then comparing the result with $h(x)$. As ρ_0 becomes too large the solution begins to exhibit large oscillations as would be expected from the mathematical theory.

In 1982 Verkerk published an extensive mathematical treatment of the deconvolution problem. In this work he discusses the relative strengths and weaknesses of many of the currently employed deconvolution techniques. Verkerk then proposes a method which in many ways is very similar to the Fourier cut-integral method. The crux of this method is that the high frequency Fourier coefficients of $h(x)$ do not contain significant information and consequently only a limited number (say K) of Fourier coefficients $H(w)$ contain the essential information from measurement of $h(x)$. It should be pointed out that if $H(w)$ contains N Fourier coefficients then deleting the $N-K$ high frequency coefficients in the reconstruction of $f(x)$ is equivalent to inserting finite limits of integration in Eq. 3.4 as in the Fourier cut-integral method.

The deletion of the high frequency coefficients is equivalent to a rectangular low-pass filter and it is well known that the application of such

a filter to $F(w)$ will cause nonphysical oscillations in the approximation to $f(x)$.

In summary, there are two different types of errors associated with the estimate of $f(x)$: 1) statistical errors, which are amplified by the deconvolution operation and 2) systematic errors due to filtering, which are largest in the peak region and may cause nonphysical oscillations in the tails of the deconvoluted signal. Error type 1 increases as the number of Fourier coefficients used in reconstruction increases, while error type 2 decreases (Verkerk, 1982). Thus, by using such an approach the problem is reduced to selecting the optimum number of coefficients. One disadvantage of Verkerk's method, as with the Fourier cut-integral method, is that the procedure must be repeated several times for different numbers of coefficients until the optimum number is determined. It would be desirable to develop a simple one-step method to determine the appropriate number of coefficients to use in reconstructing $f(x)$ from $F(w)$, and indeed this is one of the primary advantages of the FFT/power spectrum deconvolution method which is described in the following section.

The FFT/Power Spectrum Deconvolution Method

The deconvolution method developed in this work is a fast Fourier transform (FFT) based method which is simple to execute, fast, easily automated, and assumes little or no a priori information concerning the shape of $f(x)$. The distinctive feature of this method is that the number of Fourier coefficients retained in the reconstruction of $f(x)$ is determined by examining the power spectrum of the experimental data. Using the observation that the power spectrum falls steeply to a minimum before rising due to the white noise component in the experimental data, the method truncates the Fourier

coefficients at this first minimum. The logic behind this approach is rather simple. Retaining fewer coefficients than this implies a smoothing of the deconvoluted spectrum and the loss of potentially valuable structural information. Adding more coefficients gains nothing because the signal-to-noise ratio is of order one at the minimum. In addition, truncating the coefficients at the point where the white noise begins to dominate forces the dispersion of $f(x)$ to remain finite.

With this brief introduction it is now possible to list the six steps which together constitute the FFT/power spectrum deconvolution method:

- 1) Both the raw data $h(x)$ and the resolution function $r(x)$ are background corrected.
- 2) The functions $h(x)$ and $r(x)$ are Fourier transformed using an appropriate FFT algorithm.
- 3) The Fourier coefficients of $h(x)$ are examined and those up to and including the first minimum in the power spectrum of h are retained, the rest are replaced by zeros.
- 4) The Fourier transform of $f(x)$ is obtained by the point by point division of the Fourier transform of $h(x)$ by the transform of $r(x)$.
- 5) $f(x)$ is obtained by the inverse FFT.
- 6) The solution is checked by forming the convolution of $f(x)$ with $r(x)$ and comparing the result with $h(x)$.

Each of these basic steps will now be described in further detail. Semiconductor detectors usually produce asymmetric γ -ray peaks with a non-linear underlying background. This is caused primarily by three processes: 1) incomplete charge collection, 2) electron escape from the active volume, and 3) scattering of γ -rays (Chaglar et al. 1981). This background component should be removed from the experimentally obtained energy distributions before

the deconvolution procedure is performed. The background correction routine employed in this work involves a least squares fitting of a linear function in both the low and high energy tail regions. The region on the low energy side of the peak spans from 486 to 497 KeV, while the high energy region extends from 534 to 542 KeV. The straight line segments fitted in these regions are extrapolated to 503 and 518 KeV respectively where they are joined by a third line segment to produce a simple background approximation (Jackman et al. 1974). The linear least squares analysis algorithm used in this work is a simplification of a higher order least squares routine by Gerald (1978). As in the work of Jackman et al. (1974), use is made of only the high energy half of the background corrected spectrum since it is known that incomplete charge collection of solid state detectors results in low energy tailing. In theory the spectrum should be symmetric about 511 KeV since statistically one should observe equal numbers of red and blue Doppler shifted γ -rays.

Before proceeding to the details of the FFT algorithm one important point requires explanation. In order to correlate MCA channels with a corresponding energy range, one must know the MCA energy resolution per channel as well as which channel corresponds to the center of the energy distribution and hence 511 KeV. The former value is determined as described in the experimental procedures. However, the center of the distribution must be calculated for each experimental spectrum. A simple centroid calculation is unacceptable since the higher background on the low energy side would bias the result. Similarly, simply selecting the channel with the maximum number of counts is undesirable since, due to the statistical nature of the experiment, the centroid channel and the peak channel are not necessarily the same. The technique used in this work is to determine the eleven channel region which contains the largest number of counts and call the middle channel of this region

the center of the distribution. In most cases, the channel corresponding to the center as calculated above was also the channel with the maximum number of counts.

Proper arrangement of the data string is required before proceeding to the FFT algorithm. Since this algorithm requires periodic data, the raw data are rearranged in the following way. The first datum point of the rearranged set corresponds to the center of the raw data string. The remaining rearranged data points numbered from 2 to $((N/2) + 1)$ correspond to the remaining values of the background corrected high energy half of the raw spectrum. It should be pointed out that N must satisfy the relationship $N = 2^m$ where m is an integer. Since the real data string rarely has exactly $((N/2) + 1)$ data values it is usually necessary to insert a string of zeros at the end of the data set to fulfill this requirement. In order to achieve periodicity, data point N should correspond to data point 2. In general the points from $((N/2) + 2)$ to N are defined in the following way:

$$g((N/2) + P) = g((N/2) + 2 - P) \quad (3.21)$$

where P varies from 2 to $(N/2)$. In the experiment performed in this work m was equal to eleven which corresponds to a total of 2048 data points (including the zerofill).

Once the functions $h(x)$ and $r(x)$ have been background corrected and properly arranged they are passed to the FFT algorithms. The FFT algorithms employed in this work are those developed by Cooley, Lewis, and Welch (1979). There are a number of other such algorithms available which should work equally well. In every case it is recommended that the Fourier coefficients be calculated with double precision accuracy. The advantage of using FFT's in place of discrete Fourier transforms (DFT) can be seen from the following example. For 2048 data points the DFT requires N^2 or $\sim 4.2 \times 10^6$ complex mul-

tifications while the FFT requires $2N \log_2 N$ or $\sim 4.5 \times 10^4$ complex multiplications. In this example the number of calculations required is reduced by about two orders of magnitude.

The justification for using only the Fourier coefficients up to and including the one corresponding to the first minimum in the power spectrum of $h(x)$ has been briefly discussed. Similar techniques are commonly employed in electronic signal processing and it can be shown that the number of coefficients retained is a measure of the frequency resolution. In the present case the resolution refers to the width of the lineshape components which can be resolved. The procedure by which the computer calculates the number of retained Fourier coefficients from $H(w)$ is as follows. Values associated with the power spectrum are obtained by multiplying each Fourier coefficient $H(K)$ by its complex conjugate. However, since the function $h(x)$ is even, the Fourier coefficients $H(w)$ are all real. Truncating $H(w)$ at the K corresponding to the first minimum in the power spectrum is equivalent to the requirement that the set of retained coefficients be monotonically decreasing, which is easily programmed by testing

$$H(w + 1) < H(w) \quad (3.22)$$

In this analysis only the first $(N/2) + 1$ Fourier coefficients are considered. The first coefficient corresponds to the D.C. component of zeroth frequency and the $N/2 + 1$ coefficient corresponds to the highest frequency available. It is well known that the remaining coefficients correspond to the negative frequencies and are in fact the complex conjugates of the first $(N/2 + 1)$ coefficients following the relationship $g(N/2 + P) = g^*(N/2 + 2 - P)$ for $P = 2$ to $N/2$. However since all the coefficients are real, no new information is to be gained by examining the negative frequencies.

Once the appropriate number of coefficients, say I , has been determined the remaining $N-I$ coefficients of $H(w)$ are set equal to zero before dividing $H(w)$ point-by-point by $R(w)$ and proceeding to obtain $f(x)$ by the inverse Fourier transform. The consequences of this truncation, or filtering operation are well known. See, for example, the discussion by Verkerk (1982). In general the process results in some systematic errors in which the peak values are underestimated and nonphysical oscillations may appear in the deconvoluted function $f(x)$. For Doppler-broadened positron annihilation spectra taken with our instrumentation this filtering error is negligible for Doppler spectra having more than 40K peak counts.

To check the accuracy of the function $f(x)$ requires the convolution of this function with $r(x)$ and the comparison of the resulting function with $h(x)$. The details of practical convolution techniques have been discussed by Lam *et al.* (1981), and the procedure used in this work is essentially the same.

A complete listing of the Fortran FFT/power spectrum deconvolution program is given in Appendix F.

Test of the Method

In order to explore the validity of the FFT/power spectrum method the following test was performed. The resolution function $r(x)$ was obtained from the 514 KeV gamma ray of ^{85}Sr , while the function $h(x)$ was measured for a neutron irradiated high purity single crystal sapphire sample. This sample had been irradiated in EBRII at 740°C to a fluence of 3×10^{21} neutrons/cm² with $E < 0.1$ MeV. Both $r(x)$ and $h(x)$ were then processed as described in the previous section. For this test of the method $f(x)$ was estimated from $F(w)$ using the first 101 low frequency Fourier coefficients, as selected by power spec-

tral analysis.

Figure 5 is a plot of the power spectrum for both $F(w)$ and $H(w)$. The filled circles represent the spectrum of the experimentally obtained function $h(x)$. Note the rapid decrease of about six orders of magnitude in power with increasing frequency. This power spectrum is about what would be expected from a wide-band-width stochastic process contaminated with white noise. This white noise component is associated with the band of frequencies to the right of the first minimum in the power spectrum of $h(x)$. Although the overall signal-to-noise ratio is very high, for frequencies in this white noise band the signal-to-noise ratio is less than one and therefore it is impossible to retrieve any structural information about the function $f(x)$ in this high frequency range. This suggests that only those coefficients to the left of the white noise band, that is to the left of the first minimum, be retained. To use less than this number of coefficients in reconstruction is undesirable since it is known that the errors associated with truncation, or filtering, increase with a decrease in the number of coefficients used.

The amplification of the statistical errors in $h(x)$ by the deconvolution procedure can be clearly seen in Figure 5. The open circles represent the spectrum of the deconvoluted function $f(x)$. Note the drastic increase in the power associated with the high frequencies of $f(x)$ as compared with the corresponding frequencies in $h(x)$. However, the low frequency coefficients to the left of the first minimum are well behaved. These observations are the foundation on which the FFT/power spectrum method is based.

It is not surprising to find that the number of retained Fourier reconstruction coefficients, as determined by power spectrum analysis, is a function of the number of peak counts in the raw data $h(x)$. Figure 6 is a semi-log plot of this relationship for irradiated sapphire. This figure sug-

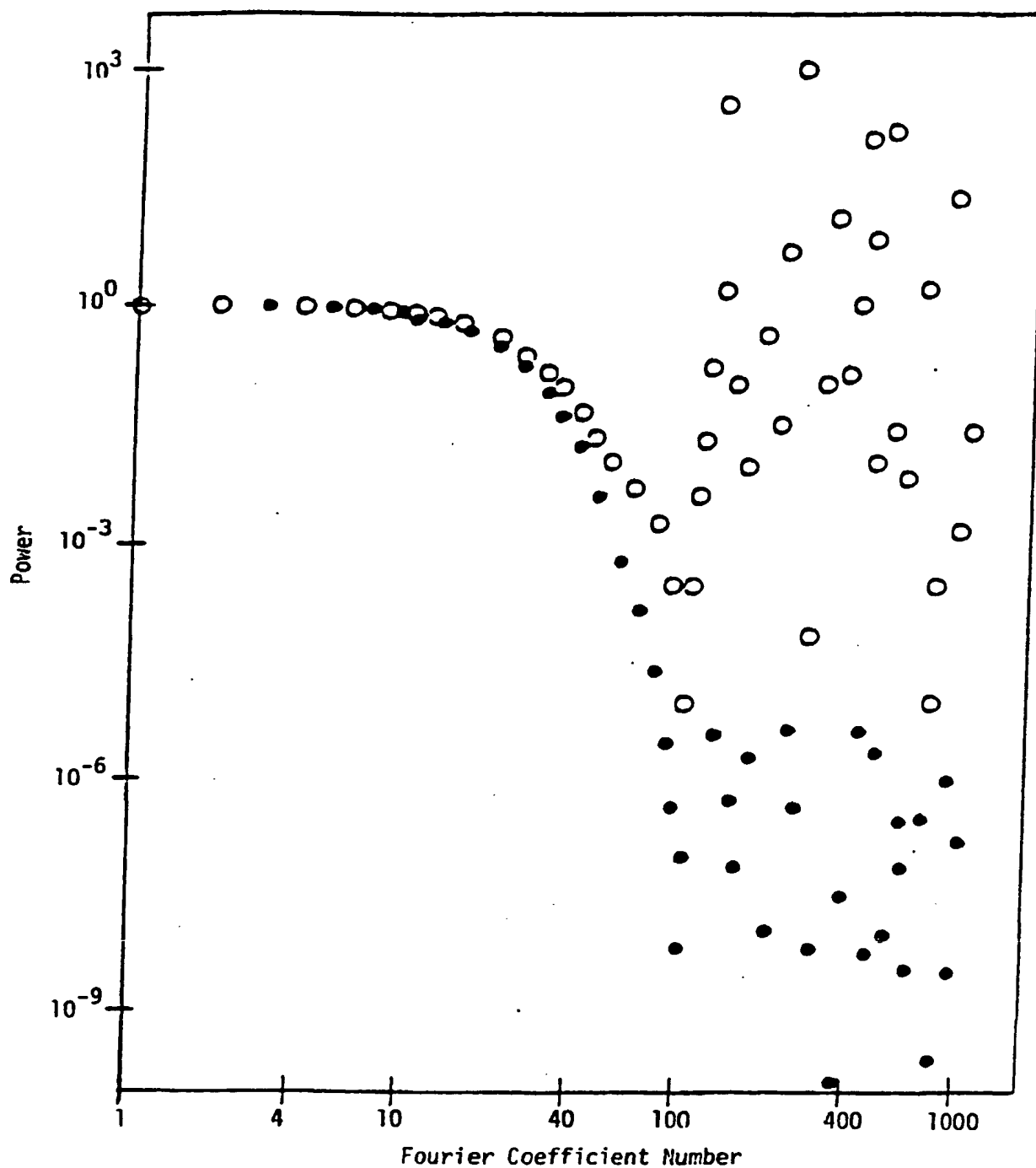


Figure 5. A Plot of the Power Spectrum of the Raw Data, $h(x)$, (Filled Circles), vs. the Deconvoluted Data, $f(x)$, (Open Circles).
 Note that increasing Fourier coefficient number corresponds to increasing frequency.

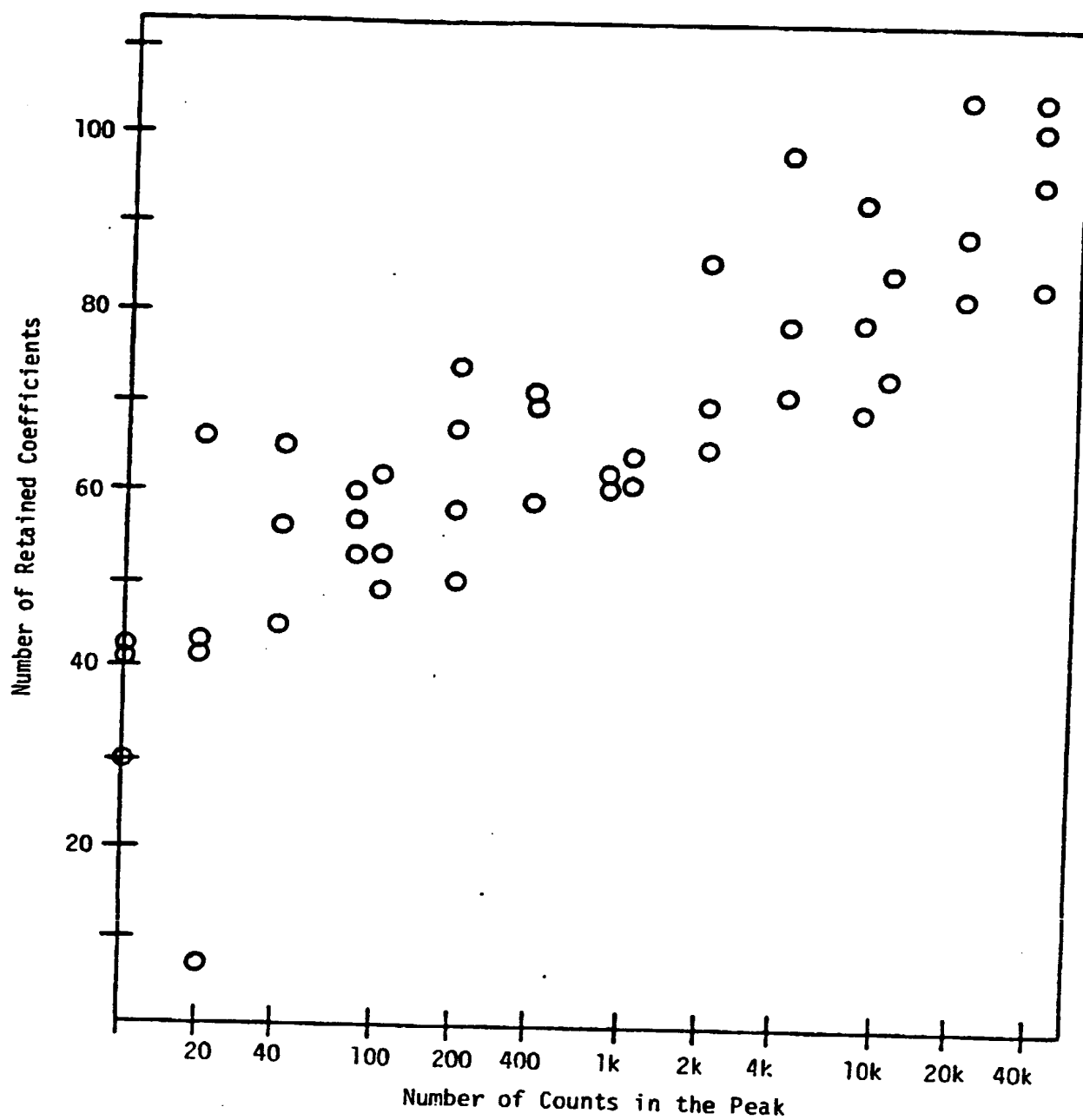


Figure 6. A Semi-Log Plot of the Number of Reconstruction Coefficients Retained by the FFT/PS Deconvolution Algorithm as a Function of the Number of Counts in the Peak Channel of the Raw Data. The Data is for Irradiated Sapphire.

gests that the relationship over this range of peak counts is an exponential of the form:

$$y \propto m \ln x \quad (3.23)$$

where y is the number of coefficients, x is the number of counts in the peak, and m is approximately equal to 7 for this data set. This curve demonstrates the high price one must pay in terms of data collection time to increase significantly the number of retained coefficients. Fortunately, our experience has shown that with the ~100 coefficients which are usually obtainable with 40K counts in the peak (30 minutes of data collection) the results obtained are very satisfactory.

Figure 7 is a comparison of the deconvoluted function $f(x)$ and the raw data $h(x)$ after background correction. The curves have been normalized to equal area. As expected, the deconvoluted curve is both sharper and smoother than the raw data. There appears to be a slight oscillation in $f(x)$ in the tail region. The quality of this estimate of $f(x)$ can be examined in the usual way by convolution with $r(x)$ to obtain an approximation $h'(x)$ to the original experimental function $h(x)$ as is shown in Figure 8. The overall quality of the fit is so good that on this scale it is difficult to see any differences between the raw spectrum and the convoluted spectrum. The one exception occurs in the peak region where several of the raw data points of $h(x)$ lie well below their counterparts in $h'(x)$. Careful examination of the shape of $h(x)$ in this region reveals some rather spurious changes in the slope of the spectrum. Physical constraints on the annihilation process suggest that, assuming no positronium formation, the annihilation spectrum should be relatively smooth in this region. This suggests that these slope changes in $h(x)$ are related to statistical counting errors. To test this idea two other

One of the theoretical advantages of deconvolution is a significant improvement in the resolution of DBPAS measurements. Figure 9 is a plot of the high energy half of a typical ^{85}Sr peak before and after deconvolution. The closed circles represent the raw data after background correction, while the open circles show the shape of the resolution curve after deconvolution using 243 coefficients. This is the number of coefficients selected by the FFT/PS method corresponding to the first minimum in the power spectrum for this data set. Note that the full width half maximum (FWHM) value for the raw data is ~ 1280 eV while the deconvoluted curve has a FWHM of ~ 320 eV. This corresponds to a factor of four improvement in resolution. However, this result is somewhat misleading in that for aluminum the number of retained coefficients is approximately 60-70. The triangles in Figure 9 show the resolution function after deconvolution using 70 retained coefficients. In this case the FWHM is ~ 576 eV corresponding to an improvement in resolution by a factor of ~ 2.2 . Clearly it can be seen that the improvement in resolution obtained by deconvolution using the FFT/PS method is a function of the number of retained coefficients, which in turn is directly related to the statistical quality of the raw data set (Schaffer et al. 1984). This implies that the data collection process should be carried out for sufficiently long times in order to obtain good counting statistics. (The counting error is proportional to $1/\sqrt{N}$, where N is the number of counts in the channel).

Unfortunately, counting for long times introduces another error source. This error source is related to instrumental electronic drift due, at least in part, to temperature fluctuations. There are two major ways in which other researchers have dealt with this problem. First, the accuracy of results can be improved by operating the entire DBPAS system within a temperature controlled ($\pm 0.2^\circ\text{C}$) atmosphere. The second method, usually used in

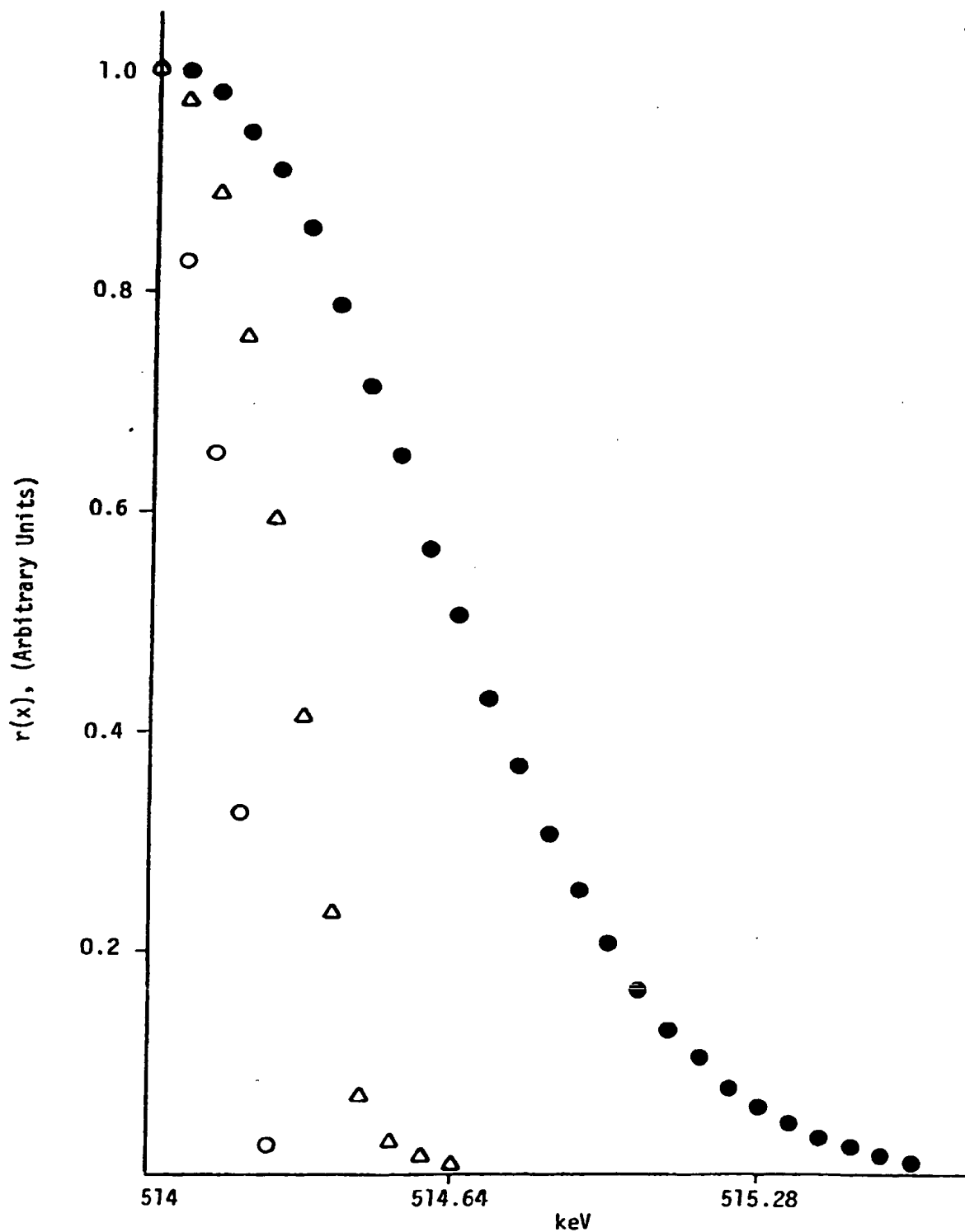


Figure 9. A Comparison of the Shape of the High Energy Half of the Resolution Function, $r(x)$, a) Before Deconvolution, (\bullet), b) After Deconvolution using 70 Coefficients (Δ), and c) After Deconvolution using 243 Coefficients, (\circ).

conjunction with the first, is to digitally stabilize the electronics. This digital stabilization is accomplished by simultaneously monitoring the 511 KeV annihilation line along with a suitably located monoenergetic gamma ray source such as the 478 KeV gamma ray from ^7Be . In this procedure a spectrum is collected for $\sim 100\text{S}$ and then the centroid of the 478 KeV peak is calculated. Subsequently, several other spectra are collected and their corresponding centroids also calculated. Next, each spectrum is linearly shifted such that all of the 478 KeV centroids coincide. Finally the 511 KeV peaks are summed to produce a DBPAS spectrum with as many total integrated counts as is necessary to obtain suitable counting statistics.

While temperature and/or digital stabilization should improve the reproducibility of DBPAS measurements, it is still possible to obtain meaningful results using unstabilized equipment. In this work neither of the stabilization techniques were employed, and the major consequence of such a procedure is an observable spread in the values of the lineshape parameters calculated for repeated DBPAS measurements of the same metallurgical sample. This problem will be discussed in greater detail in the sections of this chapter dealing with the separation of multiple defect types.

In order to minimize the change in the metallurgical defect structure of the samples as a function of time, all of the DBPAS measurements in this work were made at 77°K . Performing the measurements at liquid nitrogen temperatures raises an important theoretical question: is the assumption that the positrons are essentially at rest, with respect to the electrons, at the time of annihilation still valid? Previous experiments by Kubica and Stewart (1975) demonstrate that even at temperatures as low as 4.2°K the positrons reach thermal velocities prior to annihilation.

In order to determine the effect of measuring the annihilation

lineshape at 77°K an experiment was performed in which six DBPAS spectra were obtained for a well annealed pair of aluminum samples. Three of the measurements were made at 77°K and three at room temperature. The small deviation (of order $1/\sqrt{N}$) between the six spectra showed no correlation with measurement temperature. It was therefore concluded that decreasing the sample temperature from room temperature to 77°K would not affect the positron-electron annihilation procedure in any experimentally observable manner.

As mentioned in the experimental procedures the samples examined in this work were high purity aluminum disks heat treated to control defect type and concentration. It is assumed in the remainder of this work, without direct TEM evidence but based on the arguments presented in the experimental section, that one group of samples contained predominately monovacancies while a second group of samples possessed a defect structure dominated by prismatic dislocation loops. For each pair of disks three or four annihilation energy spectra were obtained, from which an array of lineshape parameters were subsequently extracted numerically. The lineshape parameters examined in this work include the first five even central moments of the energy distributions defined by the relationship:

$$m(I) = \frac{1}{N-1} \sum_{i=1}^N (x_i - \bar{x})^I f(x_i) \quad (4.1)$$

where N is the number of channels in the spectrum

\bar{x} is the channel corresponding to the spectrum centroid

$f(x_i)$ is the number of counts in channel i

and I is an even integer (2,4,6,8,10) corresponding to the first through the fifth even central moments

A second group of parameters is defined by the relationship:

$$x(I) = \left[\sum_{i=j}^{j+4} f(x_i) \right] / \sum_{i=\bar{x}}^{\bar{x}+59} f(x_i) \quad (4.2)$$

with j defined as $j = \bar{x} + 5(I-1)$

where $f(x_i)$ is the number of counts in channel i

\bar{x} is the channel corresponding to the spectrum centroid

and I is an integer from 1 through 12

For example, $x(1)$ is the ratio of the number of counts in the first five channel regions on the high energy side of the centroid (actually it includes the centroid) to the total number of counts in the high energy half of the spectrum. Similarly, $x(12)$ is the ratio of the number of counts in the twelfth five channel interval (to the right of the centroid) to the total number of counts in the high energy half of the spectrum.

The third, and final, group of lineshape parameters examined are the conventional "S" parameters (Mackenzie et al. 1970). These parameters are defined as the ratio of the number of counts in some central energy region to the total number of counts in the energy spectrum. The width of the energy window used to define the S parameter is selected so that the value of S is in the range 0.4 - 0.6 (Smedskjaer and Fluss 1983). In this study three S-parameters (S(1344), S(1472), and S(1600)) were examined with respective central energy windows of 1.344, 1.472, and 1.600 KeV.

These parameters were calculated for both the background corrected raw data and for the deconvoluted data. Hence a total of forty lineshape parameters were calculated for each DBPAS measurement.

Figure 10 is a plot of the parameter $x(1)$ for the deconvoluted data. The open circles represent the values of this parameter for the "as quenched" samples (predominately monovacancies). The filled circles correspond to the

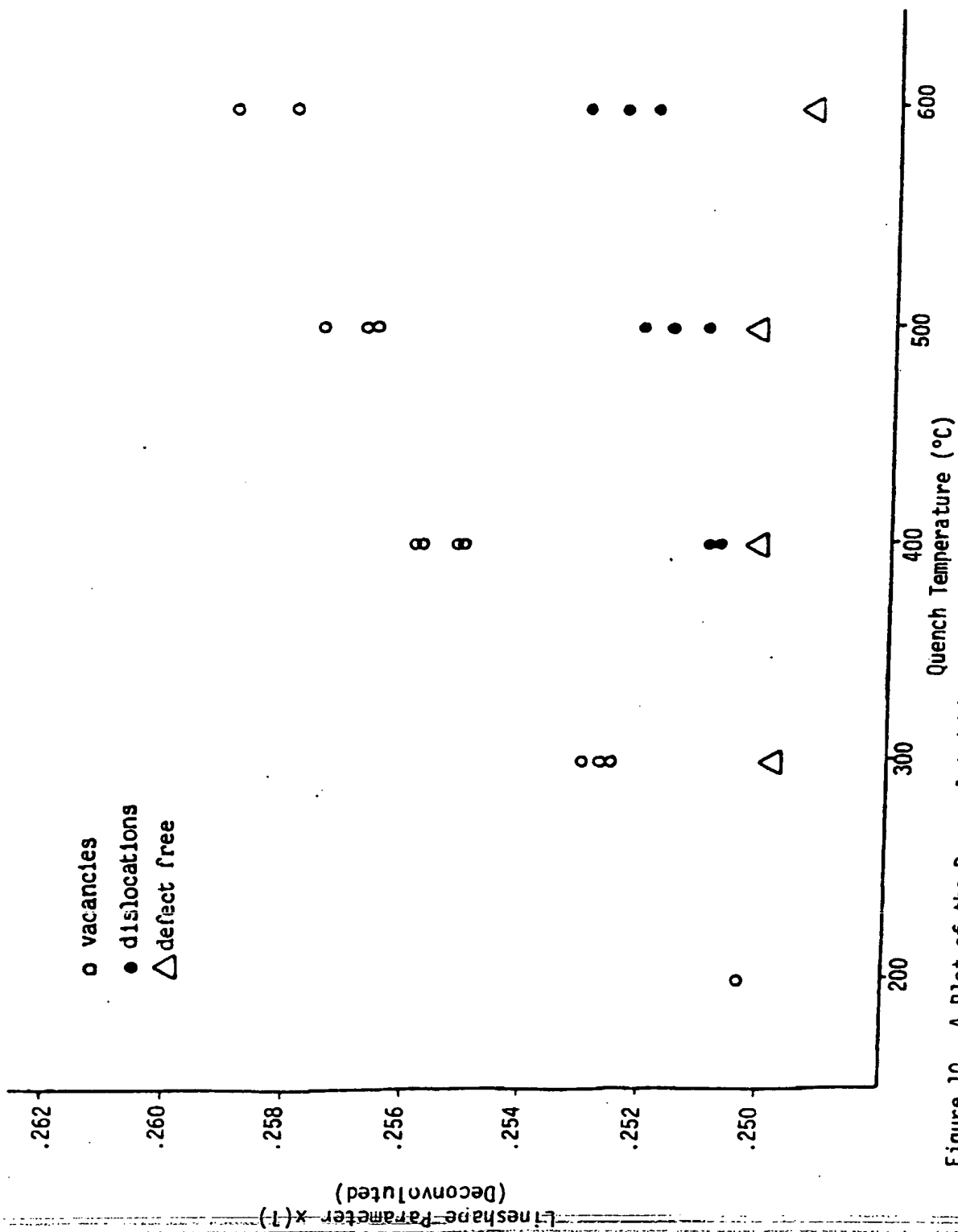


Figure 10. A Plot of the Deconvoluted Lineshape Parameter $x(1)$ as a Function of Quench Temperature.

low temperature anneal samples (prismatic dislocation loops), and the triangles represent the samples after the high temperature anneal (the essentially defect free state). Note that the numerical value of $x(1)$ increases with quenching temperature for both defect types. This trend is in agreement with theoretical predictions since an increasing defect concentration results in a higher probability of annihilation with lower kinetic energy conduction electrons, corresponding to a more narrow energy spectrum, and hence a larger value for $x(1)$. The equations used to predict the theoretical defect concentrations for both the vacancies and the prismatic dislocation loops as a function of quenching temperature are discussed in Appendix G.

Figure 10 demonstrates that DBPAS measurements are sensitive to the presence of both vacancies and dislocations in high purity aluminum. This result is, of course, a necessary prerequisite for the possibility of DBPAS measurements being able to distinguish between the defect types. From this plot it is possible to perform some semiquantitative analysis and estimate some physical properties of aluminum. For example, one can estimate values of the "cross section" for the trapping of a positron by both vacancies and dislocations in aluminum. The accuracy of these estimates is limited by the reproducibility of the DBPAS measurements as well as the need for some independent information such as the lifetime of positrons as a function of defect type.

In 1972 Cotterill et al. published a paper in which they examined the average positron lifetime, τ_{avg} , on a set of aluminum samples very similar to the ones studied in this work. Their work clearly demonstrated that positron lifetime experiments were sensitive to both vacancies and dislocations in aluminum. Before discussing the similarities between their work and the ~~current experiments it is important to demonstrate the relationship between~~

the parameters τ_{avg} and $x(1)$. In a review article by Sieger (1980) it is shown that:

$$\tau_{avg} = (1 - A_t)\tau_b + A_t\tau_t \quad (4.3)$$

where τ_b is the lifetime in the bulk material

τ_t is the lifetime in the trapped state

and A_t is the probability that the positron annihilates from the trapped state

Similarly, Sieger demonstrates that:

$$F = (1 - A_t)F_b + A_tF_t \quad (4.4)$$

where F is any characteristic shape parameter obtained from the analysis of DBPAS measurements

F_b is the value of the parameter in the bulk state

and F_t is the value of the parameter in the trapped state

Since the parameter $x(1)$ can be shown to be equivalent to an "S" type parameter, and since an "S" type parameter is a common characteristic line-shape parameter, Eq. (4.4) can be rewritten as:

$$x(1) = (1 - A_t)x(1)_b + A_tx(1)_t \quad (4.5)$$

where $x(1)_b$ is the value of the parameter in the bulk state

and $x(1)_t$ is the value of the parameter in the trapped state

Clearly a comparison of Eq. (4.3) and Eq. (4.5) demonstrates the similarity between τ_{avg} and $x(1)$.

With this in mind it is not surprising to find that plots of τ_{avg} vs. quench temperature (T_Q) and $x(1)$ vs. T_Q share many common characteristics. (The τ_{avg} plot used for comparison is Figure 2 in the work of Cotterill et al., 1972). In both figures the T_Q at which the vacancy concentration is large enough to affect the measured parameter is $\sim 200^\circ\text{C}$. The saturation value of both τ_{avg} and $x(1)$ for vacancies occurs at $T_Q = 600^\circ\text{C}$. The curve through

the points corresponding to vacancies is sigmoidal in shape for both the lifetime and deconvoluted DBPAS measurements. As for the points corresponding to samples with prismatic dislocation loops, the value of both parameters initially deviates from their bulk values for samples annealed after a quench from $\sim 400^\circ\text{C}$. Neither parameter reaches a saturation value for dislocations within the temperature range examined in this work.

Figure 10, therefore, shows not only the ability of deconvoluted DBPAS measurements to detect the trapping of positrons by both vacancies and dislocations in aluminum, but also qualitatively verifies the theoretically predicted equivalence of the lifetime parameter τ_{avg} and the Doppler parameter $x(1)$.

Figure 11 is a plot of the same lineshape parameter, $x(1)$, vs. T_Q for the background corrected raw data, i.e. the same data as shown in Fig. 10 but before the deconvolution procedure. Note the general similarity between these two figures. Careful examination of the raw data shows that the points corresponding to the 400°C quench are systematically displaced. That is, the entire group of five data points seems to be "too high" as compared with the rest of the data. To understand the cause of this shift it is necessary to examine the shape of the instrument resolution function $R(x)$.

During the course of these experiments the instrument resolution was periodically checked by collecting an energy spectrum for ^{85}Sr . The monoenergetic line is broadened due to the physical characteristics of the DBPAS system as previously described. This broadened energy line serves as the resolution function, $R(x)$, in the FFT/PS deconvolution procedure. It also describes the amount by which the undistorted energy spectrum is broadened by the instrumentation.

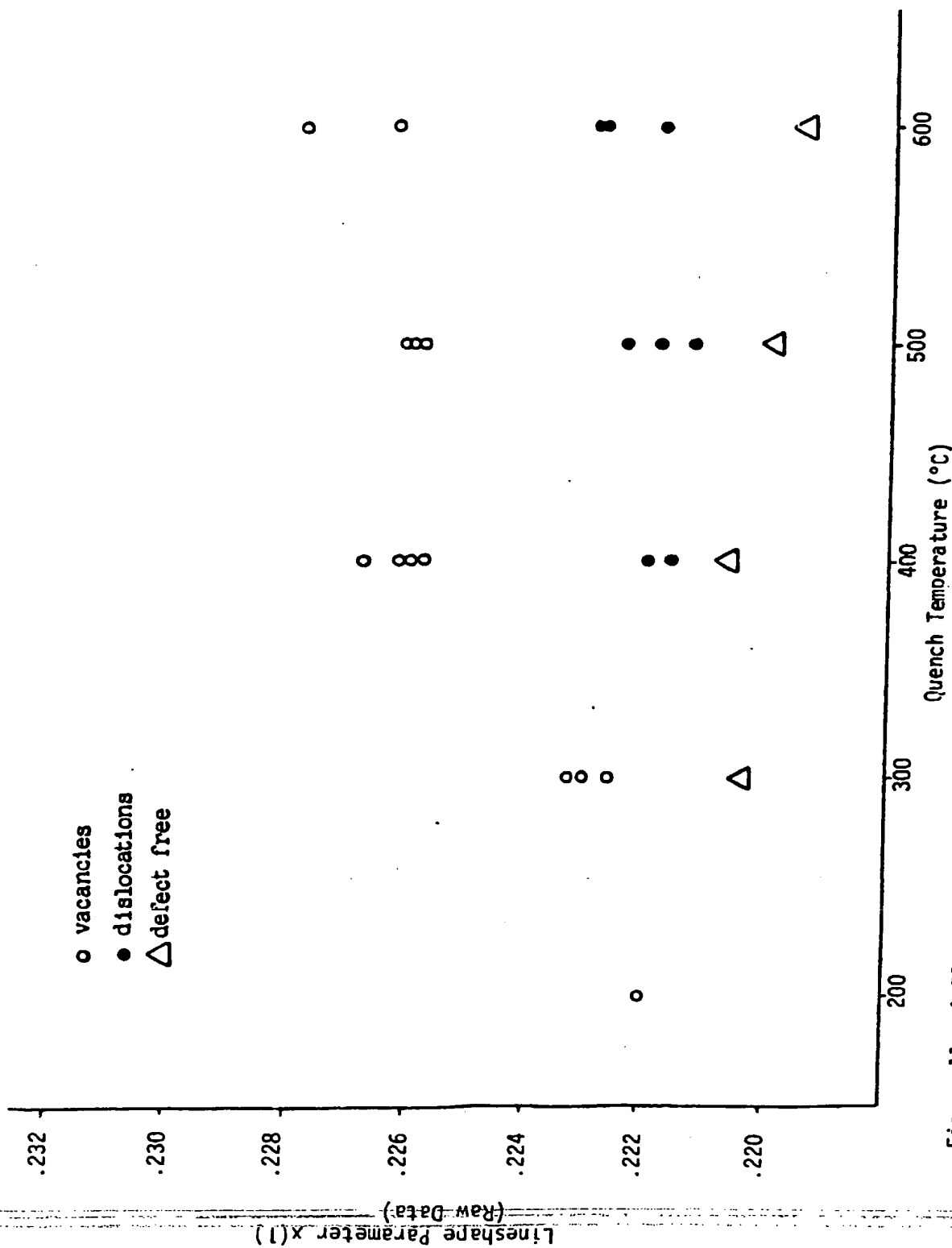


Figure 11. A Plot of the Raw Data Lineshape Parameter $x(1)$ as a Function of Quench Temperature.

Figure 12 shows two such resolution spectra. The open circles represent the instrument resolution corresponding to the DBPAS measurements for the samples quenched from 400°C. The filled circles represent a resolution function which is characteristic (within statistical error) of the resolution functions for all of the remaining data points. This comparatively large shape change in the function $R(x)$ was apparently caused by a power failure in the laboratory. Note that the Function $R(x)$ corresponding to the 400°C samples (henceforth termed SR85OLD) is more sharply peaked, and therefore more narrow, than the other resolution function (SR85NEW).

The physical significance of the change in resolution function is as follows. An observed energy spectrum will be broadened in two ways. The first way is by a decrease in the concentration of vacancy type defects, in the sample being examined. The second broadening mechanism is, of course, the broadening due to the instrumentation. Now, if the second source of broadening remains essentially constant, then changes in the width of the observed spectra may be attributed to changes in defect concentration. On the other hand, if the broadening due to the instrumentation decreases, and this error source is not properly removed, the observed spectrum will be artificially narrow and its apparent defect concentration will be too great. Thus, if the data for the 400°C samples are collected with an artificially narrow resolution function, i.e. SR85OLD, their apparent defect concentration will be greater than they should be.

Of particular significance is, that while a change in experimental conditions can alter the shape of the resolution function and thereby distort the values of lineshape parameters calculated for the raw data, the deconvolution routine, when supplied with the appropriate $R(x)$ function, automatically yields the desired results. This illustrates that for reproduc-

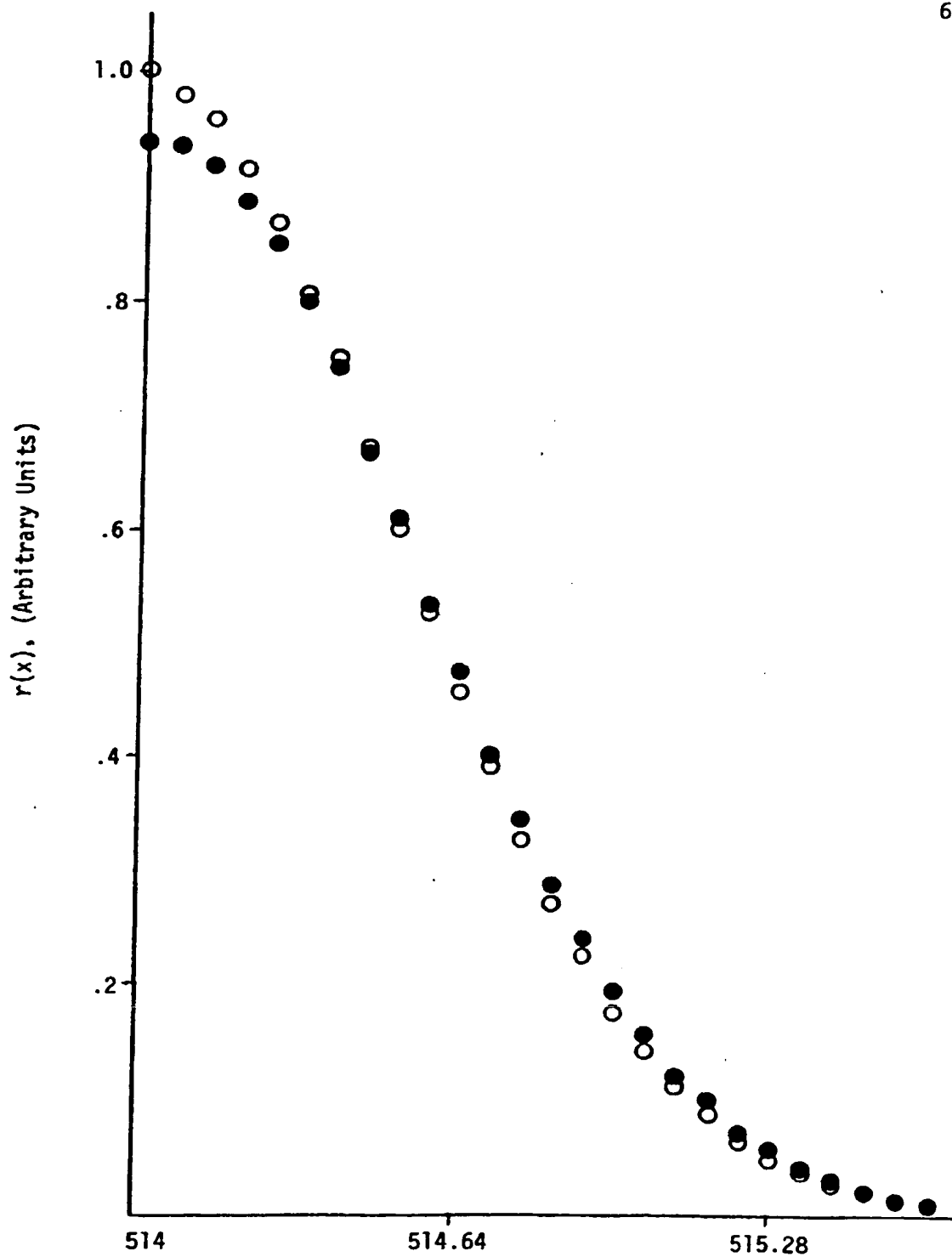


Figure 12. A Comparison of the High Energy Half of Two Resolution Functions, $r(x)$, Collected at Different Times During a Series of Experiments. The Two Functions are Referred to in the Text as SR35NEW (●) and SR85OLD (○).

bility the deconvolution of DBPAS measurements should be considered. In addition, as mentioned previously, since deconvolution removes the instrumental effects it should yield lineshape parameters which are directly comparable between different laboratories.

Despite the advantages of deconvolution it is important to remember that this technique does, of course, have its limitations. In DBPAS measurements there are several sources of experimental error, each of which has a corresponding time scale. The magnitude of this time scale is the overriding factor in determining the applicability of deconvolution techniques in minimizing the specific error in question. For example, any change in experimental conditions which can be treated as a step function, that is, by changing from one constant value to another constant value in a very short period of time, can be easily treated by deconvolution. Such "error" sources include the accidental (e.g. power failure) or intentional changes in the electronic amplification of the energy signal. To correct for such a change one simply needs to collect a resolution function before and after the event and use the appropriate $R(x)$ in the deconvolution algorithm.

On the other hand, error sources having a time scale approximately equal to the time required to collect a data set (tens of minutes) can not be corrected by deconvolution alone. Examples of such possible error sources include line voltage fluctuations, temperature variations, and electronic drift. These error sources may cause the centroid of the resolution function to vary during the collection period, resulting in a composite $R(x)$ which is artificially broad. In addition, even if the raw data set to be deconvoluted and the function $R(x)$ are collected in rapid succession the amount of centroid drift for the two energy spectra may well be uncorrelated. This type of error source requires a different means of correction. The DBPAS measurements

should be performed in a temperature controlled laboratory. Also, digital stabilization, as described previously, should be used to control centroid drift.

The final error type is the small time scale or high frequency class. An error source such as sixty-cycle electrical noise, if it were present, should average to zero over the time required to collect a data set. In addition, a high frequency error source should have a similar effect on both the resolution function and the DBPAS energy distribution.

In order to judge the effectiveness of deconvolution in eliminating experimental error it is necessary to define some quantitative measure of this error. The predominant manifestation of experimental error appears as a spread in lineshape parameter values calculated for multiple DBPAS measurements on the same samples. Figure 13 is a plot of the parameter $x(1)$ vs. T_Q for the deconvoluted data, note the spread in values of $x(1)$ for a given defect configuration.

In an attempt to evaluate the performance of the deconvolution algorithm the following parameters are introduced (see Figure 13 for a physical interpretation).

- 1) $\Delta P_V/P_0$ is a measure of the sensitivity of this parameter to the existence of vacancies.
- 2) $\delta P_V/\Delta P_V$ is a measure of the error associated with the spread in values of this parameter for vacancies.
- 3) $\Delta P_I/P_0$ is a measure of the sensitivity of this parameter to the existence of dislocations.
- 4) $\delta P_I/\Delta P_I$ is a measure of the error associated with the spread in values of this parameter for dislocations.

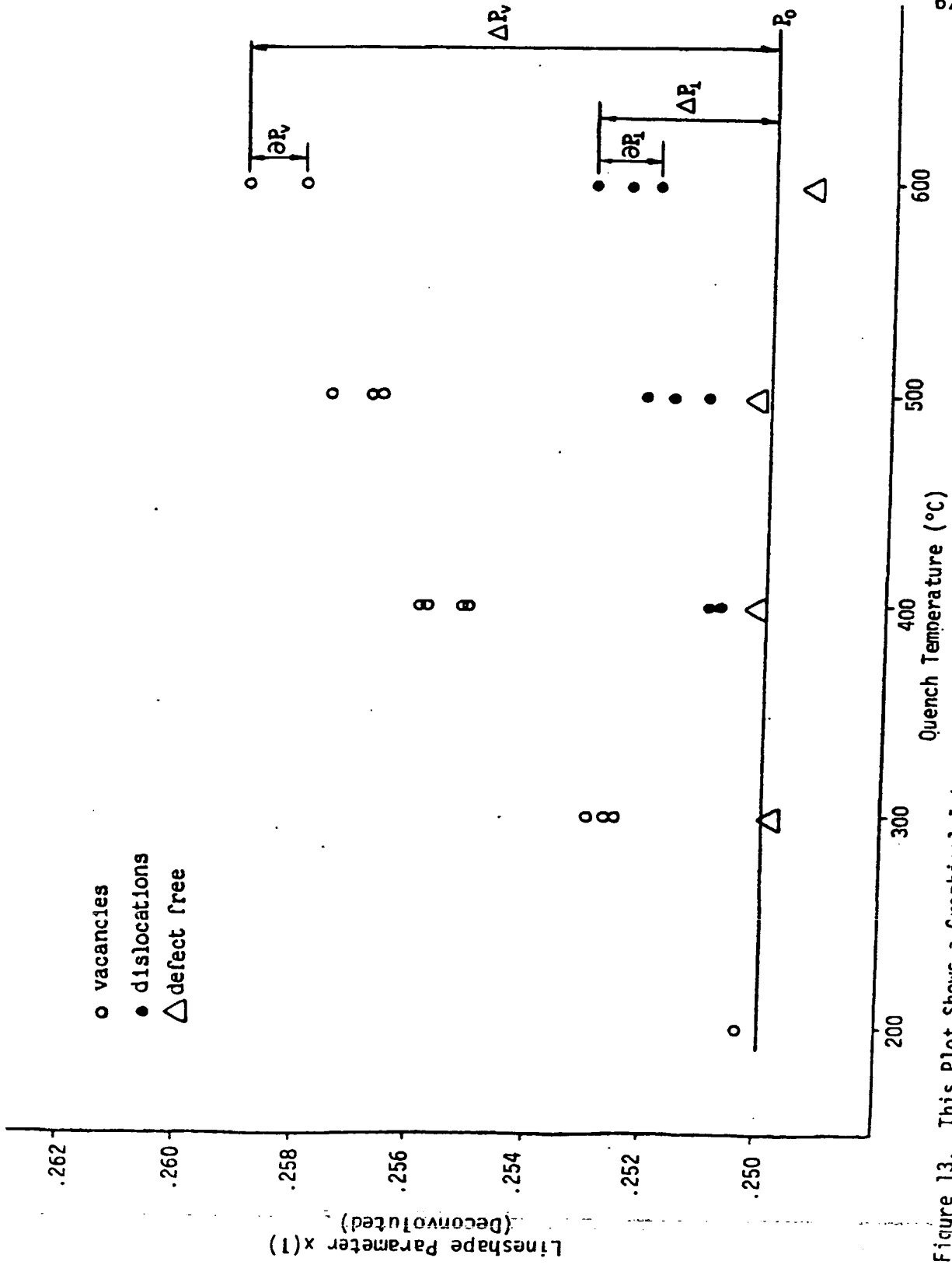


Figure 13. This Plot Shows a Graphical Interpretation of the Sensitivity and Error Parameters Discussed in the Text

Clearly, it is desirable for the sensitivity ($\Delta P/P_0$) to be as large as possible and the error ($\delta P/\Delta P$) as small as possible for both defect types. A comparison of these quantities calculated from the deconvoluted and the raw data is shown in Table 1. Note that for all four of the lineshape parameters listed the sensitivity ratio is higher and the error ratio is lower for the deconvoluted data than for the raw data. This analysis encourages the further use of the deconvolution procedure to improve the quality of the results obtained from DBPAS measurements.

A tentative explanation for the apparent improvement in sensitivity and accuracy of the deconvoluted results is based upon trends in the shape of the energy spectrum before and after the application of the FFT/PS analysis. Figure 14 shows the high energy half of the peak region for an Al sample quenched from $\sim 600^\circ\text{C}$. The deconvoluted spectrum is, of course, more narrow than the raw data but note that it is also smoother (due to the filtering of the high frequency components). One explanation for the comparatively large error ratios of the raw data is that they are related to the statistical counting errors in the peak region of the spectrum. If this is indeed the case it is not surprising to observe a decrease in the error ratio after the filtering of the high frequency components. However, the most probable explanation for the increased sensitivity resulting from deconvolution is related to the removal of the "broadening" action of the experimental instrumentation. Recall that the major effect of the instrumentation is to spread counts from one channel into several adjacent channels. Therefore, the true lineshape changes in the annihilation energy distribution, caused by the trapping of positrons at defects, are spread out over a much larger number of channels in the raw data. The deconvolution procedure corrects for this effect and in so doing restores some of the details of the "true" annihilation

Table 1

		<u>x(1)</u>	<u>x(2)</u>	<u>S(1344)</u>	<u>S(1600)</u>
DEC _v	$\frac{\delta P_{\max}}{\Delta P}$.111	.167	.183	.215
DEC _v	$\frac{\Delta P}{P_o}$.0360	.0263	.0325	.0279
DEC _l	$\frac{\delta P_{\max}}{\Delta P}$.315	.320	.331	.581
DEC _l	$\frac{\Delta P}{P_o}$.0124	.0110	.0119	.0106
ND _v	$\frac{\delta P_{\max}}{\Delta P}$.181	.235	.235	.231
ND _v	$\frac{\Delta P}{P_o}$.0348	.0165	.0256	.0207
ND _l	$\frac{\delta P_{\max}}{\Delta P}$.471	.938	.555	.585
ND _l	$\frac{\Delta P}{P_o}$.0155	.0077	.0100	.0078

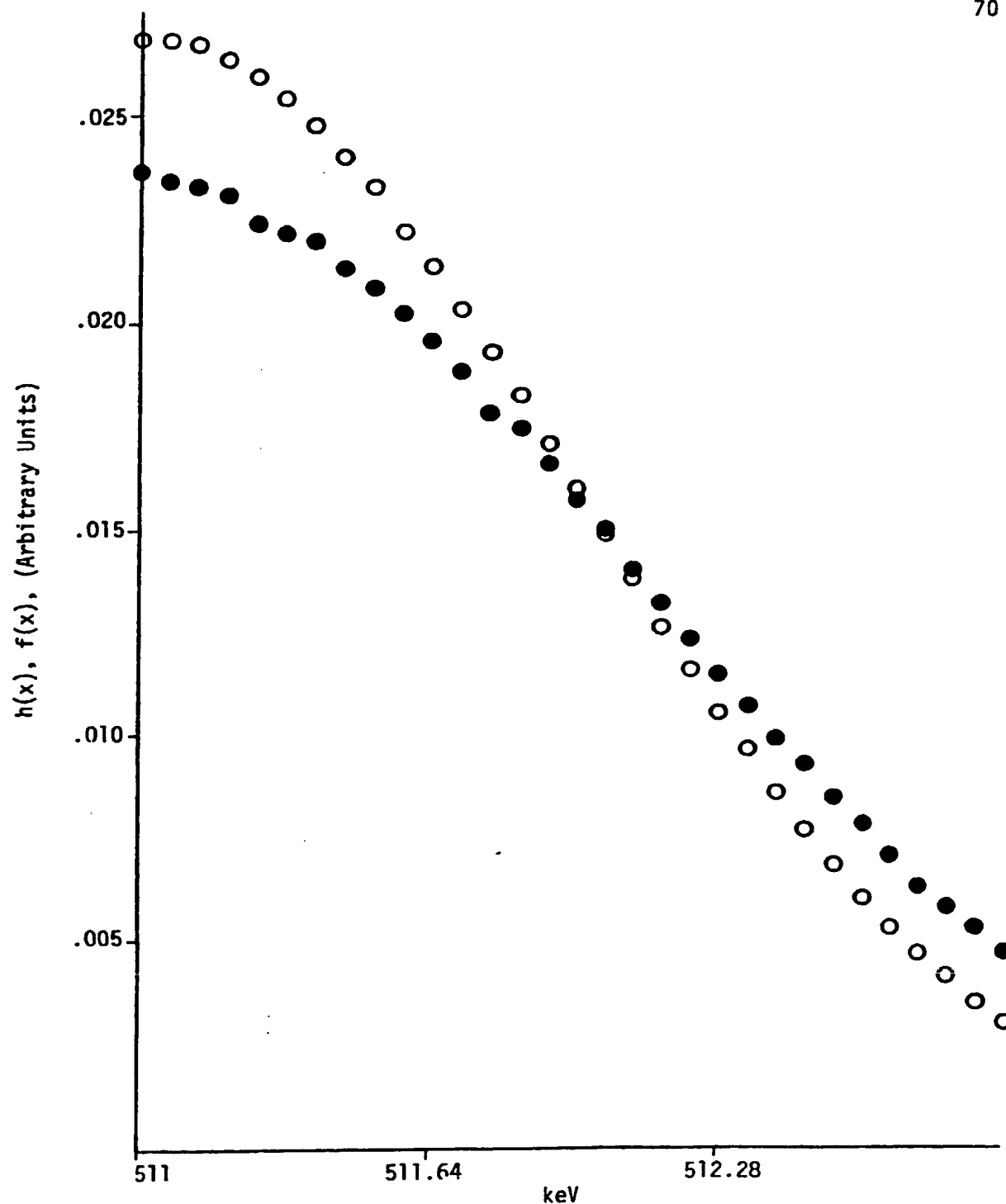


Figure 14. A Comparison of the High Energy Half of the Peak Region for $h(x)$, the Raw Data, (\bullet), and $f(x)$, the Deconvoluted Data, (\circ), for an Aluminum Sample Quenched from 600°C.

energy distribution. The net result is an increase in defect sensitivity. It should be mentioned that the magnitudes of the enhancement in sensitivity and accuracy due to deconvolution noted in this work are consistent, but small. However, from this work alone it is not possible to estimate the effect of temperature and electronic drift upon the results. It would be extremely enlightening to repeat this analysis employing a temperature controlled and digitally stabilized system.

Before moving on from the topic of parameter sensitivity and accuracy, one more pertinent observation should be discussed. Figure 15 is a plot of the error ratio, $\delta P/\Delta P$, calculated separately at each quenching temperature (the parameter being examined is $x(1)$). Several trends are apparent. First, it is clear that the error associated with the dislocations is larger than the error associated with vacancies. This trend may be a direct consequence of the size of the denominator, ΔP , which is smaller, at a given quench temperature, for samples with dislocations than for the corresponding samples with vacancy type defects. This observation is however somewhat deceptive in that the horizontal axis of Figure 15 is T_Q and not defect concentration. A meaningful comparison of parameter sensitivity between defect types should be made using equivalent defect densities. Unfortunately, the dislocation densities which can be introduced by this thermal treatment are not large enough for direct comparison. In addition, it should be mentioned that the trapping of positrons by dislocations may be somewhat more complicated than trapping by vacancies. This idea is discussed in detail by Martin and Paetsch (1972). Very briefly, it may be that the depth of the potential well associated with a prismatic dislocation loop is such that detrapping of the positron, due to local thermal excitations, becomes significant. If this is indeed the case, the interpretation of DBPAS data for low prismatic dislocation loop densities

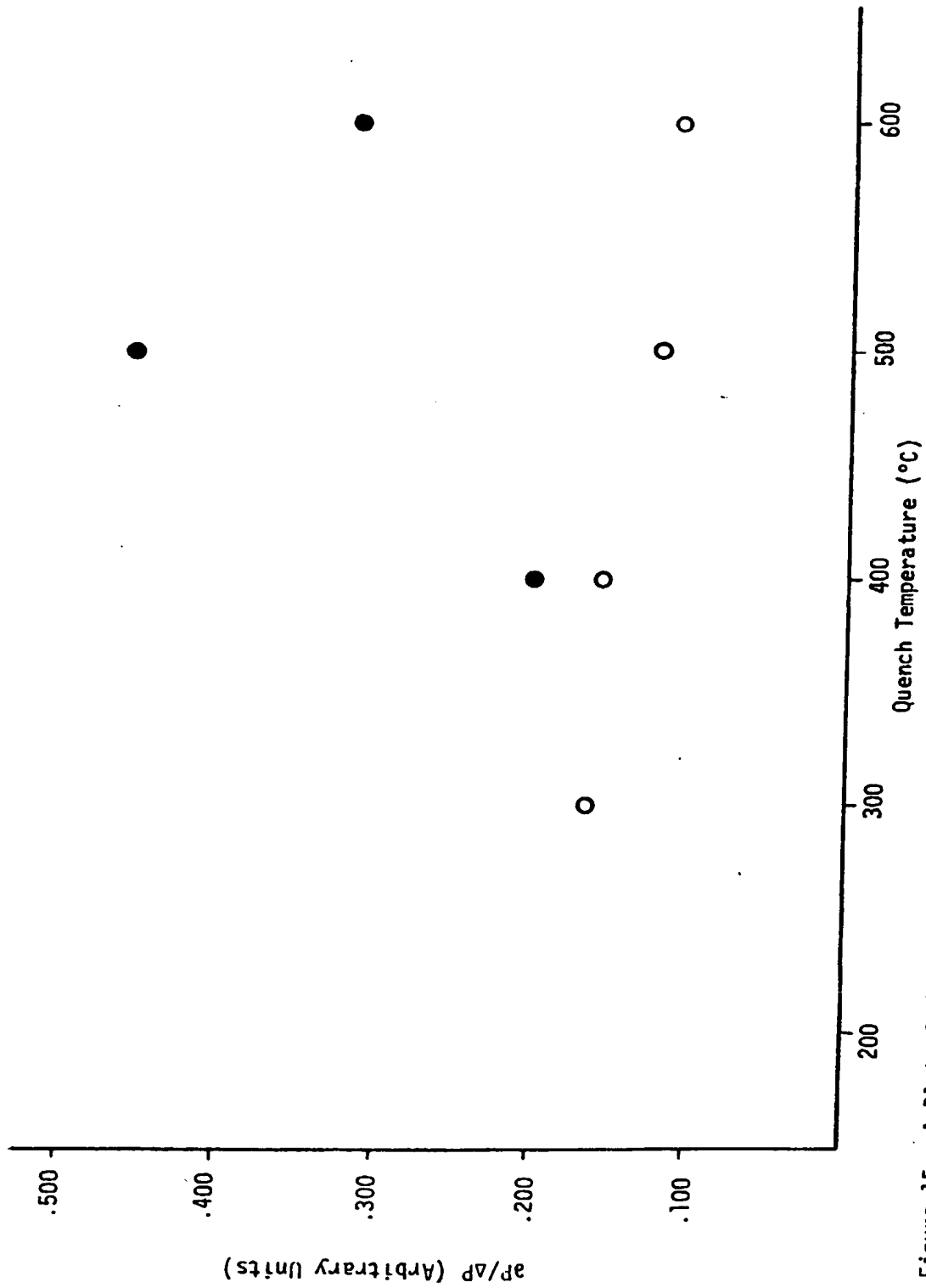


Figure 15. A Plot of the Error Parameter, $\Delta P / \Delta P$, for Both Dislocations (●) and Vacancies (○), as a Function of Quench Temperature for Aluminum Samples.

becomes more complicated. Clearly, additional experimental data is required to determine the exact reason for the observation that the error parameters are larger for the samples containing primarily dislocation loops than for the samples dominated by vacancy type defects.

Another interesting feature of Figure 15 is the relatively constant value of $\delta P/\Delta P$ for vacancies. This implies that the spread in the data decreases with the quenching temperature, since clearly ΔP decreases with T_Q . One possible explanation for this observation is related to the shift in the centroid of the experimentally obtained spectrum due to temperature and/or electronic drift. The explanation is that a centroid shift changes the peak shape of a broad and flat spectrum (low defect concentration) to a lesser extent than that of a narrow and sharp spectrum (high defect concentration). This is, of course, an extremely qualitative argument but it does predict that in a temperature/digitally controlled series of experiments the relative size of the error bars associated with the high defect concentration samples should decrease.

The preceding discussion has demonstrated the utility of deconvolution in DBPAS measurements. In summary, the use of the FFT/PS method improves the sensitivity and the relative error of the calculated lineshape parameters. In addition, deconvolution automatically corrects for a wide range of error sources which result in changes in the instrument resolution function. Deconvoluted lineshape parameters should be more directly comparable between different laboratories and, in addition, offer the potential ability to resolve fine structure in the energy spectrum which is unavailable from direct observation of the raw data. There is strong evidence (see for example Hood and Schultz, 1980) suggesting that the use of both temperature stabilization and digital stabilization, to control centroid drift, should significantly improve

the accuracy of the results.

It is interesting to note the conditions under which the undeconvoluted raw data has yielded reasonable results in the past. The main requirement is, of course, experimental conditions which yield a nearly constant resolution function, $R(x)$. As one would expect, temperature and digital control as well as performing the series of experiments as close together in time as possible, both tend to help yield reasonable results for the raw data. In addition, the use of "S" type parameters, which are essentially area integrals over large energy windows, will be affected only slightly by the "spreading" action of the instrumentation. The major advantages one gains by deconvolution are: 1) the ability to compare more accurately results for a wide variety of experimental conditions and, 2) the possibility of observing a more detailed structure of the positron-electron annihilation energy spectrum.

The Separation of Multiple Defect Types

The previous discussion has demonstrated that deconvoluted DBPAS measurements are able to detect the presence of both vacancies and dislocations in high purity aluminum. The evidence for this statement comes from controlled laboratory experiments using samples with reasonably well characterized defect distributions. In order for DBPAS measurements to become useful as an NDT tool in industrial applications it is important for the technique to be able to distinguish between multiple defect types. The reason for this requirement is that in a practical application one may require information about a particular defect type while being comparatively unconcerned with other defect types. For example, if one is interested in hydrogen embrittlement of high strength steels the "masking" of vacancies by nascent hydrogen may be of primary importance while slight variations in dislocation density may have relatively little significance.

Before discussing the results of this investigation to determine the ability of DBPAS to separate defect types a brief review of previous work in this area will be presented. The basic concept is that no two defect types will have identical electron configurations associated with them. That is, the distribution of electrons (both in terms of electron density and momentum) in the neighborhood of a single vacancy will be different than in the neighborhood of a dislocation core. Qualitatively the atmosphere will be the same, i.e. a decrease in electron density and a lower average electron momentum, but quantitatively, the measured lifetimes and fine structure of the momentum distribution should be different.

This variation in electron distribution has been verified repeatedly in the case of lifetime measurements. For example, Fluss et al. (1978) report a lifetime of ~ 244 ps for positrons trapped at a vacancy in aluminum while Hautajarvi et al. (1970) give the value of ~ 229 ps for a dislocation in the same material. It should be mentioned that the accurate determination of multiple lifetimes from a single experiment requires some rather involved calculations. The complexity of the procedure increases rapidly with the number of unconstrained components one attempts to resolve and, for crystalline materials, the results are questionable if more than two defect types are considered.

An alternate method of analyzing lifetime data is to calculate a single lifetime component, known as the "average" lifetime, for a sample containing multiple defect types. This approach simplifies the calculations and finds its greatest utility in experiments in which the concentration of one defect type is varying over a wide range of values while the concentrations of the other defect types remain relatively constant. Of course, such an approach results in the loss of the ability to separate defect types.

In the case of DBPAS measurements there have been fewer attempts to distinguish between different defect types. The most notable exception is the work of Mantl and Triftshauser (1978) which will be discussed in a following section. There are at least two major reasons for the lack of work in this area. The first reason is related to the comparatively poor energy resolution of the DBPAS technique. Because of the smoothing action of the instrumentation the fine structure of the energy distribution may have been hidden in previous experiments. In addition, even a slight change in the instrument resolution function during a series of experiments could mask the subtle changes in lineshape required to separate defect types. Although temperature and digital stabilization of the electronics would improve the situation, such a procedure does not address the issue of the smoothing action of the instrumentation. It is the use of deconvoluted data which offers the possibility of examining the fine structure of the electron momentum distribution.

As mentioned in the introduction, the most commonly reported Doppler lineshape parameter is the MacKenzie "S" parameter (1970). This lineshape parameter is defined as the ratio of counts in some central region of the DBPAS energy spectrum to the total number of counts in the spectrum. Since it is known that the energy spectrum becomes more sharply peaked with increasing vacancy type defect concentration it follows that the numerical value of "S" should be proportional to the total vacancy type defect concentration. The disadvantage of using this lineshape parameter is that it is unable to distinguish between multiple defect types. For example, if both monovacancies and edge dislocations are present in a sample both defect types will tend to increase the value of "S", however, it will be impossible to separate the relative defect concentrations solely from the calculated value of "S".

Mantl and Trifthauser (1978) developed a method for separating the effects of multiple defect types from experimentally obtained DBPAS data. To accomplish this they introduced a new lineshape parameter, I_c , defined as the ratio of the sum of the number of counts in two regions, (one on the low energy side and one on the high energy side of the peak) divided by the total number of counts in the spectrum. This lineshape parameter, which in this work will be referred to as the wing or "W" parameter, can be shown to decrease with increasing vacancy type defect concentration. When analyzed separately the "W" parameter suffers from the same disadvantages as the "S" parameter in that it is incapable of separating multiple defect types. However, Mantl and Trifthauser recognized that the combined use of "S" and "W" could yield useful results.

In Appendix H the derivation of their defect specific "R" parameter is recreated. To summarize, it can be shown that in theory the "R" parameter, as defined below, is concentration independent, but characteristic of the type of trapping site involved (Mantl and Trifthauser 1978). The "R" parameter is defined as:

$$R = |(S - S_B)/(W - W_B)| \quad (4.6)$$

where S is the "S" parameter for a given specimen,

S_B is the value of "S" corresponding to a "defect free" specimen,

W is the "W" parameter for a given specimen,

W_B is the value of "W" corresponding to a "defect free" specimen.

While such a parameter is very useful, because of its ability to distinguish between multiple defect types, it still does not solve the problem completely due to some inherent theoretical limitations. The main restriction is that the analysis is valid if only one type of trapping center is present, or if one defect type is essentially dominant (Mantl and Trifthauser 1978). In

practice this means the experimenter has the ability to calculate defect type and concentration provided each sample has only one predominant type of positron trap. The difficulties arise if a sample contains two defect types, say vacancies and dislocation cores, in roughly equal concentrations.

In terms of the present experiments on high purity large grain size aluminum, because care has been taken to produce samples with only a single dominant defect type, one would expect the "R" parameter analysis to yield useful results. A family of R-type parameters can be calculated for the experiments in this work by examining ratios of the form

$$R_N = |((\Delta x(i)/\Delta x(j)))| \quad (4.7)$$

where R_N is an R-type parameter

$\Delta x(i)$ is the difference between $x(i)$ for the current sample and the value of $x(i)$ in a defect free sample

and i is less than j

In the original work of Mantl and Trifthauser (1978) the energy windows selected to define "S" and "W" were chosen so that the annihilation events contributing to the "S" parameter corresponded to conduction (valence) electrons while core electron events resulted in contributions to the "W" parameter. This relationship restricts the possible values of i and j as defined in Equation (4.7) above.

The specific "R" parameter used in this study is defined as

$$R_1 = \left| \frac{\Delta x(1)}{\Delta(x(10) + x(11) + x(12))} \right| \quad (4.8)$$

and is defined such that the energy windows are fairly close to those used by Mantl and Trifthauser (1978). For comparison, R_1 has a low energy window of ~511 - 511.32 KeV and a high energy window of ~513.88 - 514.84 KeV compared to windows of ~511 - 511.5 KeV and ~513.6 - 516.1 KeV in the referenced work.

Figure 16 is a plot of R_1 as a function of quenching temperature for the background corrected raw data. Note that although samples with primarily dislocation type defects have, in general, a higher R_1 value than the samples with primarily vacancy type defects, there is a significant amount of scatter in the data. The source of this scatter is not known exactly but it is probably related to the fact that the data was collected without temperature or digital stabilization. In fact, it is plausible that the spread in R_1 values is a numerical amplification of the spread in values of $x(1)$, $x(10)$, $x(11)$ and $x(12)$. In addition to this error source, any error associated with changes in the instrument resolution function, (IRF), should also be present in Figure 16. To test the utility of deconvolution in R-parameter analysis one would like to have a data set in which the second error source is present but the first error source, related to electronic drift, is negligible. Unfortunately, such a data set can not be obtained with the instrumentation used in this study.

In an attempt to isolate the instrument resolution effects the following procedure was employed. Using the fact that all DBPAS measurements for a given metallurgical sample were performed in a comparatively short time interval (~8 hrs.), it seems reasonable to assume that the spread in calculated lineshape values is a result of the lack of temperature and digital stabilization rather than of changes in instrument resolution. This hypothesis is supported by the observation that for a given set of consecutive experiments, the IRF's measured before and after the experiments showed only very slight changes. If this assumption is true, one may be able to artificially select a subset of the original data which qualitatively corresponds to a series of experiments with reduced electronic drift error. In this work each group of DBPAS measurements, corresponding to a sample subjected to

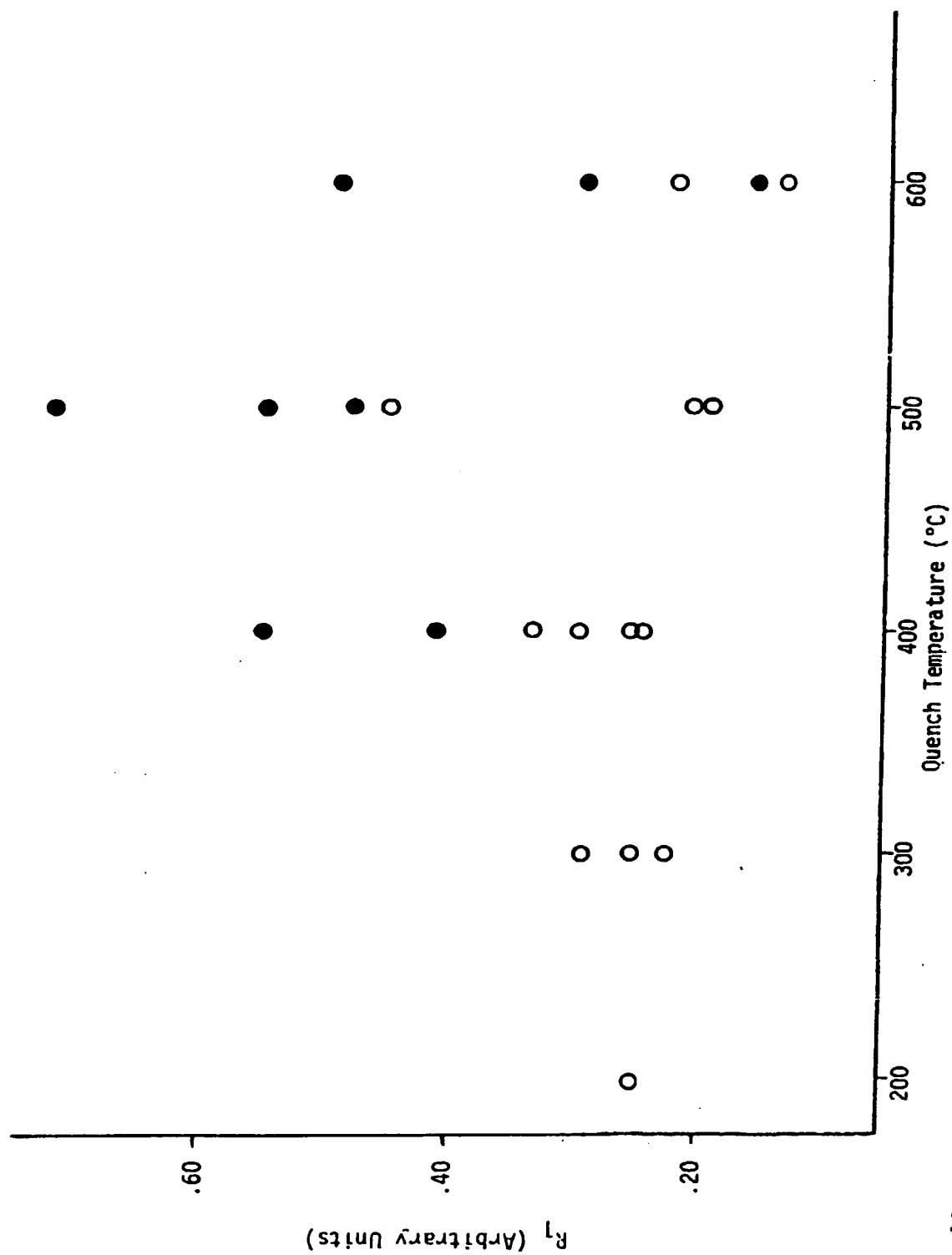


Figure 16. A Plot of R_1 Values for the Raw Data vs. Quench Temperature for Dislocations (●) and Vacancies (○).

a given thermal treatment, was independently examined and an average value for each relevant lineshape parameter was calculated. The corresponding R_1 values calculated from the average lineshape parameter values are shown in Figure 17. These values are, as in Figure 16, for the background corrected raw data.

A similar procedure was then employed for the deconvoluted data. That is, average $x(i)$ values were calculated for each specimen and then used to calculate R_1 values. These R_1 values for the deconvoluted data are shown in Figure 18. It is quite apparent that the spread in R-parameter values has been increased by the FFT/PS deconvolution algorithm. The explanation for the increased scatter in the data is not immediately obvious. In a previous section of this work it was demonstrated that deconvolution improved the quality of the calculated $x(1)$ lineshape parameter values. That is, the spread in $x(1)$ values for DBPAS measurements performed on a given sample was decreased (refer to Table 1). One could argue that decreasing the scatter of $x(1)$ for a given sample should improve, or at least not adversely affect, the amount of scatter in the calculated R_1 values. The difficulty is, of course, that R_1 depends not only on $x(1)$ but also on the values of the parameters $x(10)$, $x(11)$, and $x(12)$. These parameters are defined in the tail regions of the energy distribution and it is in this region that one must look to understand the difficulty associated with the calculation of R-type parameters for FFT/PS deconvoluted data.

Figures 19 and 20 are a comparison of the energy distribution (raw data) for a sample quenched from 600°C and then subsequently annealed at 523°K. Figure 19 shows the differences in the peak region of the spectra. Recall that $x(1)$ is defined over the energy window of 511 - 511.32 KeV. In Figure 20 the vertical scale has been expanded so that the differences in the tail region are visible. Several important features of the energy

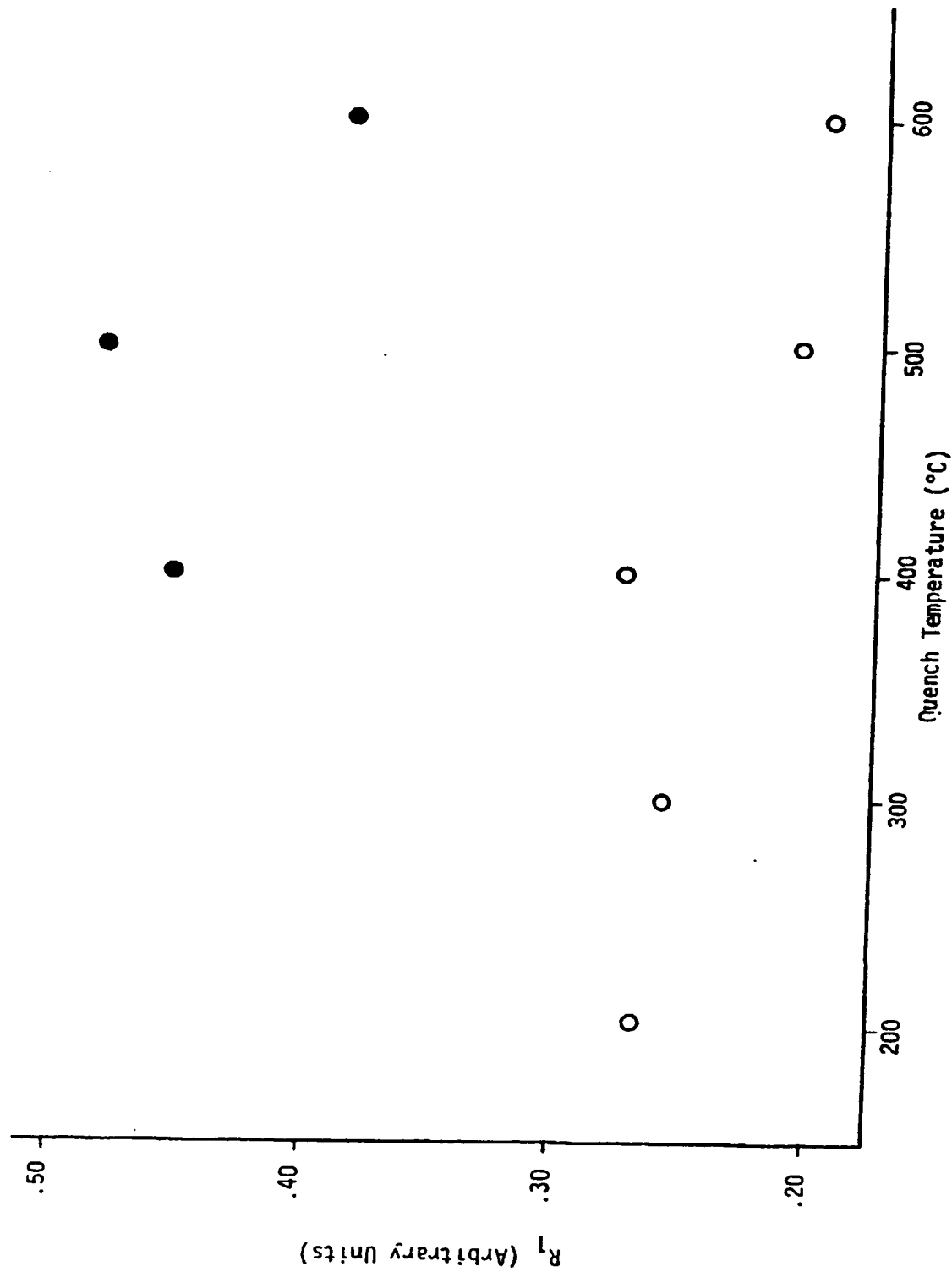


Figure 17. A Plot of R_1 Values as Calculated from Average Lineshape Parameter Values of the Raw Data vs. Quench Temperature for Dislocations (●) and Vacancies (○).

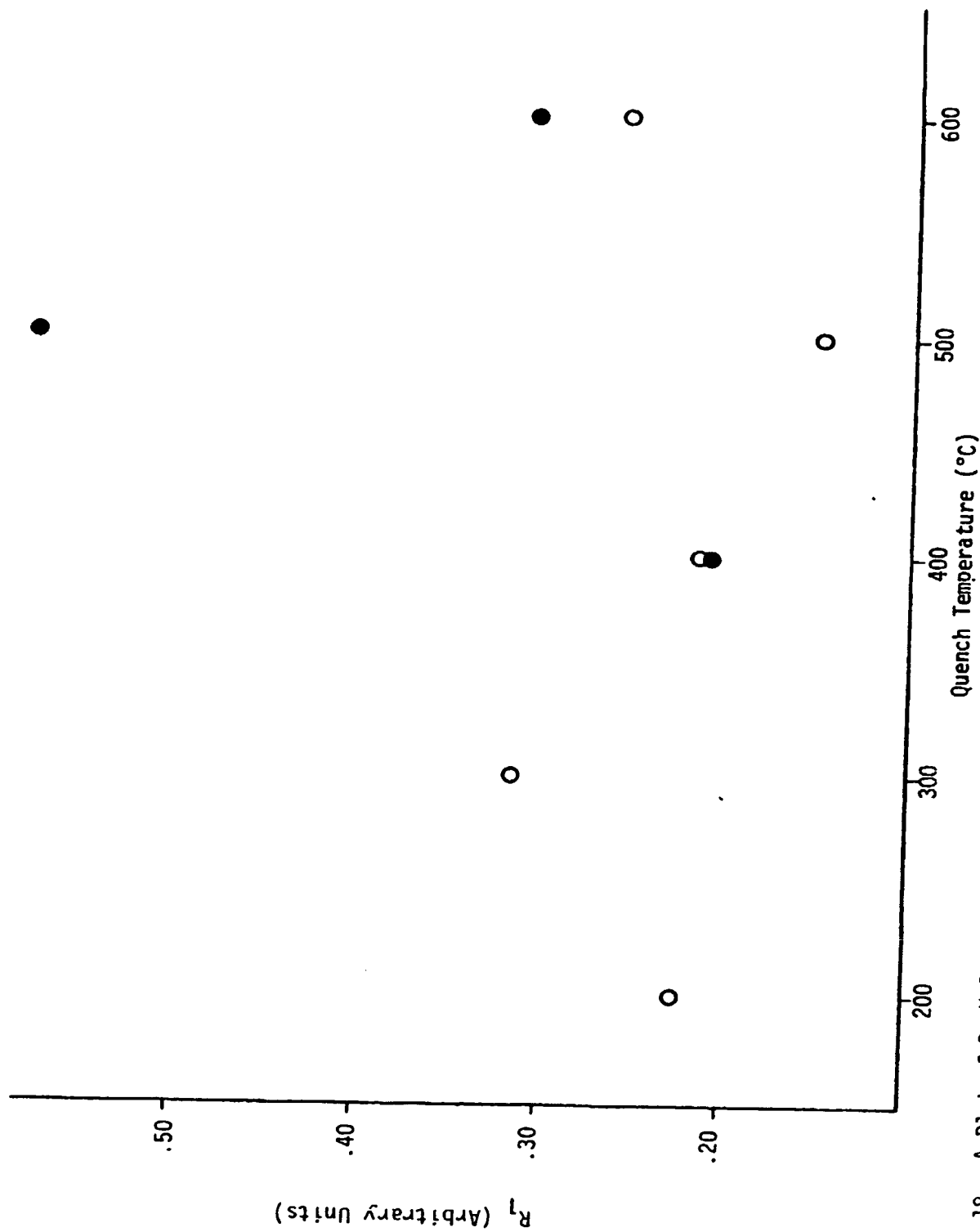


Figure 18. A Plot of R_1 Values for the Deconvoluted Data, Using all Retained Coefficients, vs. Quench Temperature.

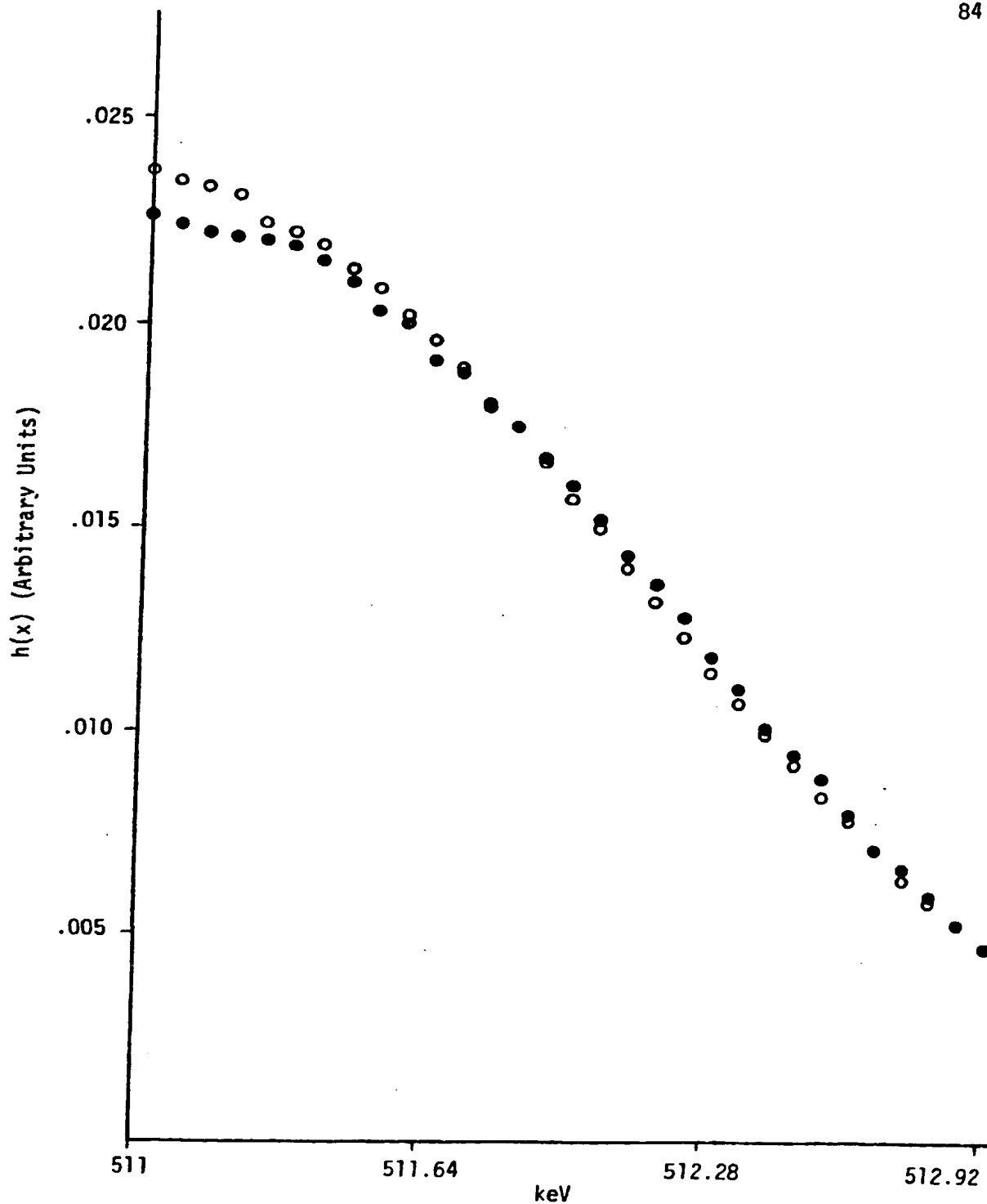


Figure 19. A Comparison of the Raw Data for an Aluminum Sample Quenched from 600°C (o) and the Same Sample After the High-Temperature Anneal (•).

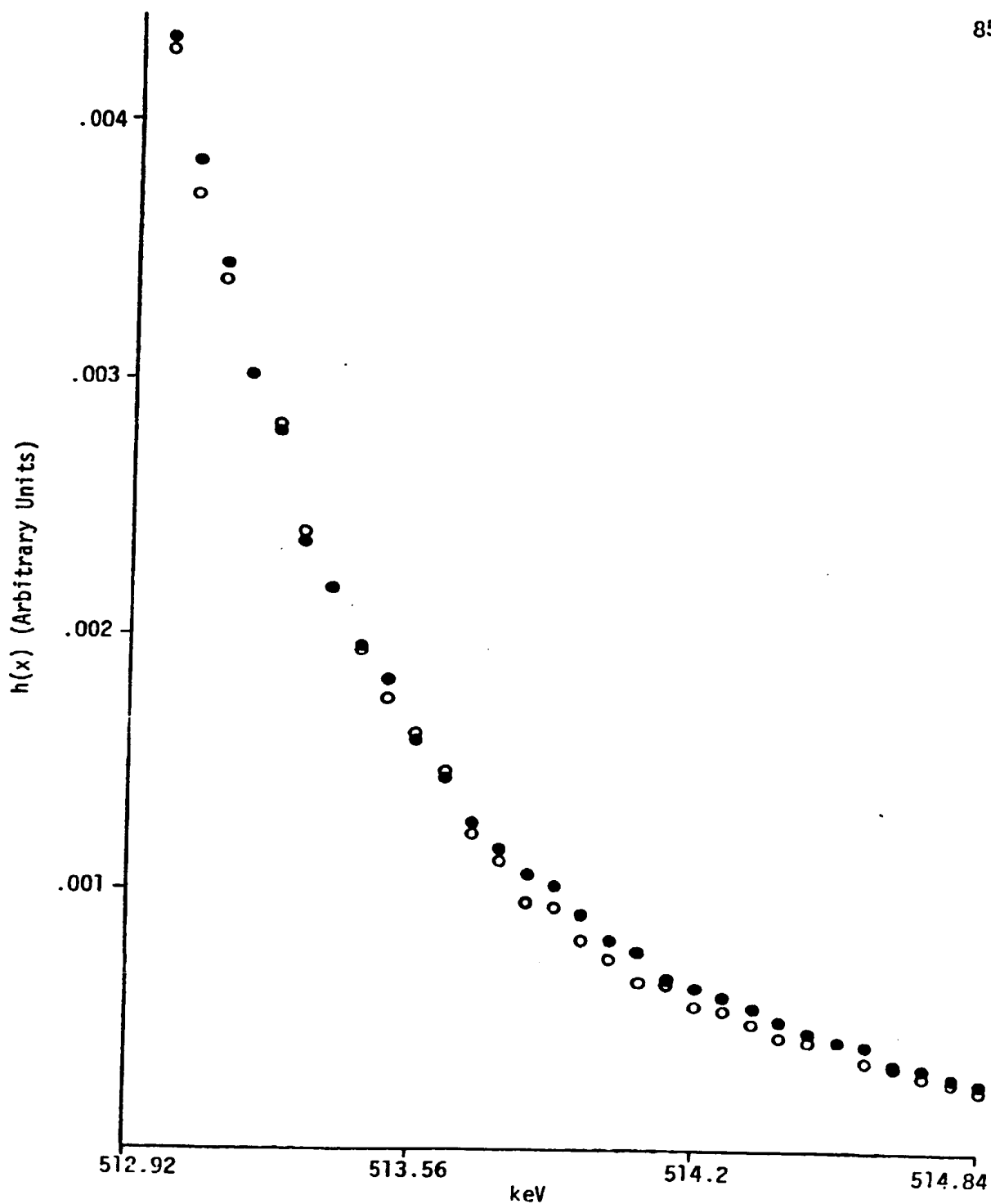


Figure 20. A Comparison of the Tail Region of the Raw Data for an Aluminum Sample Quenched from 600°C (o) and the Same Sample After the High Temperature Anneal (●).

distribution in the tail region are apparent. First, it must be noted that in general the data points for the quenched sample lie below their counterparts for the annealed sample as predicted by theory. Secondly, the statistical, or counting, error from channel to channel can be recognized. The former observation is believed to account for the qualitative agreement between theoretical predictions and the calculated R_1 values for the raw data. The latter observation, statistical noise, is the most probable explanation (along with electronic noise) for the spread in R_1 values as shown in Figure 16.

For comparison, Figures 21 and 22 show the change in energy distribution for the same two samples after deconvolution using the FFT/PS algorithm. In Figure 21, which shows the peak region, some of the desirable features of deconvolution are evident. Most notably, the statistical channel to channel noise has been removed (compare with Figure 19). A careful comparison of the raw and deconvoluted data shows that deconvolution does indeed decrease the full width half maximum as discussed previously.

Figure 22 shows, with an expanded vertical scale, an undesirable feature of the FFT/PS deconvolution method. It was mentioned in Chapter III that truncating the Fourier coefficients is equivalent to the insertion of a low pass filter and it is well known that low pass filtering introduces certain errors. Recalling that the Fourier analysis of the convolution equation, neglecting the statistical counting error, yields the following equation for the desired function $f(x)$:

$$f(x) = \int_{-\infty}^{+\infty} u(w)F(w)e^{-iwx}dw \quad (4.10)$$

where $u(w) = 1$ for $w < w_c$
 $= 0$ for $w > w_c$

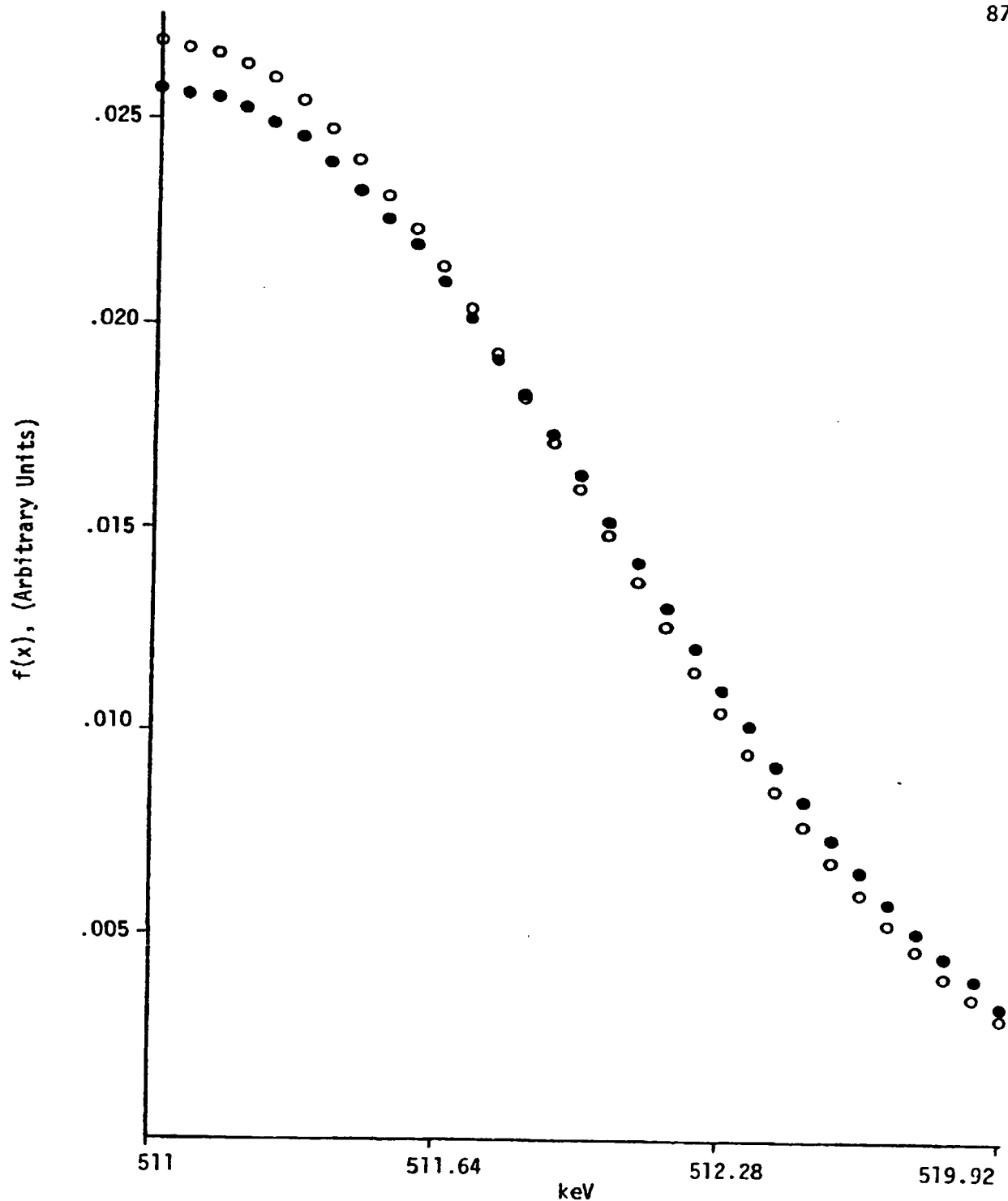


Figure 21. A Comparison of the Deconvoluted Data for an Aluminum Sample Quenched from -600°C (o) and the Same Sample After the High Temperature Anneal (●).

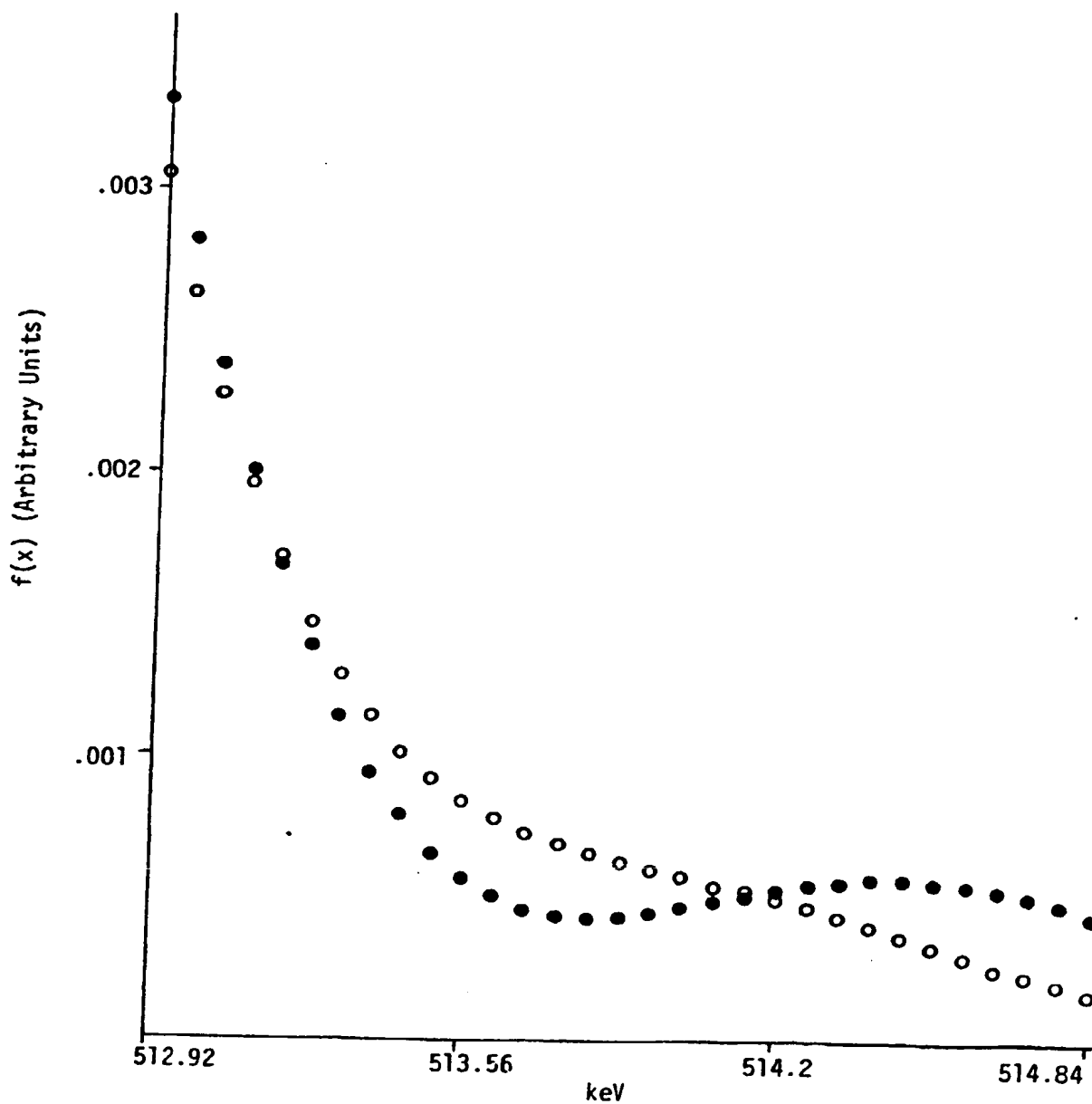


Figure 22. A Comparison of the Tail Region of the Deconvoluted Data for an Aluminum Sample Quenched from 600°C (o) and the Same Sample After the High Temperature Anneal (●).

and w_c corresponds to the frequency which is the first minimum of the power spectrum of $h(x)$

It can be shown (Bendat and Piersol 1971) that error introduced by such a filter is proportional to $(1/w_c)\sin(2\pi x w_c)$. The significance of this result is that the amplitude of the error is inversely proportional to w_c (the number of retained coefficients), and the frequency of the resulting error is proportional to w_c .

This effect is clearly evident in Figure 22. The open circles represent the annealed sample for which the power spectrum analysis yielded a w_c of fifty six (56) coefficients. For comparison, the filled circles, corresponding to the quenched specimen are calculated using sixty seven (67) retained coefficients. It is quite obvious that the error amplitude is decreased for the sample with the larger number of retained coefficients. A careful analysis of the data shows that the frequency of the error is proportional to w_c .

With this information, it is now possible to explain the increased scatter in R_1 values displayed by the FFT/PS deconvoluted data. Because the energy window used to define the wing parameter (513.88 - 514.84 KeV) is in the range where the amplitude of the filtering error is of the same order of magnitude as the amplitude of the true signal, this error source is significant. If the wavelength of the error source was small compared to the size of the energy window, then the error contribution would average to nearly zero and this difficulty would not exist. The problem arises because the energy window spans less than a period of the sinusoidal error source and it spans a different fraction of the period depending on the number of retained Fourier coefficients. For example, in Figure 22 the energy window of interest for the annealed sample spans approximately the positive half cycle of the

sinusoidal filtering error. This leads to a calculated wing parameter with an artificially high value, which in turn distorts the value of the calculated R_1 parameter. Since multiple DBPAS measurements on even the same metallurgical sample may yield slightly different numbers of retained coefficients, this error source can lead to a scatter of R_1 parameters for a single sample. Because the number of retained coefficients varies more widely between samples of differing defect density (or defect structure), the spread in R_1 values becomes larger for such samples.

Having related the scatter in R_1 values for the deconvoluted data to the phase and amplitude of the filtering error, it is now possible to try to correct for this error source. There are at least three ways to proceed. First, one could simply extend the experimental collection times to get a higher number of total integrated counts in the energy spectrum. This would result in better counting statistics, and a higher number of retained coefficients (Schaffer *et al.* 1984). Since an increased number of retained coefficients decreases the amplitude of the filtering error, such a procedure should yield better R_1 values. Unfortunately one must pay a very high price in terms of collection time to significantly increase w_c .

Another approach is to use the same number of retained coefficients for each data set. That is, one could calculate a w_c value for each data set to be analyzed and then deconvolute all of the data sets using the minimum value of w_c . Using this procedure will not eliminate the error source, but it will be controlled so that its contribution to the calculated values of R_1 does not vary between experiments. Clearly such an approach has several inherent disadvantages. The primary disadvantage is that the absolute values of R_1 will be a function of the particular value of w_c used in the deconvolution procedure. One would prefer an approach which eliminates, or at least

greatly reduces, the filtering error rather than simply controlling it. A method for accomplishing this goal will be discussed in the final chapter of this work. What follows here is a discussion of controlling the error source in the tail region by using the same number of retained coefficients for each data set.

Figure 23 shows the energy window used to calculate the wing parameter. The vertical scale has been greatly expanded to show the fine detail of the structure. This plot is for the same samples as in Figure 22, but in this case both data sets have been deconvoluted using fifty seven (57) coefficients. As expected, the filtering error is in phase. In addition, as theory predicts, the data points corresponding to the quenched sample are below the points representing the annealed sample. One can extend this procedure to all of the other data sets and then calculate the corresponding R_1 parameters in the manner previously described. The results are presented in Figure 24. When this figure is compared with Figure 18 it can be seen that the filtering error does influence the scatter in R_1 values. By simply controlling this error source, i.e. by using the same number of retained coefficients in the deconvolution of all data sets, the quality of the calculated R_1 values can be improved.

To summarize this section, the average values of R_1 , along with the associated standard deviations for each of the two defect types, have been calculated for four different types of data. The four data types are: 1) the entire raw data set (Fig. 16), 2) the average raw data (Fig. 17), 3) the averages of the deconvoluted data as obtained directly from the FFT/PS algorithm (Fig. 18), and 4) the averages of the deconvoluted data using the same number of retained coefficients for each data set (Fig. 24). These values are shown in Table II.

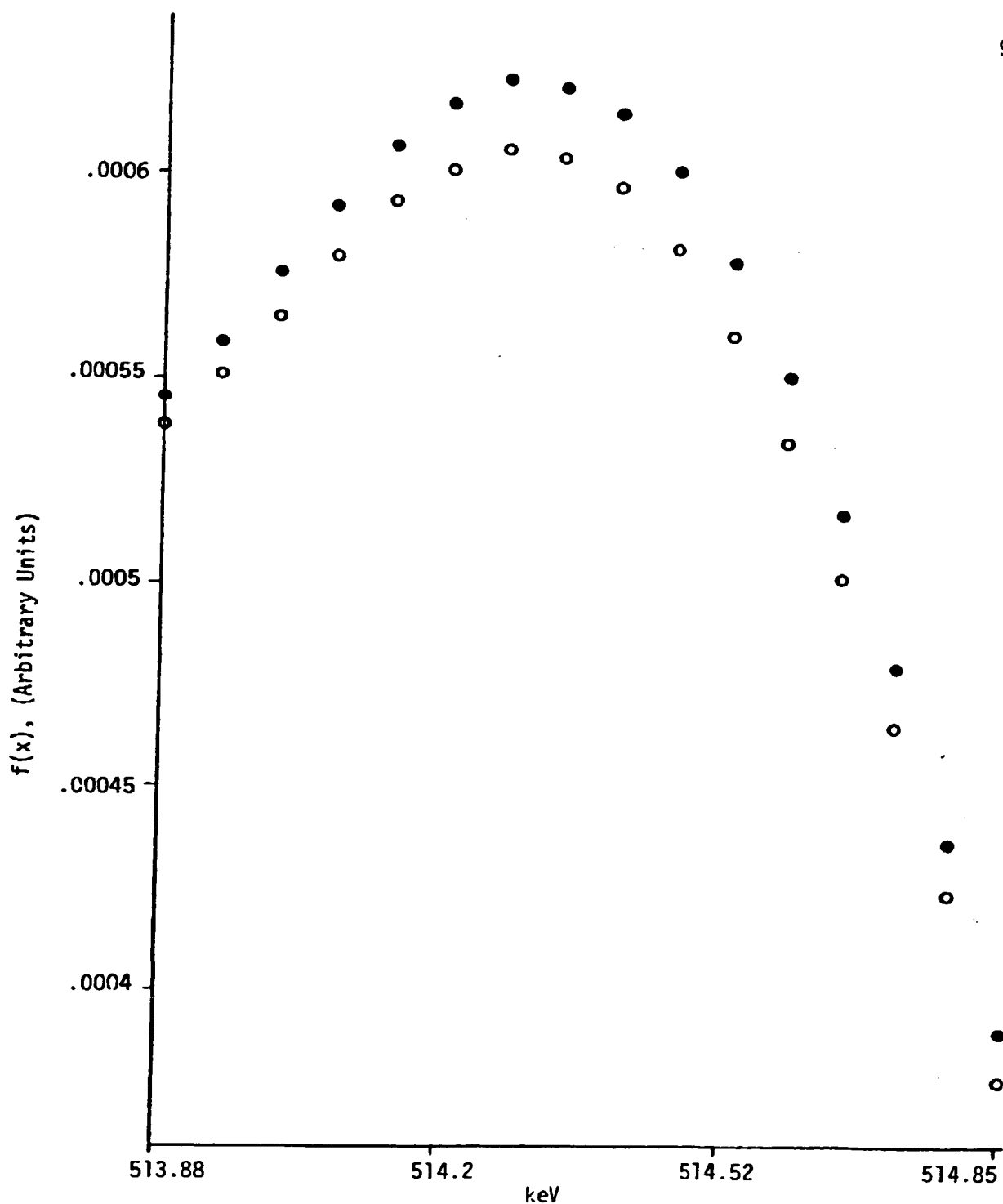


Figure 23. A Comparison of the Tail Region of the Same Samples as in Figure 22. In this Plot Both Data Sets have Been Deconvoluted Using the Same Number (57) of Reconstruction Coefficients.

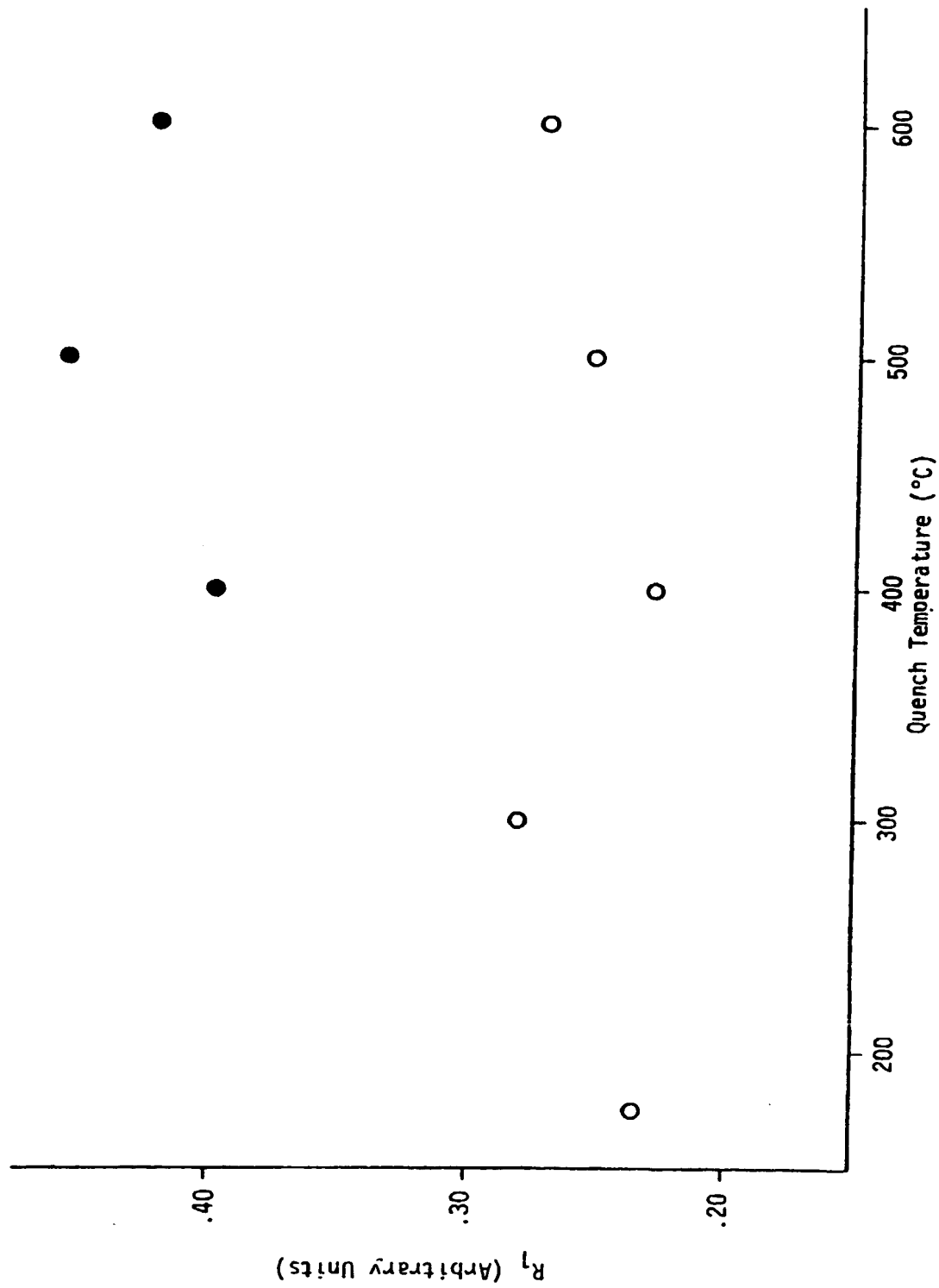


Figure 24. A Plot of R_1 Values, for the Deconvoluted Data Using a Constant Number of Reconstruction Coefficients, Comparing Dislocations (●) with Vacancies (○).

Table II

Data Type	$R_{avg}(Vac.)$	$R_{avg}(Dis.)$	$\sigma(Vac.)$	$\sigma(Dis.)$
1	.261	.458	.0677	.1751
2	.240	.440	.0347	.0492
3	.234	.364	.1515	.1876
4	.253	.424	.0216	.0290

Note that the largest standard deviations occur for the deconvoluted data when the maximum number of coefficients are used in the reconstruction of each $f(x)$. This result is explainable in view of the previously discussed relationship between w_c and the amplitude and phase of the filtering error. When this error source is controlled by using a single value of w_c for the deconvolution of all data sets (data type 4) the calculated standard deviations are improved. With this modification to the FFT/PS deconvolution algorithm it appears that if one defect type dominates, one can distinguish between vacancies and prismatic dislocation loops, in high purity large grain size aluminum.

To conclude the results and discussion chapter of this work the even central moments of the annihilation energy distributions will be discussed. As mentioned in the introduction, because this technique has the potential to distinguish between multiple defect types, this family of lineshape parameters is interesting from a theoretical point of view. Briefly, this possibility arises because the higher order central moments are increasingly dominated by the tail regions of the energy distribution. Thus, the low moments give information about the central region (S-type information) while the higher order moments yield W-type information. Unfortunately, this analysis is extremely sensitive to small errors in the tail regions which are greatly

amplified by moment analysis. Therefore the statistical error ruled out moment analysis in the raw data while filtering error precluded its use in the deconvoluted data. It is possible, however, that an improved filtering technique, discussed in the following chapter, will allow moment analysis to become a useful tool in future work.

CHAPTER V

CONCLUSIONS AND FUTURE WORK

Over the past several decades positron annihilation spectroscopy has evolved into an accepted tool for the study of the defect structure of materials. Of the three most common measurement techniques Doppler broadening offers the advantages of reasonably high data collection rates, comparatively low source strength requirements, and few geometrical experimental constraints. It is therefore the technique with the best chance of making the transition from a laboratory research device to an industrial NDT tool. Unfortunately, DBPAS measurements suffer from some inherent limitations. The two most significant limitations are comparatively poor instrumental energy resolution and limited ability to distinguish between multiple defect types. Based on these observations, the two primary goals of this work were: 1) to develop an efficient, model independent, noniterative deconvolution method, and 2) to improve the ability of DBPAS to distinguish between multiple defect types.

In order to improve the effective energy resolution of the DBPAS instrumentation the fast Fourier transform/power spectrum analysis deconvolution algorithm was developed (Schaffer et al. 1984). The convolution integral equation was shown in Chapter III to describe the relationship between the experimentally observed energy distribution, the instrument resolution function,

data is that results obtained in different laboratories should be more directly comparable if the instrumental broadening effects have been accurately removed. This ability to directly compare numerical values for standard lineshape parameters should help to clear up some of the discrepancies which currently exist in the literature.

While it is fairly clear that accurate deconvolution should correct for changes in the IRF and improve the agreement of results obtained using different instrumentation, some of the other trends observed from the comparison of lineshape parameter calculated before and after deconvolution were not entirely predictable. For example, based on the limited results presented in this work, both the sensitivity and the accuracy of the lineshape parameters are improved by deconvolution. One explanation for the improved accuracy, i.e. the decrease in the error ratio, of the deconvoluted lineshape parameters is that the filtering operation has essentially removed the statistical counting errors present in the raw data. A comparison of multiple DBPAS measurements performed on the same sample show that before deconvolution, differences in the statistical counting error in the peak region can lead to a spread in calculated $x(1)$ values. However, after deconvolution, the energy distributions show less variation from experiment to experiments, and hence yield $x(1)$ values with correspondingly less scatter.

The increased sensitivity of the deconvoluted parameters may be related to the removal of the "broadening" action of the experimental instrumentation. Recall that the major effect of the instrumentation is to spread counts from one channel into several adjacent channels. Therefore, the true lineshape changes in the annihilation energy distribution, which are caused by the trapping of positrons at defects, are spread out over a much larger number of channels in the raw data. The deconvolution procedure corrects for

this effect and, in so doing, restores some of the details of the "true" annihilation energy distribution. This results in an increase in observed defect sensitivity.

Even with the improvements in lineshape sensitivity and accuracy due to the FFT/PS algorithm, the DBPAS technique must have the additional ability to distinguish between multiple defect types if it is to become a useful tool in the study of industrial materials. In order to investigate the usefulness of deconvolution in resolving multiple defect types, a comparison was made between the values of the R_1 parameters calculated before and after deconvolution. If the number of reconstruction Fourier coefficients is allowed to vary between samples, as would be the case if the FFT/PS method is used in its standard form, then the calculated R_1 parameter value yields little useful information.

In order to explain this somewhat negative result, the consequences of truncating the Fourier coefficient, also known as low pass filtering, were examined in greater detail. It is known that the truncation of the coefficients introduces a filtering error with an amplitude inversely proportional to the number of retained coefficients, w_c , and a frequency which is proportional to w_c . Ideally, one would like to greatly increase the number of retained coefficients in order to reduce the amplitude of this filtering error. Unfortunately, as w_c is increased beyond the first minimum of the power spectrum the calculated solution will contain large, rapidly oscillating components which are not physically plausible. The mathematics of this argument were presented in detail in Chapter III.

Since it is not possible to reduce the amplitude of the filtering error by arbitrarily increasing w_c an alternative method was developed to improve the calculated values of R_1 for deconvoluted data. The first step in

the procedure is to calculate a w_c value for each of the data sets to be analyzed. Next the minimum value of w_c is selected and subsequently employed in the deconvolution of all the data sets. Using this procedure does not eliminate the filtering error, but rather controls the source such that its contribution to the calculated R_1 values remains approximately constant from experiment to experiment. Although this solution is not ideal, the data presented in Chapter IV clearly indicate that by controlling the error source the reproducibility of the R_1 parameter, and its usefulness in the separation of multiple defect types, is improved.

To summarize this section it can be stated that the FFT/PS deconvolution algorithm appears to improve the quality of the data as obtained from DBPAS measurements in several ways. These improvements, as presented in this work include: 1) automatic correction for accidental and/or intentional changes in the instrument resolution function, 2) the potential of direct comparison of quantitative results between laboratories, 3) an improvement in both lineshape sensitivity and accuracy, and 4) the ability to distinguish between vacancy and dislocation type defects, as demonstrated for large grained high purity aluminum.

To generalize these conclusions, further studies of this kind should be performed using a variety of different alloys with known defect type and concentration. In addition, it would be extremely useful to repeat the entire series of experiments using a DBPAS system which is both digitally and temperature stabilized. Such a data set would allow one to separate the effects of instrument broadening, which are theoretically correctable by deconvolution, from the nonsystematic effects of instrumental drift. In addition, spectra collected on a stabilized system could conceivably possess better counting statistics (due to longer allowable experimental times) which could in turn

increase the number of coefficients retained in the deconvolution procedure.

Additional experiments should be performed on the FFT/PS algorithm. These experiments could be designed to investigate alternative filtering schemes with the hope of reducing the associated filtering error. Most notably, the use of cosine tapering appears to be a viable approach. Once the filtering error has been reduced or eliminated the utility of moment analysis in the separation of multiple defect types should be reinvestigated. It is not known at this time if the current FFT/PS algorithm is capable of distinguishing the formation of positronium in a nonmetallic material. Positronium would show itself as a relatively high frequency characteristic of the annihilation energy distribution. The key factor is determining whether the frequencies required to observe positronium are to the left of the first minimum in the power spectrum. This question could be investigated using both numerically simulated data and data obtained from materials in which positronium is known to form.

In order for Doppler broadened positron annihilation spectroscopy to become a widely used industrial NDT tool it must continue to evolve in several ways. Its energy resolution must improve, the ability to separate multiple defect types must be further developed, and the reproducibility and reliability of the experimental results must increase. Although the fast Fourier transform/power spectrum analysis deconvolution technique has clearly not solved all of these problems, the results presented in this work indicate that this method measurably improves the quality and reproducibility of the information obtainable from DBPAS measurements, and serves as a sound basis for future refinements.

APPENDICES

APPENDIX A

In this appendix the equations used to theoretically determine the stopping, or thermalization, times of positrons in metals will be discussed. For a more complete treatment of this subject see Brandt and Arista (1982). As briefly mentioned in the text, positrons slow down mainly by two mechanisms: 1) ionization and excitation of electrons which is characterized by the electronic stopping power, S_e , of the material, and 2) phonon interactions characterized by the phonon stopping power, S_{ph} . The second mechanism dominates at epithermal energies below some critical value E_c characteristic of the material. In the range from the maximum source energy, E_s , to E_c the electronic stopping power dominates. This energy range can be further divided into two subranges separated by the photon energy for which the material has its maximum stopping power, E_m . In the range $E_m < E < E_s$ an accurate estimate for the stopping times is given by

$$t_1 = 7.7\rho^{-1}(E_i/mc^2)^{1.2} \quad (A.1)$$

where t_1 is the stopping time in psec

ρ is the density of the material in g/cm^3

mc^2 is 0.511 MeV

and E_i is the initial positron energy

since

$$E_i/mc^2 < E_s/mc^2 \sim 1 \quad (A.2)$$

we can rewrite Eq. (A.1) as

$$t_1 \sim 7.7\rho^{-1}$$

(A.3)

which for most metals of interest results in stopping times of ~ 1 psec for the high energy region.

For $E_c < E < E_m$ the electron gas theory of conduction electrons with Fermi energy E_F is used to produce the equation

$$S_e = \frac{\pi}{105} \frac{m^2}{h} \left[\frac{2}{m}\right]^{3/2} \frac{E^{5/2}}{E_F} \quad (A.4)$$

in the case of a continuous slow down approximation

$$t_s = - \left[\frac{m}{2}\right]^{1/2} \int_{E_i}^{E_f} \frac{dE}{E^{1/2} S} \quad (A.5)$$

Substituting Eq. (A.4) into Eq. (A.5) and integrating yields

$$t_2 = \frac{105}{8\pi} \frac{hE_F}{E_f^2} \quad (A.6)$$

where t_2 is in picoseconds.

In the low energy region $3/2 KT < E < E_c$ phonon interactions dominate with

$$S_{PH} = \frac{2}{\pi} \frac{m^3 w^2}{h^4 d} E \quad (A.7)$$

where w is the lattice deformation potential.

Eq. (A.4) can be combined with Eq. (A.7) to define E_c yielding

$$E_c^{3/2} = \frac{105b^2}{2^{1/2}\pi^2} \frac{m^{5/2} E_F^3}{h^3 \rho} \quad (A.8)$$

Inserting Eq. (A.7) into Eq. (A.5) and integrating from $3/2 KT$ to E_c as defined by Eq. (A.8) yields

$$t_3 = \frac{\pi h^4 \rho}{3^{1/2} w^2 (K_B T)^{1/2}} \left[1 - \left(\frac{3K_B T}{2E_c} \right)^{1/2} \right] \quad (A.9)$$

using typical values for common metals it can be shown that

$$t_3 > t_2 > t_1 \quad (\text{A.10})$$

Thus, phonon thermalization times are larger than electronic stopping times.

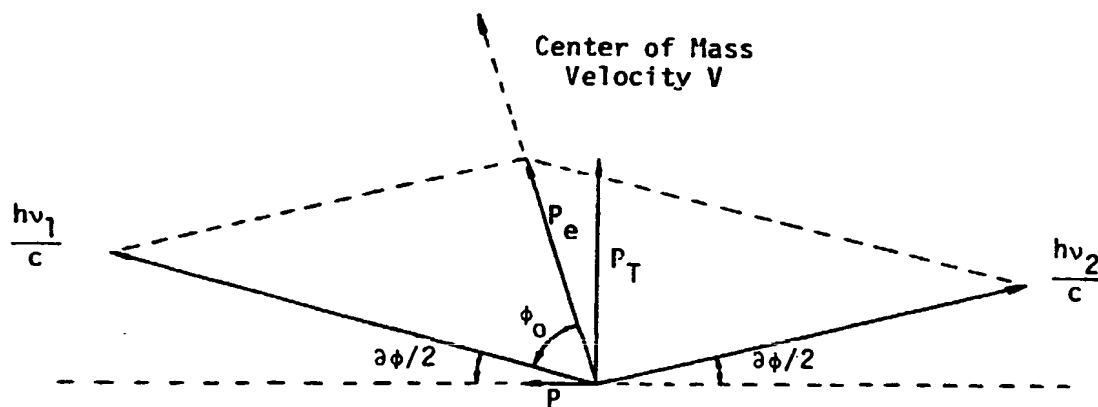
The total stopping time is given by

$$t_s = t_1 + t_2 + t_3 \quad (\text{A.11})$$

with typical theoretical values of 13 psec in Al and 45 psec in Pb (Brandt and Arista 1982).

APPENDIX B

The purpose of this appendix is to describe the relationships between the momentum distribution of the electrons in the sample and the measured Doppler shifts in energy as well as the angular deviations from colinearity of the γ -rays. In the center of mass rest reference frame the annihilation γ -rays will be emitted in directions separated by 180° and each with an energy of 511 KeV which is equal to the rest mass of an electron (or positron). However, in the laboratory frame the momentum of the electron (the positron is assumed to be at rest as described in the text) produces changes in both the observed γ -ray energy and the angle between the γ -rays. The geometry of the situation is shown in the diagram below.



Straightforward application of the Lorentz transformations of special relativity combined with some trigonometric manipulation yield the result that

$$\delta\phi = \left(\frac{2v}{c}\right) \sin \phi_0 + \theta \left(\frac{v^2}{c^2}\right) \quad (B.1)$$

where $\delta\phi$ is the angular deviation from 180°

v is the electron velocity

c is the speed of light

ϕ_0 is the angle between the electron velocity vector and the direction of γ -ray emission

and $\theta(\frac{v^2}{c^2})$ is a term of order $\frac{v^2}{c^2}$ which is negligible for $v \ll c$

(For a detailed derivation of this result see Rindler 1960). The relativistic definition of momentum is

$$p = \alpha m_0 v \quad (B.2)$$

where p is the momentum

$$\alpha = (1 - \frac{v^2}{c^2})^{-1/2}$$

and m_0 is the particle mass

For $v \ll c$, $\alpha \rightarrow 1$ and $p = mv$

Substituting this result into Eq. (B.1) yields

$$\delta\phi = \frac{2p}{m_0 c} \sin \phi_0 \quad (B.3)$$

Defining the transverse momentum component as

$$p_T = p \sin \phi_0 \quad (B.4)$$

and substituting Eq. (B.4) into Eq. (B.3) yields the final result

$$\delta\phi = \frac{2p_T}{m_0 c} \quad (B.5)$$

demonstrates that measuring the distribution of the angular deviations, $\delta\phi$, is in essence equivalent to measuring the distribution of the momentum of the electrons within the sample.

In the case of Doppler measurements one has

$$\delta p_\gamma = p_e \cos \phi_0 \quad (B.6)$$

where δp_γ is the change in momentum of the γ -ray

p_e is the electron momentum

and ϕ_0 is as defined above

Using Eq. (B.2) with $v \ll c$ Eq. (B.6) takes the form

$$\delta p_\gamma = m_e v_e \cos \phi_0 \quad (B.7)$$

It can be shown that in relativistic dynamics

$$E^2 = p^2 c^2 + m_0^2 c^4 \quad (B.8)$$

where E is the relativistic energy

p is the relativistic momentum

c is the speed of light

and m_0 is the particle rest mass

Now for a photon (γ -ray) $m_0 = 0$ so Eq. (B.8) reduces to

$$E_\gamma = p_\gamma c \quad (B.9)$$

Combining Eqs. (B.6), (B.7), and (B.9) yields

$$\delta E_\gamma = \delta p_\gamma c = p_e (\cos \phi_0) c = m_e c v_e (\cos \phi_0) \quad (B.10)$$

where δE_γ is the Doppler energy shift of the observed γ -ray

δp_γ is the change in momentum of the γ -ray

and p_e is the momentum of the annihilating electron

From Eq. (B.10) it can be seen that the momentum distribution of the annihilating electrons can be deduced from the measured Doppler energy shifts.

Combining Eq. (B.5) with (B.10) yields the following relationship between $\delta\phi$ and δE :

$$\delta E = 255.5 \delta\phi \quad (B.11)$$

where δE is in eV

and $\delta\phi$ is in mrad

Finally, by combining Eq. (B.10) and the fact that for an electron $m_0 c^2 = 511$

KeV it can be shown that

$$\delta E_{\gamma} = 511(\cos \phi_0)\left(\frac{v_e}{c}\right) \quad (\text{B.12})$$

where δE_{γ} is in KeV

For the case of a 1 eV electron ($v_e = 5.93 \times 10^7$ cm/sec) moving in the direction of γ -ray emission, Eq. B.12 predicts a 1.01 KeV shift in observed energy.

APPENDIX C

The material examined in this work was high purity (99.9995%) aluminum supplied by the Materials Research Corporation. The chemical analysis, in terms of PPM of metallic interstitials (and some gases) is listed below.

<u>Element</u>	<u>PPM</u>	<u>Element</u>	<u>PPM</u>	<u>Element</u>	<u>PPM</u>
Ag	<0.1	Li	<0.1	U	
Al	major	Mg	1.5	V	<0.1
As	<0.1	Mn	<0.1	W	<0.2
Au	<0.1	Mo	<0.1	Y	
B		Na	0.2	Zn	0.4
Ba		Nb	<0.1	Zr	<0.1
Be		Ni	0.1		
Bi	<0.1	Pb	<0.1	Cl	0.6
Ca	<0.1	Pd	<0.1	F	
Cd	<0.1	Pt	<0.14	H	3
Co	<0.1	Rh	<0.1	N	5
Cr	<0.1	Sb	<0.1	O	20
Cu	0.1	Si	0.9	P	0.3
Fc	<0.1	Sn	<0.3	S	
Ga	<0.1	Ta			
Ge	<0.1	Th			
In	<0.1	Ti	<0.1		
K	<0.1	Tl			

APPENDIX D

In this Appendix the utility of Fourier analysis in the solution of the convolution integral equation will be demonstrated. In the first section of Chapter III it was shown that

$$h(y) = \int_{-\infty}^{\infty} f(x)r(y-x)dx \quad (D.1)$$

By definition of the Fourier transform

$$F(w) = \int_{-\infty}^{\infty} e^{iwx}f(x)dx \quad (D.2)$$

Therefore

$$F(w)R(w) = \left[\int_{-\infty}^{\infty} e^{iwx}f(x)dx \right] \left[\int_{-\infty}^{\infty} e^{iwt}r(t)dt \right] \quad (D.3)$$

$$= \int_{-\infty}^{\infty} \int_{-\infty}^{\infty} e^{iwx}f(x)e^{iwt}r(t)dxdt \quad (D.4)$$

$$= \int_{-\infty}^{\infty} \int_{-\infty}^{\infty} e^{iw(x+t)}f(x)r(t)dxdt \quad (D.5)$$

Now let $x + t = y$

so $t = y - x$

and $dt = dy$

Hence Eq. (D.5) can be rewritten as

$$F(w)R(w) = \int_{-\infty}^{\infty} \int_{-\infty}^{\infty} e^{iwy}f(x)r(y-x)dx dy \quad (D.6)$$

$$= \int_{-\infty}^{\infty} e^{iwy} \left[\int_{-\infty}^{\infty} f(x)r(y-x)dx \right] dy \quad (D.7)$$

But the integral within the brackets is by Eq. (D.1) equal to $h(y)$. Therefore Eq. (D.7) can be rewritten as

$$F(w)R(w) = \int_{-\infty}^{\infty} e^{iwy}h(y)dy \quad (D.8)$$

and using Eq. (D.2) on the right hand side

$$F(w)R(w) = H(w) \quad (D.9)$$

This demonstrates that in Fourier space convolution is simply a complex multiplication.

APPENDIX E

The purpose of this Appendix is to demonstrate some of the mathematical difficulties associated with the incorrectly posed convolution integral equation. The primary source of the problem is that the left hand side of the equation

$$h^*(x) = \int_a^b f(y)r(x-y)dy \quad (E.1)$$

is only known to within some error ϵ . That is, if $h(x)$ is the "true" function then

$$\max_{a < x < b} |h^*(x) - h(x)| < \epsilon \quad (E.2)$$

Any function $f_1(y)$ which when convoluted with the known resolution function $r(x)$ yields a function $h_1^*(x)$ that satisfies Eq. (E.2) must be considered a solution of Eq. (E.1).

Assume there are two solutions to Eq. (E.1) which are $f_1(x)$ and $f_2(x) = f_1(x) + c \sin(2\pi nw/(b-a))$. By definition

$$h_1^*(x) = \int_a^b f_1(y)r(x-y)dy \quad (E.3)$$

and

$$h_2^*(x) = \int_a^b [f_1(y) + C \sin (2\pi ny/(b-a))]r(x-y)dy \quad (E.4)$$

Subtracting Eq. (E.3) from Eq. (E.4) yields

$$h_2^*(x) - h_1^*(x) = \int_a^b r(x-y) C \sin(2\pi ny/(b-a)) dy \quad (E.5)$$

Now integrating by parts with

$$\begin{aligned} u &= r(x-y) & dv &= C \sin\left(\frac{2\pi Ny}{b-a}\right) dy \\ du &= \frac{d(r(x-y))}{dy} dy & v &= -\frac{C(b-a)}{2\pi N} \cos\left(\frac{2\pi Ny}{b-a}\right) \end{aligned}$$

yields

$$\begin{aligned} \int_a^b r(x-y) C \sin\left(\frac{2\pi Ny}{b-a}\right) dy &= r(x-y) \left[-\frac{C(b-a)}{2\pi N} \cos\left(\frac{2\pi Ny}{b-a}\right) \right]_a^b \\ &\quad - \int_a^b \frac{C(b-a)}{2\pi N} \cos\left(\frac{2\pi Ny}{b-a}\right) \frac{d(r(x-y))}{dy} dy \end{aligned} \quad (E.6)$$

Now integrating the last term on the right hand side by parts with

$$\begin{aligned} u &= \cos\left(\frac{2\pi Ny}{b-a}\right) & dv &= \frac{d(r(x-y))}{dy} dy \\ du &= -\left(\frac{2\pi Ny}{b-a}\right) \sin\left(\frac{2\pi Ny}{b-a}\right) dy & v &= r(x-y) \end{aligned}$$

Yields

$$\begin{aligned} \int_a^b \cos\left(\frac{2\pi Ny}{b-a}\right) \frac{d(r(x-y))}{dy} dy &= [r(x-y) \cos\left(\frac{2\pi Ny}{b-a}\right)]_a^b \\ &\quad - \int_a^b r(x-y) \left(\frac{2\pi Ny}{b-a}\right) \sin\left(\frac{2\pi Ny}{b-a}\right) dy \end{aligned} \quad (E.7)$$

Combining Eqs. (E.6) and (E.7) yields

$$\int_a^b f(x-y) C \sin\left(\frac{2\pi Ny}{b-a}\right) dx = \frac{-C(b-a)}{2\pi N} [r(x-y) \cos\left(\frac{2\pi Ny}{b-a}\right)]_a^b \quad (E.8)$$

and combining Eqs. (E.8) and (E.5) yields the result

$$h_2^*(x) - h_1^*(x) = \frac{C}{N} \left[\left(\frac{a-b}{2\pi} \right) r(x-y) \cos\left(\frac{2\pi Ny}{b-a}\right) \right]_a^b \quad (E.9)$$

So it can be seen that for any value of C one can select a value of N large

enough so that the difference between $h_2^*(x)$ and $h_1^*(x)$ is smaller than any previously determined number. Therefore, both $h_1^*(x)$ and $h_2^*(x)$ satisfy Eq. (E.2) and $f_1(x)$ as well as $f_2(x)$ must be solutions to Eq. (E.1). The important point is that one may select C and N in such a way as to allow $f_1(x)$ and $f_2(x)$ to differ from each other by as much as one likes. Clearly the problem as posed does not have a unique solution and a different solution technique is required.

APPENDIX F

```

CCCCCCCCCCCCCCCCCCCCCCCCCCCCCCCCCCCCCCCCCCCCCCCCCCCCCCCCCCCC
C
C   THIS IS A LISTING OF THE FORTRAN 77 VERSION OF THE PROGRAM C
C   DECONPFT WHICH IS DESIGNED TO DECONVOLUTE DOPPLER BROADENED C
C   POSITRON ANNIHILATION SPECTRA. FOR A DESCRIPTION OF THE C
C   MATHEMATICS INVOLVED SEE J.P. SCHAFER, E.J. SHAUGHNESSY, C
C   AND P.L. JONES, JOURNAL OF NUCLEAR INSTRUMENTS AND METHODS C
C   IN PHYSICS RESEARCH, B5, 74, 1984. C
C
CCCCCCCCCCCCCCCCCCCCCCCCCCCCCCCCCCCCCCCCCCCCCCCCCCCCCCCCCCCC

```

```

      INTEGER PCSP
      CHARACTER*2 PCSZ,PCH
      CHARACTER*80 XCH,YCH,TCH
      CHARACTER*7 NAME,NAMEE
      DIMENSION IA(2048), IB(2048), DOPE(12),XP(74),YP(74)
      DOUBLE PRECISION A(2048),B(2048),C(2048),FR(2048),HC(2048)
      DOUBLE PRECISION D(2048),E(2048),G(2),S(2048),SI(2048)
      DOUBLE PRECISION F1(2048),PI,V,W,W1
      COMPLEX*16 R(4096),H(4096),F(4096),T,A1,H1(4096)
      COMPLEX*16 A2,R1(4096),T1
      PI=3.141592653589793D0
      PRINT*,'THIS PROGRAM DEALS WITH THE CONVOLUTION'
      PRINT*,'H(X)=F(X)*R(X), WHERE R IS THE'
      PRINT*,'RESOLUTION FUNCTION, H IS THE'
      PRINT*,'BROADENED AND OBSERVED FUNCTION, AND'
      PRINT*,'F IS THE TRUE AND DESIRED FUNCTION.'
      PRINT*,' '
C   THE RESOLUTION FUNCTION IS USUALLY OBTAINED FROM
C   THE Sr(85) GAMMA RAY (514 KeV).
C
      2 PRINT*,'THE PROGRAM REQUIRES N DATA POINTS'
      PRINT*,'WHERE N=2**M, AND M IS AN INTEGER.'
      PRINT*,' '
C   THESE DATA POINTS WILL BE H(X) AND R(X) AS COLLECTED
C   BY THE MCA.
C
      PRINT*,'ENTER THE VALUE OF M TO BE USED IN THIS'
      PRINT*,'PROGRAM. (M=11 YIELDS N=2048)'
      PRINT*,' '
      READ(*,'(I2)') M
      N=2**M
      ND2=N/2
      ND4=N/4
      PRINT*,'ENTER THE RESOLUTION FUNCTION FILENAME'
      PRINT*,' '
      READ (*,'(A7)') NAME
      OPEN (90,FILE=NAME,PAD='YES')
      READ (90,1) (IA(I), I=1,2048)
1  FORMAT(5X,5I7)
      CLOSE (90)

```

```

PRINT*, 'ENTER THE EXPERIMENTAL FUNCTION FILENAME'
PRINT*, '
READ (*, '(A7)') NAME
OPEN (90, FILE=NAME, PAD='YES')
READ (90, 1) (IB(I), I=1, 2048)
CLOSE (90)
NIN=2048
C THE SUBROUTINE DELSKIP DELETES THE LINE
C SKIP IN THE RAW DATA SUPPLIED BY THE MCA.
  CALL DELSKIP (IA, A, NIN)
  CALL DELSKIP (IB, B, NIN)
C THE FOLLOWING SUBROUTINE CALCULATES THE CENTRAL
C CHANNEL LOCATION BASED ON THE CENTER OF THE
C 11 CHANNEL REGION WHICH CONTAINS THE MAXIMUM
C TOTAL NUMBER OF COUNTS
  CALL CENTER (A, IMAXA)
  CALL CENTER (B, IMAXB)
C
C THIS NEXT LARGE SECTION DEALS WITH THE
C BACKGROUND CORRECTION.
C
  PRINT*, 'DO YOU WISH TO BACKGROUND CORRECT? '
  READ (*, '(A1)') NAME
  IF (NAME .EQ. 'Y') GO TO 3
  CALL NOBACK (N, B, IMAXB)
  GO TO 200
3 PRINT*, 'DO YOU WISH TO BACKGROUND CORRECT USING'
  PRINT*, 'THE JACKMAN METHOD OR THE SPECTRAL FILTERING'
  PRINT*, 'TECHNIQUE? (J OR S) '
  READ (*, '(A1)') NAME
  IF (NAME .EQ. 'J') GO TO 5
  PRINT*, 'THE NEXT SEVERAL QUESTIONS REFER TO THE'
  PRINT*, 'RESOLUTION FUNCTION. '
  CALL BACK (A, IMAXA, N)
  PRINT*, 'THE NEXT SEVERAL QUESTIONS REFER TO THE'
  PRINT*, 'EXPERIMENTAL FUNCTION.'
  CALL BACK (B, IMAXB, N)
  GO TO 377
5 PRINT*, 'ENTER THE RESOLUTION OF THE MCA IN'
  PRINT*, 'eV/CHANNEL. (USE A DECIMAL POINT)'
  PRINT*, '(SUGGESTION: IF THE SYSTEM IS SET'
  PRINT*, 'IN ITS NORMAL MODE USE 64. )'
  PRINT*, '
  READ (*, '(P6.2)') EV
  X=(1000.D0/EV)+0.5D0
  IK=IFIX (X)
  IKLA=(IMAXA-20)/IK
  ILA=514-IKLA
  IKHA=(1024-IMAXA)/IK
  IHA=514+IKHA
  IKLB=(IMAXB-20)/IK

```

```

CALL FIT (N1,D,E,G)
BAH=G(1)
XMAH=G(2)
PRINT*, 'TO WHICH ENERGIES WOULD YOU LIKE TO'
PRINT*, 'EXTRAPOLATE THE LINEAR BACKGROUND'
PRINT*, 'CORRECTION? (SUGGESTION: 506 521)'
PRINT*, '
READ (*,*) IL,IH
PRINT*, 'ON THE HIGH ENERGY SIDE OF THE PEAK,'
PRINT*, 'WHAT IS THE HIGHEST ENERGY YOU WISH'
PRINT*, 'TO HAVE CONSIDERED FOR DECONVOLUTION?'
PRINT*, 'SUGGESTION: 521'
PRINT*, '
READ (*,*) IEND
IL=IMAXA-(514-IL)*IK
IH=IMAXA+(IH-514)*IK
IEND=IMAXA+(IEND-514)*IK
IEA=IEND
DO 55 I=IH,IEND
  A(I)=A(I)-(XMAH*I+BBH)
  IF (A(I) .LT. 0.) A(I)=0.D0
55 CONTINUE
XH=XMAH*IH+BAH
XL=XMAL*IL+BAL
XM=(XL-XH)/(FLOAT(IL-IH))
XB=XH-((XL-XH)/(FLOAT(IL-IH)))*IH
DO 60 I=IMAXA,IH
  A(I)=A(I)-(XM*I+XB)
  IF (A(I) .LT. 0.) A(I)=0.D0
60 CONTINUE
GO TO 378
377 CONTINUE
IEA=IMAXA+109
IEB=IMAXB+453
378 CONTINUE
C
C THIS IS THE END OF THE BACKGROUND CORRECTION SEQUENCE.
C NEXT WE NEED TO REFLECT THE HIGH ENERGY HALF OF THE
C BACKGROUND CORRECTED PEAK ABOUT THE CENTRAL POINT
C TO FORM A SYMMETRIC PEAK. IN ADDITION A ZEROFILL
C TO 2048 DATA POINTS IS REQUIRED
C
CALL ZEROFILL (A,IMAXA,IEA,N)
CALL ZEROFILL (B,IMAXB,IEB,N)
M1=IEA-IMAXA+10
CALL TAPER (A,M1,N)
M2=IEB-IMAXB+20
CALL TAPER (B,M2,N)
M3=M1
CALL SMOOTH (A,M3,N)
M4=M2

```

```

      CALL SMOOTH (B,M4,N)
C   THE NEXT TWO DO LOOPS NORMALIZE THE AREA
C   OF THE RESOLUTION AND BROADENED SPECTRA.
      V=0.D0
      W=0.D0
      DO 62 I=1,N
        V=V+A(I)
        W=W+B(I)
62   CONTINUE
      DO 63 I=1,N
        A(I)=A(I)/V
        B(I)=B(I)/W
63   CONTINUE
      DO 68 I=1,N
        S(I)=B(I)
68   CONTINUE
      DO 72 I=1,ND2
        J=ND2+I
        V=S(I)
        S(I)=S(J)
        S(J)=V
72   CONTINUE
      PRINT*,'DO YOU WISH TO SAVE THE BACKGROUND'
      PRINT*,'CORRECTED SPECTRUM? '
      READ (*,'(A1)') NAME
      IF (NAME .EQ. 'N') GO TO 76
      PRINT*,'ENTER THE FILENAME. '
      READ (*,'(A7)') NAME
      OPEN (90,FILE=NAME,PAD='YES')
      WRITE (90,74) (S(I),I=1,N)
74   FORMAT (5X,5D22.10)
      CLOSE (90)
      CALL PARAMS (N,S)
76   CONTINUE
      DO 77 I=1,N
        R(I)=DCMPLX(A(I),0.D0)
        H(I)=DCMPLX(B(I),0.D0)
77   CONTINUE
      CALL REORDER (M,H)
      CALL FFT (M,H)
      CALL REORDER (M,R)
      CALL FFT (M,R)
      CALL DECON (M,F,R,H)
C
      DOPE(1)=150.
      DOPE(2)=150.
      DOPE(3)=950.
      DOPE(4)=650.
      DOPE(5)=0.
      DOPE(6)=0.
      PCSZ='NS'

```

```

      PCSP=1
C
C THIS NEXT SMALL SECTION ALLOWS ONE TO VIEW THE POWER
C SPECTRUM IF SO DESIRED.
      PRINT*, 'WOULD YOU LIKE TO SEE AND PLOT THE POWER SPECTRUM'
      PRINT*, 'OF THE EXPERIMENTAL DATA AND THE DECONVOLUTED DATA.'
      PRINT*, ' '
      READ (*, '(A1)') NAME
      IF (NAME.EQ. 'N') GO TO 179
      DO 78 I=1,ND2
        D(I)=H(I)*(CONJG(H(I)))
78 CONTINUE
      PRINT*, 'ENTER THE FILENAME FOR THE P.S. OF THE EX. DATA. '
      PRINT*, ' '
      READ (*, '(A7)') NAME
      OPEN (90, FILE=NAME, PAD='YES')
      WRITE (90, 901) (I, D(I), I=1, ND2)
901 FORMAT (5(I4, D22.12))
      CLOSE (90)
      CALL REORDER (M, F)
      CALL FFT (M, F)
      T=0.D0
      DO 277 I=1, N
        T=T+F(I)
277 CONTINUE
      DO 278 I=1, N
        F(I)=F(I)/T
278 CONTINUE
      CALL REORDER (M, F)
      CALL FFT (M, F)
      DO 178 I=1, ND2
        E(I)=F(I)*(CONJG(F(I)))
178 CONTINUE
      PRINT*, 'ENTER THE FILENAME FOR THE P.S. OF THE DECON. DATA.'
      PRINT*, ' '
      READ (*, '(A7)') NAME
      OPEN (90, FILE=NAME, PAD='YES')
      WRITE (90, 901) (I, E(I), I=1, ND2)
      CLOSE (90)
      NPTS=74
      DO 910 I=1, 10
        XP(I)=ALOG10(FLOAT(I))
        YP(I)=E(I)
        YP(I)=ALOG10(YP(I))
910 CONTINUE
      DO 912 I=15, 100, 5
        J=8+(I/5)
        XP(J)=ALOG10(FLOAT(I))
        YP(J)=E(I)
        YP(J)=ALOG10(YP(J))
912 CONTINUE

```



```

DO 914 I=120,1000,20
  J=23+(I/20)
  XP(J)=ALOG10(FLOAT(I))
  YP(J)=E(I)
  YP(J)=ALOG10(YP(J))
914 CONTINUE
  XP(74)=ALOG10(1020.)
  YP(74)=-10.
  XCH='LOG OF THE FOURIER COEFFICIENT NO.'
  MX=34
  YCH='LOG OF THE POWER'
  MY=16
  PRINT*, 'ENTER THE TITLE OF THIS PLOT. '
  PRINT*, ' '
  READ (*, '(A80)') TCH
  PRINT*, 'ENTER THE NO. OF CHARACTERS IN THE TITLE. '
  READ (*, '(I2)') NT
  PCH='1 '
  CALL CKSTUP ('TK15',9600)
  CALL CKER
  CALL CKGRAP (DOPE,NPTS,XP,YP,XCH,MX,YCH,MY,TCH,NT,PCSZ
C,PCSP,PCH)
  DO 930 I=1,10
    YP(I)=D(I)
    YP(I)=ALOG10(YP(I))
930 CONTINUE
  DO 932 I=15,100,5
    J=8+(I/5)
    YP(J)=D(I)
    YP(J)=ALOG10(YP(J))
932 CONTINUE
  DO 934 I=120,1020,20
    J=23+(I/20)
    YP(J)=D(I)
    YP(J)=ALOG10(YP(J))
934 CONTINUE
  PCH='3 '
  CALL CKPLT (DOPE,NPTS,XP,YP,PCSZ,PCSP,PCH)
  CALL CKMA (0.,0.,1)
  READ (*,*)
179 CONTINUE
C
C AT THIS STAGE THE RESOLUTION AND EXPERIMENTAL
C SPECTRA HAVE BEEN TRANSFORMED INTO FOURIER SPACE.
C THIS NEXT SMALL SECTION DETERMINES THE NUMBER OF
C POSITIVE DECREASING FOURIER COEFFICIENTS IN THE
C DECONVOLUTED RESULT. THIS INFORMATION CAN THEN
C BE USED IN THE FILTERING ROUTINES IF SO DESIRED.
C
DO 80 I=2,N
  J=I-1

```

```

      D(I)=REAL(F(I))
      D(J)=REAL(F(J))
      IF (D(I) .LT. 0.0) GO TO 81
      IF (D(I) .GT. D(J)) GO TO 81
80  CONTINUE
81  IPD=I-1
      WRITE (*,82) IPD
82  FORMAT (5X,'THE NO. OF POSITIVE DECREASING COEPS. IS ' I5)
      PRINT*, '
      PRINT*, 'DO YOU WISH TO USE A COSINE TAPER FILTER'
      PRINT*, 'TO MODIFY THE FOURIER COEFFICIENTS? '
      READ (*, '(A1)') NAME
      IF (NAME .EQ. 'N') GO TO 189
      PRINT*, 'ENTER THE NUMBER OF THE FIRST COEFFICIENT'
      PRINT*, 'TO BE SET EQUAL TO ZERO. '
      READ (*, '(I3)') IZ
      PRINT*, 'ENTER THE NUMBER OF COEFFICIENTS TO BE TAPERED. '
      READ (*, '(I3)') IT
      IS=IZ-IT
      XS=REAL(IS)
      XZ=REAL(IZ)
      XY=1.0/(XS-XZ)
      DO 181 I=IS, IZ
          X=REAL(I)
          F(I)=F(I)*0.5*(1-COS(PI*XY*(X-XZ)))
181  CONTINUE
      J=IZ+1
      K=(N/2)+1
      DO 183 I=J, K
          F(I)=DCMPLX (0.D0,0.D0)
183  CONTINUE
      K=K-1
      DO 185 I=2, K
          J=N+2-I
          F(J)=F(I)
185  CONTINUE
189  PRINT*, 'DO YOU WISH TO USE A BOXCAR FILTER TO'
      PRINT*, 'MODIFY THE FOURIER COEFFICIENTS IN'
      PRINT*, 'ORDER TO REMOVE THE HIGH FREQ. NOISE? '
      READ (*, '(A1)') NAME
      IF (NAME .EQ. 'N') GO TO 84
      PRINT*, 'ENTER THE NUMBER OF COEFFICIENTS TO BE USED: '
      READ (*, *) J
      J=J+1
      K=N+2-J
      DO 83 I=J, K
          F(I)=DCMPLX(0.D0,0.D0)
83  CONTINUE
84  CONTINUE
      PRINT*, 'DO YOU WANT TO SEE THE FOURIER COEFFICIENTS?'
      READ (*, '(A1)') NAME

```

```

      IF (NAME .EQ. 'N') GO TO 85
      PRINT*, 'ENTER THE FILENAME FOR H(X). '
      PRINT*, ' '
      READ (*, '(A7)') NAME
      OPEN (90, FILE=NAME, PAD='YES')
      WRITE (90, 911) (I, H(I), I=1, N)
911  FORMAT (2(I4, 2D22.10))
      CLOSE (90)
      OPEN (90, FILE='PCSF', PAD='YES')
      WRITE (90, 911) (I, F(I), I=1, N)
      CLOSE (90)
85  CONTINUE
      CALL REORDER (M, F)
      CALL FFT (M, F)
      CALL REORDER (M, H)
      CALL FFT (M, H)
C   THIS NEXT SECTION ALLOWS ONE TO USE THE ITERATION
C   ROUTINE TO IMPROVE F(X).
      PRINT*, 'WOULD YOU LIKE TO USE THE ITERATION'
      PRINT*, 'SUBROUTINE TO TRY TO IMPROVE THE'
      PRINT*, 'ACCURACY OF THE DECONVOLUTED SPECTRUM? '
      READ (*, '(A1)') NAME
      IF (NAME .EQ. 'N') GO TO 86
      CALL ITER (M, R, F, H)
86  CONTINUE
C   THIS NEXT DO LOOP SHIFTS THE PHASE OF THE
C   EXPERIMENTAL FUNCTION H, AND THE DECONVOLUTED
C   FUNCTION F, SO THAT THEIR MAXIMA ARE LOCATED
C   IN THE CENTRAL CHANNELS.
      ND2=N/2
      DO 88 I=1, ND2
          J=ND2+I
          T=F(I)
          T1=H(I)
          F(I)=F(J)
          H(I)=H(J)
          F(J)=T
          H(J)=T1
88  CONTINUE
      DO 98 I=1, N
          F1(I)=REAL(F(I))
98  CONTINUE
      W=0.D0
      DO 99 I=1, N
          W=W+F1(I)
99  CONTINUE
      DO 100 I=1, N
          F1(I)=F1(I)/W
100 CONTINUE
      PRINT*, 'DO YOU WANT A PLOT OF h(X) AND f(X)? '
      READ (*, '(A1)') NAME

```

```

      IF (NAME .EQ. 'N') GO TO 105
      NPTS=60
      W=F1(1025)
      DO 102 I=1,60
        J=1024+I
        XP(I)=.064*(FLOAT(I))
        YP(I)=F1(J)/W
102  CONTINUE
      XCH='KeV'
      MX=3
      YCH='h(X) AND f(X)'
      MY=13
      PRINT*, 'ENTER THE TITLE OF THIS PLOT.'
      PRINT*, ' '
      READ (*, '(A80)') TCH
      PRINT*, 'ENTER THE NO. OF CHARACTERS IN THE TITLE. '
      READ (*, '(I2)') NT
      PCH='1 '
      CALL CKSTUP ('TK15',9600)
      CALL CKER
      CALL CKGRAP (DOPE,NPTS,XP,YP,XCH,MX,YCH,MY,TCH,NT,PCSZ
C,PCSP,PCH)
      DO 103 I=1,60
        J=1024+I
        YP(I)=S(J)/W
103  CONTINUE
      PCH='3 '
      CALL CKPLT (DOPE,NPTS,XP,YP,PCSZ,PCSP,PCH)
      CALL CKMA (0.,0.,1)
      READ (*,*)
105  PRINT*, 'DO YOU WISH TO SAVE THE '
      PRINT*, 'DECONVOLUTED SPECTRUM? '
      READ (*, '(A1)') NAME
      IF (NAME .EQ. 'N') GO TO 101
      PRINT*, 'ENTER THE FILENAME. '
      READ (*, '(A7)') NAME
      OPEN (90, FILE=NAME, PAD='YES')
      WRITE (90,74) (F1(I), I=1,N)
      CLOSE (90)
101  CONTINUE
      PRINT*, 'DO YOU WISH TO CHECK YOUR RESULT BY'
      PRINT*, 'CONVOLUTING f(X) WITH r(X) AND COMPARING'
      PRINT*, 'THE RESULT WITH h(X)?'
      READ (*, '(A1)') NAME
      IF (NAME .EQ. 'N') GO TO 200
      CALL REORDER (M,F)
      CALL FFT (M,F)
      CALL CONV (M,F,R,H1)
      CALL REORDER (M,H1)
      CALL FFT (M,H1)
      DO 106 I=1,N

```

```

      HC(I)=REAL(H1(I))
106 CONTINUE
      V=0.D0
      DO 107 I=1,N
        V=V+HC(I)
107 CONTINUE
      DO 108 I=1,N
        HC(I)=HC(I)/V
108 CONTINUE
      PRINT*, 'ENTER THE FILENAME FOR THE RESULT'
      PRINT*, 'OF THIS COMPARISON.'
      PRINT*, ' '
      READ (*, '(A7)') NAME
      OPEN (90, FILE=NAME, PAD='YES')
      WRITE (90, 110)
110 FORMAT (3X, 'I', 14X, 'h(X) RAW', 14X, 'h(X)=(F*R)', 14X, 'f(X)')
      WRITE (90, 120) (I, S(I), HC(I), F1(I), I=1025, 1300)
120 FORMAT (1X, I4, 2X, 3D22.10)
      CLOSE (90)
      PRINT*, 'DO YOU WANT A PLOT OF h(X) AND THE ESTIMATE'
      PRINT*, 'OF h(X) OBTAINED FROM f(X)*r(X)? '
      READ (*, '(A1)') NAME
      IF (NAME .EQ. 'N') GO TO 200
      NPTS=60
      W=HC(1025)
      DO 130 I=1, 60
        J=1024+I
        XP(I)=.064*(FLOAT(I))
        YP(I)=HC(J)/W
130 CONTINUE
      XCH='Rev'
      MX=3
      YCH='h(X) AND h` (X)'
      MY=14
      PRINT*, 'ENTER THE TITLE OF THIS PLOT.'
      PRINT*, ' '
      READ (*, '(A80)') TCH
      PRINT*, 'ENTER THE NO. OF CHARACTERS IN THE TITLE. '
      READ (*, '(I2)') NT
      PCH='1 '
      CALL CKSTUP ('TK15', 9600,
      CALL CKER
      CALL CKGRAF (DOPE, NPTS, XP, YP, XCH, MX, YCH, MY, TCH, NT, PCSZ
      C, PCSP, PCH)
      DO 140 I=1, 60
        J=1024+I
        YP(I)=S(J)/W
140 CONTINUE
      PCH='3 '
      CALL CKPLT (DOPE, NPTS, XP, YP, PCSZ, PCSP, PCH)
      CALL CKMA (0., 0., 1)

```

```

      READ (*,*)
200  CONTINUE
      CALL PARAMS (N,P1)
      STOP
      END
CCCCCCCCCCCCCCCCCCCCCCCCCCCCCCCCCCCCCCCCCCCCCCCCCCCCCCCCCCCC
C
      SUBROUTINE DELSKIP (IC,C,NIN)
      DIMENSION IC(2048)
      DOUBLE PRECISION C(1024)
      J=0
      K=0
      DO 10 I=1,NIN
        J=J+1
        K=K+1
        IC(I)=IC(K)
        IF (J .EQ. 5) THEN
          J=0
          K=K+5
        ENDIF
10    CONTINUE
      NID2=NIN/2
      DO 20 I=1,NID2
        C(I)=FLOAT(IC(I))
20    CONTINUE
      RETURN
      END
C
      SUBROUTINE CENTER (A,IMAX)
      DOUBLE PRECISION A(1024),X,T(21),Y
      X=0.D0
      DO 10 I=300,800
        IF (A(I) .GT. X) THEN
          X=A(I)
          J=I-10
        ENDIF
10    CONTINUE
      K=J+21
      Y=0.D0
      DO 20 I=J,K
        L=I-5
        M=I+5
        T(I)=0.D0
        DO 15 N=L,M
          T(I)=T(I)+A(N)
15    CONTINUE
        IF (T(I) .GT. Y) THEN
          Y=T(I)
          IMAX=I
        ENDIF
20    CONTINUE

```

```

RETURN
END

```

```

C
  SUBROUTINE FIT (N,X,Y,C)
C  THIS SUBROUTINE IS A SIMPLIFICATION OF
C  A LARGER SUBROUTINE WHICH FITS A CURVE USING
C  UP TO A NINTH ORDER POLYNOMIAL.  FOR A
C  REFERENCE SEE JPS DISSERTATION.
    DOUBLE PRECISION X(300),Y(300),C(2),A(3,3),XN(300)
    DO 10 I=1,N
10  XN(I)=1.D0
    DO 30 I=1,2
      A(I,1)=0.D0
      A(I,3)=0.D0
      DO 20 J=1,N
        A(I,1)=A(I,1)+XN(J)
        A(I,3)=A(I,3)+Y(J)*XN(J)
20  XN(J)=XN(J)*X(J)
30  CONTINUE
      A(2,2)=0.D0
      DO 40 J=1,N
        A(2,2)=A(2,2)+XN(J)
40  XN(J)=XN(J)*X(J)
      A(1,2)=A(2,1)
      DO 50 I=1,2
        SUM=0.D0
        IF (2 .GT. I) GO TO 45
        SUM=SUM+A(I,1)*A(1,2)
        A(I,2)=A(I,2)-SUM
        GO TO 50
45  IF (ABS(A(I,I)) .LT. 1.E-10) GO TO 99
        A(I,2)=(A(I,2)-SUM)/A(I,I)
50  CONTINUE
      DO 90 J=1,2
60  C(J)=A(J,3)
        C(1)=C(1)/A(1,1)
        SUM=A(2,1)*C(1)
        C(2)=(C(2)-SUM)/A(2,2)
        SUM=A(1,2)*C(2)
        C(1)=C(1)-SUM
      RETURN
99  PRINT*, 'TROUBLE IN SUBROUTINE FIT'
    RETURN
  END

```

```

C
  SUBROUTINE ZEROFILL (C,IM,IE,N)
    DOUBLE PRECISION C(2048),D(2048),T
    M=IE-IM
    MP1=M+1
    DO 10 I=1,N
      D(I)=0.D0

```

```

10 CONTINUE
   DO 20 I=1,MP1
      J=IM+I-1
      D(I)=C(J)
20 CONTINUE
   DO 30 I=1,N
      C(I)=D(I)
30 CONTINUE
   RETURN
   END

C
SUBROUTINE TAPER (C,M,N)
DOUBLE PRECISION C(2048),T
T=1.D0/1000.D0
DO 90 I=1,M
   IF (C(I) .NE. 0.D0) GO TO 80
   J=I-1
   K=I+1
   C(I)=(C(J)+C(K))/2.D0
   IF (C(I) .LT. T) GO TO 95
80 CONTINUE
90 CONTINUE
   GO TO 97
95 IK=I
   DO 96 J=IK,M
      K=J-1
      C(J)=0.95D0*C(K)
96 CONTINUE
97 CONTINUE
   ND2=N/2.D0
   DO 100 I=2,ND2
      J=ND2+I
      K=ND2+2-I
      C(J)=C(K)
100 CONTINUE
   RETURN
   END

C
SUBROUTINE SMOOTH (C,M,N)
DOUBLE PRECISION C(2048)
DO 20 I=2,M
   J=I-1
   IF (C(J) .GT. C(I)) GO TO 10
   K=I+1
   C(I)=(C(J)+C(K))/2.D0
5   IF (C(J) .GT. C(I)) GO TO 10
   C(I)=0.999*C(I)
   GO TO 5
10 CONTINUE
20 CONTINUE
   ND2=N/2

```



```

      DO 30 I=2,ND2
        J=ND2+I
        K=ND2+2-I
        C(J)=C(K)
30    CONTINUE
      RETURN
      END

C
      SUBROUTINE REORDER (M,C)
C    IN ORDER TO USE THE FOLLOWING FFT ONE MUST
C    FIRST REORDER THE DATA.  SEE JPS DISSERTATION
C    FOR DETAILS.
      COMPLEX*16 C(4096),T
      N=2**M
      MV2=N/2
      NM1=N-1
      J=1
      DO 7 I=1,NM1
        IF (I .GE. J) GO TO 5
        T=C(J)
        C(J)=C(I)
        C(I)=T
5      K=MV2
6      IF (K .GE. J) GO TO 7
        J=J-K
        K=K/2
        GO TO 6
7    J=J+K
      RETURN
      END

C
      SUBROUTINE FFT (M,A)
C    FOR DETAILS SEE JPS DISSERTATION
      DOUBLE PRECISION PI
      COMPLEX*16 A(4096),U,W,T
      PI=3.141592653589793D0
      N=2**M
      DO 30 L=1,M
        LE=2**L
        LEI=LE/2
        U=(1.D0,0.D0)
        W=DCMPLX(DCOS(PI/LEI),-DSIN(PI/LEI))
        DO 20 J=1,LEI
          DO 10 I=J,N,LE
            IP=I+LEI
            T=A(IP)*U
            A(IP)=A(I)-T
            A(I)=A(I)+T
10        CONTINUE
        U=U*W

```

```

20    CONTINUE
30    CONTINUE
    RETURN
    END

C
    SUBROUTINE CONV (M,F,R,H)
    DOUBLE PRECISION X
    COMPLEX*16 H(4096),F(4096),R(4096)
    N=2**M
    W1=FLOAT(N)
    DO 10 I=1,N
        H(I)=F(I)*R(I)
10    CONTINUE
    DO 20 I=1,N
        H(I)=H(I)/W1
20    CONTINUE
    RETURN
    END

C
    SUBROUTINE DECON (M,F,R,H)
    DOUBLE PRECISION X
    COMPLEX*16 F(4096),R(4096),H(4096)
    N=2**M
C IN FOURIER SPACE DECONVOLUTION IS SIMPLY A
C COMPLEX DIVISION.
    DO 10 I=1,N
        F(I)=H(I)/R(I)
10    CONTINUE
    X=FLOAT(N)
    DO 30 I=1,N
        F(I)=F(I)/X
30    CONTINUE
    RETURN
    END

C
    SUBROUTINE ITER (M,R,F,H)
    DIMENSION A(2048),B(2048)
    COMPLEX*16 R(4096),F(4096),H(4096),H1(4096),T
    CHARACTER*7 NAME
    PRINT*,'ENTER THE VALUE FOR THE PARAMETER WHICH'
    PRINT*,'CONTROLS THE ALLOWABLE ERROR BETWEEN THE'
    PRINT*,'OBSERVED SPECTRUM AND F*R. '
    PRINT*,'EPS=THE SORT OF THE SUM OF THE SQRS OF'
    PRINT*,'THE DIFFERENCES BETWEEN THE H(I)S AND'
    PRINT*,'THE F(I)*R(I)S. '
    PRINT*,'(A REAL NUMBER PLEASE.) '
    READ (*,'(F13.7)') EPS
    PRINT*,'ENTER THE MAXIMUM NUMBER OF ITERATIONS'
    PRINT*,'YOU WISH TO PERMIT. '
    PRINT*,'(AN INTEGER PLEASE) '
    READ (*,'(I3)') IEND

```

```

N=2**M
ND2=N/2
ND4=N/4
DO 30 I=1,IEND
    CALL REORDER (M,P)
    CALL FFT (M,P)
    CALL CONV (M,P,R,H1)
    CALL REORDER (M,P)
    CALL FFT (M,P)
    CALL REORDER (M,H1)
    CALL FFT (M,H1)
    RSQ=0.0
    DO 2 IA=1,N
        A(IA)=REAL(H(IA))
        B(IA)=REAL(H1(IA))
2    CONTINUE
    V=0.0
    W=0.0
    DO 4 IAA=1,N
        V=V+A(IAA)
        W=W+B(IAA)
4    CONTINUE
    DO 6 IAB=1,N
        A(IAB)=A(IAB)/V
        B(IAB)=B(IAB)/W
6    CONTINUE
    DO 10 IAC=1,ND4
        RSQ=RSQ+(A(IAC)-B(IAC))**2
10   CONTINUE
    RSQ=RSQ**0.5
    WRITE (*,11) RSQ
11  FORMAT (5X,'RSQ= ',E13.6)
    IF (RSQ .LT. EPS) GO TO 33
    F(1)=F(1)*(A(1)+2*A(2)+2*A(3))/(B(1)+2*B(2)+2*B(3))
    F(2)=F(2)*(A(1)+2*A(2)+A(3)+A(4))/(B(1)+2*B(2)+B(3)+B(4))
    DO 20 IB=3,ND4
        J=IB-2
        K=IB+2
        TH=0.0
        TH1=0.0
        DO 15 II=J,K
            TH=TH+A(II)
            TH1=TH1+B(II)
15    CONTINUE
        IF (TH1 .EQ. 0.0) GO TO 20
        F(IB)=F(IB)*TH/TH1
20    CONTINUE
    DO 25 IC=2,ND2
        J=ND2+IC
        K=ND2+2-IC
        F(J)=F(K)

```

```

25 CONTINUE
30 CONTINUE
33 CONTINUE
    I=I-1
    WRITE (*,35) I
35 FORMAT (5X,'THE NO. OF ITERATIONS IS ',I3)
    RETURN
    END

```

C

```

SUBROUTINE PARAMS (N,A)
DOUBLE PRECISION A(2048),X(12),M(10),V,W
CHARACTER*7 NAME
K=1024
DO 20 I=1,12
    X(I)=0.D0
    DO 10 J=1,5
        K=K+1
        X(I)=X(I)+A(K)
10    CONTINUE
20 CONTINUE
    V=0.D0
    DO 30 I=1025,1084
        V=V+A(I)
30 CONTINUE
    DO 40 I=1,12
        X(I)=X(I)/V
40 CONTINUE
    DO 60 I=2,10,2
        M(I)=0.D0
        DO 50 J=1026,1084
            V=FLOAT(J-1025)
            W=FLOAT(I)
            V=V**W
            M(I)=M(I)+A(J)*V
50    CONTINUE
        M(I)=M(I)/59.D0
60 CONTINUE
    M(2)=DSQRT(M(2))
    V=M(2)
    DO 65 I=4,10,2
        M(I)=M(I)/(V**I)
65 CONTINUE
    PRINT*,'ENTER THE FILENAME FOR THIS SET OF'
    PRINT*,'PARAMETERS. '
    READ (*,'(A7)') NAME
    OPEN (90,FILE=NAME,PAD='YES')
    WRITE (90,70)
70 FORMAT (5X,'EVEN CENTRAL MOMENTS')
    WRITE (90,80) (I,M(I), I=2,8,2 )
80 FORMAT (10X,'M(',I1,') =',D17.10)
    WRITE (90,100) (M(10))

```

```

100 FORMAT (9X,'M(10) =',D17.10)
    WRITE (90,110)
110 FORMAT (5X,'5 CHANNEL GROUPS (CENTER FIRST)')
    WRITE (90,120) (I,X(I),I=1,9)
120 FORMAT (10X,'X(',I1,') =',D17.10)
    WRITE (90,130) (I,X(I),I=10,12)
130 FORMAT (9X,'X(',I2,') =',D17.10)
    CLOSE (90)
    RETURN
    END

```

C

```

SUBROUTINE BACK (A,IMAX,N)
DOUBLE PRECISION A(1024),C(2048),V
COMPLEX*16 B(4096)
CHARACTER*7 NAME
ND2=N/2
ND4=N/4
DO 10 I=1,N
    C(I)=0.D0
10 CONTINUE
N1=ND2-IMAX
IF (N1 .GT. ND4) N1=ND4
DO 20 I=1,N1
    J=IMAX+I-1
    C(I)=A(J)
20 CONTINUE
N2=IMAX-1
N3=N-N2
DO 30 J=1,N2
    I=N3+J
    C(I)=A(J)
30 CONTINUE
DO 40 I=1,N
    B(I)=DCMPLX(C(I),0.D0)
40 CONTINUE
M=11
CALL REORDER (M,B)
CALL FFT (M,B)
PRINT*,'WOULD YOU LIKE TO SEE THE FIRST FEW'
PRINT*,'FOURIER COEFFICIENTS? '
READ (*,'(A1)') NAME
IF (NAME .EQ. 'N') GO TO 43
PRINT*,'HOW MANY? '
READ (*,*) IFC
WRITE (*,41) (I,B(I),I=1,IFC)
41 FORMAT (I4,2D22.10)
43 CONTINUE
PRINT*,'WOULD YOU LIKE TO SEE THE FIRST FEW'
PRINT*,'VALUES OF THE POWER SPECTRUM? '
READ (*,'(A1)') NAME
IF (NAME .EQ. 'N') GO TO 46

```

```

      PRINT*, 'HOW MANY? '
      READ (*,*) IPS
      DO 44 I=1,IPS
        A(I)=B(I)*CONJG(B(I))
44    CONTINUE
      WRITE (*,45) (I,A(I),I=1,IPS)
45    FORMAT (I4,D22.10)
46    CONTINUE
      PRINT*, 'DO YOU WISH TO DELETE ALL OF THE SINE'
      PRINT*, 'COEFFICIENTS? '
      READ (*, '(A1)') NAME
      IF (NAME .EQ. 'N') GO TO 51
      DO 50 I=1,ND2
        B(I)=(B(I)+CONJG(B(I)))/2.D0
50    CONTINUE
51    PRINT*, 'DO YOU WISH TO DELETE SOME OF THE COSINE'
      PRINT*, 'COEFFICIENTS? '
      READ (*, '(A1)') NAME
      IF (NAME .EQ. 'N') GO TO 53
      PRINT*, 'HOW MANY? '
      READ (*,*) IDC
      DO 52 I=1,IDC
        B(I)=(B(I)-CONJG(B(I)))/2.D0
52    CONTINUE
      DO 152 I=2,IDC
        J=2050-I
        B(J)=(B(J)-CONJG(B(J)))/2.D0
152   CONTINUE
53    PRINT*, 'INSTEAD OF DELETING SOME OF THE COSINE'
      PRINT*, 'COEFS. YOU MAY PREFER TO JUST TRIM THEM.'
      PRINT*, 'THIS IS DONE BY SETTING THE FIRST N TERMS'
      PRINT*, 'EQUAL TO THE N+1 TERM. YOU MAY INVOKE'
      PRINT*, 'THIS OPTION EVEN IF YOU HAVE PREVIOUSLY'
      PRINT*, 'DELETED THE FIRST N COSINE COEFFICIENTS.'
      PRINT*, 'DO YOU WISH TO DO SO? '
      READ (*, '(A1)') NAME
      IF (NAME .EQ. 'N') GO TO 200
      PRINT*, 'HOW MANY? '
      READ (*,*) IT
      DO 190 I=1,IT
        J=IT+1
        B(I)=DCMPLX(REAL(B(J)),0.D0)
190   CONTINUE
200   CONTINUE
      PRINT*, 'DO YOU WISH TO DELETE SOME OF THE SINE'
      PRINT*, 'COEFFICIENTS? '
      READ (*, '(A1)') NAME
      IF (NAME .EQ. 'N') GO TO 55
      PRINT*, 'HOW MANY? '
      READ (*,*) IDS
      DO 54 I=1,IDS

```

```

      B(I)=(B(I)+CONJG(B(I)))/2.D0
54  CONTINUE
      DO 154 I=2,IDS
          J=2050-I
          B(J)=(B(J)+CONJG(B(J)))/2.D0
154  CONTINUE
55  CONTINUE
      PRINT*,'DO YOU WISH TO SAVE THE FOURIER COEFS. OF'
      PRINT*,'H(X) PRIOR TO THE TAPER IN THE WINGS? '
      READ (*,'(A1)') NAME
      IF (NAME .EQ. 'N') GO TO 57
      PRINT*,'ENTER THE FILENAME. '
      PRINT*,' '
      READ (*,'(A7)') NAME
      OPEN (90,FILE=NAME,PAD='YES')
      WRITE (90,56) (I,B(I),I=1,2048)
56  FORMAT (2(I4,2D22.10))
      CLOSE (90)
57  CALL REORDER (M,B)
      CALL FFT (M,B)
      DO 60 I=1,ND2
          C(I)=REAL(B(I))
60  CONTINUE
      V=0.D0
      DO 70 I=359,484
          V=V+C(I)
70  CONTINUE
      V=V/126.
      PRINT*,'DO YOU WANT A D.C. CORRECTION USING A'
      PRINT*,'LEAST SQUARE FITTING IN THE TAILS? '
      READ (*,'(A1)') NAME
      IF (NAME .EQ. 'N') V=0.D0
      DO 80 I=1,ND2
          C(I)=C(I)-V
          IF (C(I) .LT. 0.D0) C(I)=0.D0
80  CONTINUE
      DO 90 I=1,ND4
          J=(3*ND4)+I
          A(I)=C(J)
90  CONTINUE
      N4=ND4+1
      DO 100 I=N4,ND2
          J=I-ND4
          A(I)=C(J)
100 CONTINUE
      IMAX=513
      RETURN
      END

```

C

```

SUBROUTINE NOBACK (N,B,IMAX)
DOUBLE PRECISION B(1024),A(2048),V

```

```

      COMPLEX*16 C(4096)
      CHARACTER*7 NAME
      M=11
      ND2=N/2
      ND4=N/4
      DO 10 I=1,N
        A(I)=0.D0
10    CONTINUE
      N1=ND2-IMAX
      IF (N1 .GT. ND4) N1=ND4
      DO 20 I=1,N1
        J=IMAX+I-1
        A(I)=B(J)
20    CONTINUE
      N2=IMAX-1
      N3=N-N2
      DO 30 J=1,N2
        I=N3+J
        A(I)=B(J)
30    CONTINUE
      V=0.D0
      DO 33 I=1,N
        V=V+A(I)
33    CONTINUE
      DO 36 I=1,N
        A(I)=A(I)/V
36    CONTINUE
      OPEN (90,FILE='RAWDATA',PAD='YES')
      WRITE (90,70) (I,A(I),I=1,N)
      CLOSE (90)
      DO 40 I=1,N
        C(I)=DCMPLX(A(I),0.D0)
40    CONTINUE
      CALL REORDER (M,C)
      CALL FFT (M,C)
      DO 50 I=1,N
        A(I)=C(I)*CONJG(C(I))
50    CONTINUE
      PRINT*,'ENTER THE FILENAME FOR E(X). '
      PRINT*,' '
      READ (*,'(A7)') NAME
      OPEN (90,FILE=NAME,PAD='YES')
      WRITE (90,60) (I,C(I),I=1,2048)
60    FORMAT (2(I4,2D22.10))
      CLOSE (90)
      PRINT*,'ENTER THE FLENAME FOR THE P.S. '
      PRINT*,' '
      READ (*,'(A7)') NAME
      OPEN (90,FILE=NAME,PAD='YES')
      WRITE (90,70) (I,A(I),I=1,1024)
70    FORMAT (5(I4,D22.10))

```


CLOSE (90)

RETURN

END

END

APPENDIX G

In this Appendix the theoretical relationship between the vacancy concentration, C_v , and the concentration of dislocation cores, C_d , is demonstrated. (from Cotterill et al. 1972). The starting equation is

$$C_v = A \exp(-E_{vf}/KT) \quad (G.1)$$

where C_v is the vacancy concentration at thermal equilibrium

E_{vf} is the vacancy formation energy

and KT has its usual meaning

Now the concentration of vacancies after the quench, C'_v , is related to C_v by

$$C'_v = nC_v \quad (G.2)$$

where n is the quench efficiency which is assumed to be nearly unity

After the low temperature anneal the concentration of dislocation loops, C_L , is given by

$$C_L = \nu C'_v \quad (G.3)$$

where ν is the inverse of the number of vacancies required to form an average loop

The dislocation concentration, C_d , in terms of an atomic fraction is then

$$C_d = C_L \pi D / d_0 \quad (G.4)$$

where D is the average loop diameter

and d_0 is the nearest neighbor distance.

It can be shown that

$$v = 2\sqrt{3} d_o^2 / \pi D^2 \quad (G.5)$$

Combining Equations (G.3), (G.4), and (G.5) yields

$$C_d = 2\sqrt{3} d_o C_v' / D \quad (G.6)$$

APPENDIX H

In this Appendix the derivation of the defect specific lineshape parameter "R" is recreated from the work of Mantl and Trifthauser (1978). The following quantities require definition:

- S, W - are the values of the "S" and "W" parameters for the sample being analyzed.
- S_t, W_t - are the values of the "S" and "W" parameters for a sample in which all of the positrons are annihilating from the trapped state.
- S_B, W_B - are the values of the "S" and "W" parameters for a sample in which all of the positrons are annihilated from the bulk (defect free).
- P_t - the probability of a positron annihilation from the trapped state.
- P_B - the probability of a positron annihilating from the bulk.
- μ - the trapping constant.
- C - the trap concentration.
- λ_B - the annihilation rate from the bulk state.

Now, it is known that

$$S = S_B P_B + S_t P_t \quad (H.1)$$

and

$$P_B + P_t = 1 \quad (H.2)$$

Also

$$P_t = \mu C / (\lambda_B + \mu C) \quad (H.3)$$

Substituting Eq. (H.3) into Eq. (H.1) yields:

$$S = S_B \left(1 - \frac{\mu C}{\lambda_f + \mu C}\right) + S_t \left(\frac{\mu C}{\lambda_f + \mu C}\right) \quad (H.4)$$

Similarly

$$W = W_b \left(1 - \frac{\mu C}{\lambda_f + \mu C}\right) + W_t \left(\frac{\mu C}{\lambda_f + \mu C}\right) \quad (H.5)$$

Rearranging Eq. (H.4) and Eq. (H.5) yields:

$$S - S_B = (S_t - S_B) \mu C / (\lambda_f + \mu C) \quad (H.6)$$

$$W - W_B = (W_t - W_B) \mu C / (\lambda_f + \mu C) \quad (H.7)$$

Taking the ratio of Eq. (H.6) to Eq. (H.7) yields:

$$R = \left| \frac{S - S_B}{W - W_B} \right| = \left| \frac{S_t - S_B}{W_t - W_B} \right| \quad (H.8)$$

Clearly the ratio on the far right has a constant value for a given defect in a given material.

REFERENCES

- Anderson, C. D., "Energies of Cosmic Ray Particles," *Physics Review*, 41, 405, 1932.
- Aulick, C. M., and Gallie, T. M., A Generalized Approach to Regularization for Ill-Conditioned Linear Systems, Technical Report, Dept. of Computer Science, Duke University, 1981.
- Bendat, J. S., and Piersol, A. G., *Random Data: Analyses and Measurement Procedures*, John Wiley and Sons, Inc., 1971.
- Brandt, W. and Arista, N., "Thermalization and Diffusion of Positrons in Solids," *Physical Review B*, 26, 8, 4229, 1982.
- Byrne, J. G., "The Utility of Positrons for Studies of Metals and Alloys," *Scripta Metallurgica*, 14, 3, 1980.
- Campbell, J. L., "Annihilation Gamma-Ray Lineshape Parameters," *Applied Physics*, 13, 365, 1977.
- Chaglar, I., "An Accurate Calculation of the 511 keV Line Background in Positron Annihilation Doppler Broadening Studies," *Nuclear Instruments and Methods*, 187, 581, 1981.
- Coleman, C. F., "Positron Annihilation - A Potential New NDT Technique," *NDT International*, 10, 227, 1977.
- Cooley, J. W., Lewis, P. A., and Welch, P. D., in *One-Dimensional Digital Signal Processing*, by Chi-Tsong Chen (Marcel Dekker, New York), 1979.
- Cotterill, R. M. J. et al., *Lattice Defects in Quenched Metals*, (New York: Academic Press) 1965.
- Cotterill, R. M. J. et al., "Positron Lifetimes and Trapping Probabilities Observed Separately for Vacancies and Dislocations in Aluminum," *Journal of Physics F: Metal Physics*, 2, 459, 1972.
- Dannefaer, S. and Kerr, D. P., "Deconvolution of Doppler Broadened Spectra of Positron Annihilation Photons," *Nuclear Instruments and Methods*, 131, 119, 1975.
- Debenedetti, S. et al., "On the Angular Distribution of Two-Photon Annihilation Radiation," *Physics Review*, 77, 205, 1950.

- Dekhtyar, T. Ya. et al., "Electron-Positron Annihilation in Plastically Deformed Metals," Soviet Physics Doklady, 9, 492, 1964.
- DeMull, F. F. M. and Bregman, J. D., "On the Analysis of Cold Neutron Time-of-Flight Spectra Using Direct Fast Fourier Transformation," Nuclear Instruments and Methods, 98, 53, 1972.
- Dirac, P. A. M., Quantum Mechanics, (Oxford University Press) Chapter XII, 1935.
- Fluss, M. J., et al., "Measurement of the Vacancy Formation Enthalpy in Aluminum Using Positron Annihilation Spectroscopy," Physics Review B, 17, 3444, 1978.
- Gerald, C. F., Applied Numerical Analysis, (Addison-Wesley, Second Edition), 1978.
- Goldanskii, V. I. et al., "Another Method of Deconvoluting Positron Annihilation Spectra Obtained by the Solid-State Detector," Applied Physics, 16, 413, 1978.
- Hautovarvi, P., et al., "Trapping of Positrons by Dislocations in Aluminum," Physics Review Letters, 24, 459, 1970.
- Hirsch, P. B. et al., "Dislocation Loops in Quenched Aluminum," Phil. Mag. 3, 897, 1958.
- Hood, G. M., and Schultz, R. J., "Annihilation and Vacancy Formation in Aluminum," Journal of Physics F: Metal Physics, 10, 545, 1980.
- Hotz, H. P. et al., "Measurement of Positron Annihilation Line Shapes with a Ge(Li) Detector," Physical Review, 170, 2, 351, 1968.
- Howell, R. H. et al., Positron Annihilation (eds. P. G. Coleman, S. C. Sharma, and L. M. Diana) 860, 1982.
- Hughes, A. E. et al., Review of Progress in Quantitative Nondestructive Evaluation, Vol. 1 (eds. D. O. Thompson and D. E. Chimenti) 661, 1982.
- Jackman, J. L. et al., "Deconvolution of Doppler-Broadened Positron Annihilation Energy Spectra in Metals," Applied Physics, 5, 259, 1974.
- Johnson, M. L. et al., "The Trapping of Positrons by Dislocations Produced in Single Crystal Bending," Metallurgical Transactions A, 9A, 841, 1978.
- Kishimoto, Y. et al., Positron Annihilation (eds. P. G. Coleman, S. C. Sharma, and L. M. Diana) 843, 1982.
- Kubica, P. and Stewart, A. T., "Thermalization of Positrons and Positronium," Physics Review Letters 34, 852, 1975.
- Lam, R. B. et al., "Practical Computation with Fourier Transforms for Data Analysis," Analytical Chemistry, 53, 7, 889, 1981.

- Mackenzie, I. K. et al., "Some Temperature Effects on Positron Annihilation in Metals," *Canadian Journal of Physics*, 42, 1837, 1964.
- Mackenzie, I. K. et al., "Temperature Dependence of Positron Mean Lives in Metals," *Physical Review Letters*, 19, 17, 946, 1967.
- Mackenzie, I. K. et al., "The Interaction Between Positrons and Dislocations in Copper and in an Aluminum Alloy," *Physics Letters*, 33A, 5, 279, 1970.
- Mackenzie, I. K. et al., "Positron Systematics in Annealed Metals," *Applied Physics*, 9, 259, 1976.
- Mantl, S. and Trifthauser, W., "Defect Annealing Studies on Metals by Positron Annihilation and Electrical Resistivity Measurements," *Physical Review B*, 17, 1645, 1978.
- Martin, J. W., and Paetsch, R., "Interaction of Positrons and Dislocations," *Journal of Physics F: Metal Physics*, 2, 997, 1972.
- McNelles, L. A. and Campbell, J. L., "Analytic Approximations to Peak Shapes Produced by Ge(Li) and Si(Li) Spectrometers," *Nuclear Instruments and Methods*, 127, 73, 1975.
- Moore, K. D., "Positron Annihilation Methods for Nondestructive Study of the Effect of Thermal and Mechanical Treatment and Hydrogen Environments on the Defect Structure of Commercial Iron Alloys," Ph.D. Dissertation, Duke University, 1983.
- Penrose, R., "On Best Approximate Solutions of Linear Matrix Equations," *Proceedings of the Cambridge Philosophical Society*, 52, 17, 1956.
- Rautian, S. G., "New Apparatus and Methods of Measurement," *Soviet Physics Uspekhi*, 1, 245, 1958.
- Reddy, K. R. and Carrigan, R. A., "On the Doppler Broadening of Two-Photon Positron Annihilation Radiation," *Il Nuovo Cimento*, Vol. LXVI B, 105, 1970.
- Rindler, W., *Special Relativity*, (Oliver and Boyd) 1960.
- Schaffer, J. P. et al., "Deconvolution of Doppler-Broadened Positron Annihilation Measurements Using Fast Fourier Transforms and Power Spectral Analysis," *Journal of Nuclear Instruments and Methods in Physics Research*, B5, 75, 1984.
- Schultz, P. J. et al., "Analysis Procedures for Annihilation Energy Spectra with Enhanced Sensitivity to Positron Localization," *Canadian Journal of Physics*, 59, 325, 1981.
- Siegel, R. W., *Annual Review of Materials Science*, (eds. R. A. Huggins, R. H. Bube, and D. A. Vermilyea), 10, 393, 1980.
- Smedskjaer, L. C. and Fluss, M. J., in *Methods of Experimental Physics*, Vol. 21 (Academic Press), 1983.

- Stevens, J. R., "Probe and Label Techniques: Positron Annihilation," *Methods of Experimental Physics*, 16A, 371, 1980.
- Szotek, Z. and Chmielewski, S., "Deconvolution of Positron Annihilation Curves with Regard to the Instrumental Resolution Function," *Acta Physica Polonica*, A60, 6, 829, 1981.
- Turchin, V. F. et al., "The Use of Mathematical-Statistical Methods in the Solution of Incorrectly Posed Problems," *Soviet Physics Uspekhi*, 13, 6, 681, 1971.
- Verkerk, P., "Resolution Correction: A Simple and Efficient Algorithm with Error Analysis," *Computer Physics Communications*, 25, 325, 1982.
- West, R. W., *Positron Studies of Condensed Matter* (Taylor and Francis, London) 1974.
- Wilkes, P. and Harrison, E. A., "Improved Dilatometric Technique for the Study of Vacancies," *Journal of Physics E: Scientific Instruments*, 1972.

BIOGRAPHY

James Peter Schaffer was born on November 13, 1959, in Wilmington, Delaware. He received his Bachelor of Science in Mechanical Engineering and Materials Science (Magna Cum Laude) in 1981 from Duke University in Durham, North Carolina. He received his Master of Science degree in Mechanical Engineering and Materials Science in the following year.

Mr. Schaffer published several papers during his years as a graduate student. These include:

- 1) "Photoconductivity of Amorphous Hydrogenated Silicon" with J. H. Lind, P. L. Jones, and F. H. Cocks, Physica Status Solidi (a) 71, K111, 1982.
- 2) "Hydrogenated Amorphous Boron: Transient and Steady State Photoconductivity" with H. Park, J. H. Lind and P. L. Jones, Physica Status Solidi (a) 81, K51, 1984.
- 3) "The Deconvolution of Doppler Broadened Positron Annihilation Measurements using Fast Fourier Transforms and Power Spectral Analysis" with E. J. Shaughnessy and P. L. Jones, Nuclear Instruments and Methods in Physics Research B5, 75, 1984.
- 4) "A Comparison of the Doppler Broadened Positron Annihilation Spectra of Neutron Irradiated Al_2O_3 and $MgAl_2O_4$ " with P. L. Jones, F. H. Cocks, F. W. Clinard, Jr., and G. F. Hurley, Journal of Nuclear Materials 127, 221, 1985.

In addition, Mr. Schaffer presented a paper entitled "On the Application of Fast Fourier Transforms and Power Spectrum Analysis to Incorrectly Posed Integral Equations" at the Integral Methods in Science and Engineering Conference in Arlington, Texas, March 18-21, 1985.

In 1981, Mr. Schaffer received a research and teaching assistantship award from Duke University for graduate study in the Department of Mechanical Engineering and Materials Science. In the following year he was awarded a three year Fellowship from the Office of Naval Research. During his graduate studies, Mr. Schaffer was inducted into Sigma Xi, the National Scientific Research Society.

**This Page is Inserted by IFW Indexing and Scanning
Operations and is not part of the Official Record**

BEST AVAILABLE IMAGES

Defective images within this document are accurate representations of the original documents submitted by the applicant.

Defects in the images include but are not limited to the items checked:

- ☐ **BLACK BORDERS**
- ☐ **IMAGE CUT OFF AT TOP, BOTTOM OR SIDES**
- ☐ **FADED TEXT OR DRAWING**
- ☐ **BLURRED OR ILLEGIBLE TEXT OR DRAWING**
- ☐ **SKEWED/SLANTED IMAGES**
- ☐ **COLOR OR BLACK AND WHITE PHOTOGRAPHS**
- ☐ **GRAY SCALE DOCUMENTS**
- ☐ **~~LINES~~ OR MARKS ON ORIGINAL DOCUMENT**
- ☐ **REFERENCE(S) OR EXHIBIT(S) SUBMITTED ARE POOR QUALITY**
- ☐ **OTHER: _____**

IMAGES ARE BEST AVAILABLE COPY.

As rescanning these documents will not correct the image problems checked, please do not report these problems to the IFW Image Problem Mailbox.

This Page Blank (uspto)